Development and Testing of a Beam-Powered Thermal Propulsion Laboratory Model

AE5810: Thesis Space

Diogo A. M. D. Gomes

Delft University of Technology

TU Delft

Development and Testing of a Beam-Powered Thermal Propulsion Laboratory Model

by

Diogo A. M. D. Gomes

Student Name	Student Number
Diogo A. M. D. Gomes	5447585

Supervisor: Ir. B.T.C. Zandbergen
Project Duration: May 2023 - June 2024
Faculty: Faculty of Aerospace Engineering, Delft

TU Delft

ABSTRACT

Beam-powered thermal propulsion, utilizing an external energy beam to heat a propellant, is proposed as a promising alternative to traditional chemical and electrical propulsion systems. This research aims to contribute to this technology's numerical and experimental development, offering a comprehensive analysis of the receiver-absorber cavity (RAC) performance and its optimization.

The work begins with a detailed background study of the principles of beam-powered propulsion. This sets the stage for the subsequent chapters, which investigate the numerical modelling and experimental testing of the thruster.

The numerical part of this thesis focuses on developing accurate prediction tools for the total absorbed beam power by the RAC. This information is added to a previously developed RAC performance prediction tool and the development of a new tool considering spatial information is started. The optimization process regarding efficiency is presented with an example case study with optimal values above 80% with a margin to improve.

The experimental component involves the design, manufacturing, and testing of a prototype beam-powered thermal thruster. Leak testing, test bench calibration and a cold flow test are conducted. Detailed test procedures and setups for these are presented, alongside their results. The experimental findings are compared with the numerical predictions to assess the accuracy and reliability of the models.

The thesis concludes with evaluating the research questions, and discussing the successes and challenges encountered. Recommendations for future work are provided, aiming to guide further advancements in beam-powered thermal propulsion technology. The combination of numerical and experimental insights gained through this research contributes to the feasibility and optimization of beam-powered thermal propulsion systems.

ACKNOWLEDGEMENTS

Tenho em mim todos os sonhos do mundo

Fernando Pessoa

This thesis project marks the end of a huge chapter in my life: the Aerospace Engineering adventure that started back in 2018. These past six years have been filled with incredible and unforgettable moments and I am extremely happy with my performance and work developed. I took on the challenge of working on a thesis with an experimental component to consciously address and fill a gap in my expertise. Through this endeavour, I successfully filled that gap, making me a more well-rounded and proficient engineer.

First, I would like to thank my supervisor Barry Zandbergen for his guidance and support throughout the whole thesis duration. He provided me with the freedom to explore my interests while ensuring that I remained focused on the overall goal. The constant and constructive feedback substantiated by his extensive experience played a significant role in my learning journey.

This project would have never become the way it is due to the help of several people. I would like to acknowledge the help provided by the IWS, EWS, DEMO staff and Mr. Jurriaan van Slingerland who helped me in the manufacturing process of the thesis. Also, my friend José Reis with his extremely hands-on capacity and proactive attitude spent countless hours helping me with designing and manufacturing.

I would like to thank my friends for their encouragement and for providing much-needed balance. To my Portugal friends, thank you for always being there for me even if at a distance. To the friends that I have met throughout my stay in the Netherlands, you filled these three years with unique moments and unforgettable coffee breaks.

On a personal note, I am forever indebted to my family for their unwavering support and understanding throughout this journey. Their patience and belief in my abilities have been a source of constant motivation. Without their sacrifices, I would not be here at this moment graduating from one of the best universities in the world.

Now a new and for sure exciting chapter begins.

Diogo A. M. D. Gomes
Delft, July 2024

CONTENTS

Abstract i

Acknowledgements ii

List of Figures vii

List of Tables x

1 Introduction 1

2 Background Information 4
2.1 Beam-powered thruster system . . . 4
2.2 Ideal Rocket Theory . . . 6
2.3 Work at TU Delft . . . 8
2.4 Other literature findings . . . 9
2.5 Engineering process . . . 10
2.6 Research Questions . . . 10

3 Beam Power Absorption Theory 12
3.1 Beam Reflection . . . 12
3.2 Beam Power Distribution . . . 13
3.3 View Factors . . . 14
3.3.1 Gebhart Factors . . . 15
3.4 Geometrical Cavity Shape . . . 15
3.5 Ray Tracing . . . 16
3.6 Theoretical Predictive Algorithms . . . 18
3.6.1 View Angle Method - Diffuse Reflection . . . 18
3.7 Finite Element Method . . . 19
3.7.1 Sensitivity analysis . . . 21
3.8 Verification . . . 22
3.8.1 Specular Reflection . . . 22
3.8.2 Diffuse Reflection . . . 23
3.9 Results and Analysis . . . 24
3.9.1 Total absorption . . . 24
3.9.2 Variable Effect . . . 24
3.9.3 Surface reflectivity . . . 26
3.9.4 Geometry . . . 27
3.9.5 Comparison to previous methods . . . 29
3.10 Model Regression . . . 30
3.11 Conclusions and future work . . . 31

4 Receiver-Absorber Cavity Performance Prediction Tools **33**
4.1 Heat Balance . . . 33
4.2 Thermal radiation . . . 34
4.3 Conduction . . . 35
4.4 Convection . . . 36
4.5 Zero-order Model . . . 37
4.5.1 Assumptions . . . 37
4.5.2 Overview . . . 38
4.5.3 Verification . . . 40
4.6 FEM Model . . . 41
4.6.1 Assumptions . . . 41
4.6.2 Overview . . . 42
4.6.3 Verification . . . 43
4.7 Conclusion and recommendations . . . 45

5 RAC Design Optimization **47**
5.1 RAC Efficiency . . . 47
5.2 Case Study - Inputs and constraints . . . 49
5.3 Absorption Efficiency Optimization . . . 50
5.3.1 Optimization method . . . 50
5.3.2 Surface coating effect . . . 53
5.3.3 Conduction Effect . . . 54
5.3.4 Convection Effect . . . 55
5.4 Heat exchanger efficiency optimization . . . 55
5.4.1 Optimization method . . . 56
5.4.2 Number of ducts effect . . . 57
5.5 Overall Efficiency Optimization . . . 58
5.6 Baselines for Laboratory Model . . . 61
5.7 Conclusions and Future Work . . . 62

6 Experimental Design and Hardware **63**
6.1 Locations . . . 63
6.2 Thruster General Requirements . . . 63
6.3 Thruster Design and Manufacturing . . . 64
6.3.1 RAC . . . 64
6.3.2 Connection Pieces . . . 66
6.3.3 Nozzle . . . 68
6.3.4 Thruster Support . . . 70
6.4 Thruster Assembly . . . 72
6.5 Test Set-up Hardware and Software . . . 73
6.5.1 Cleanroom Computer and PC . . . 74
6.5.2 Pressure sensors . . . 75
6.5.3 Mass flow sensors . . . 76
6.5.4 Thermowell and MAX6675 Amplifier . . . 76
6.5.5 Load cell and Signal Amplifier . . . 77
6.5.6 Nitrogen feed system . . . 78

6.5.7 Variable turn density coil . . . 79
6.5.8 Test bench . . . 79
6.6 Summary . . . 80

7 Preliminary Tests **81**
7.1 Thrust measurement calibration . . . 81
7.1.1 Load Cell . . . 81
7.1.2 Test Bench . . . 82
7.2 Leak testing . . . 86
7.2.1 Methodology and setup . . . 86
7.2.2 Exploratory testing . . . 87
7.2.3 Results and Discussion . . . 87
7.3 Conclusions and recommendations . . . 89

8 Nitrogen Testing **92**
8.1 Experimental approach . . . 92
8.2 Test Results . . . 95
8.3 Data elaboration . . . 97
8.3.1 Pressure Drop Estimation . . . 97
8.3.2 Mass flow adjustment . . . 98
8.4 Discussion . . . 99
8.4.1 Discharge coefficient . . . 99
8.4.2 Nozzle Flow Quality . . . 101
8.5 Conclusion and Recommendations . . . 102

9 Conclusion **104**

Bibliography **110**

A Ray Tracing Simulations **111**
A.1 Numerical Simulation Setup . . . 111
A.2 Simulation numerical parameters . . . 115

B 2D Specular Rectangular Algorithm **118**
B.1 Algorithm . . . 118

C View Angle Method **123**

D Beam Absorption Results **131**
D.1 Variable Effect . . . 131
D.2 Surface Reflectivity . . . 133

E Convection - Literature Study **136**
E.1 Convection . . . 136
E.1.1 Inner Cavity Convection . . . 137
E.1.2 Single-Phase Propellant Convection . . . 139
E.1.3 Two-Phase Propellant Convection . . . 143
E.1.4 Outer wall convection . . . 145
E.2 Pressure Gradient . . . 146

F Locations **152**

G Data Sheets **155**
G.1 Pressure Sensor . . . 155
G.2 Futek LSB200 . . . 159

H Test Procedures **162**
H.1 Leak Test Procedure . . . 162
H.1.1 Background and Instrumentation Overview . . . 162
H.1.2 Preparation . . . 163
H.1.3 Experiment Execution . . . 163
H.1.4 Shutdown . . . 164
H.2 Test Bench Calibration Test Procedure . . . 164
H.2.1 Background and Instrumentation Overview . . . 164
H.2.2 Preparation . . . 165
H.2.3 Experiment Execution . . . 165
H.2.4 Shutdown . . . 165
H.3 Cold Gas Flow Test Procedure . . . 165
H.3.1 Background and Instrumentation Overview . . . 165
H.3.2 Preparation . . . 166
H.3.3 Experiment Execution . . . 166
H.3.4 Shutdown . . . 167

I Nitrogen Test Plots **169**

J Discharge Coefficient for Orifice Plates **174**

List of Figures

1.1 Propulsion system thrust/weight ratio and specific impulse values [4]. . . 1

2.1 Conical RAC (cross-sectional view) - indirect heating and direct propulsion [10]. . . . 5
2.2 Spacecraft architecture overview - Inflatable Parabolic Reflector [9]. . . . 6
2.3 The three geometry shapes of cavity receiver studied by Daabo et. al [17]. . 9

3.1 Specular and diffuse reflection. The rays represent the luminous intensity. [29] . . . 13
3.2 Laser beam Gaussian distribution and beam diameter. . . . 14
3.3 Cavity Geometry and its variables . . . 16
3.4 COMSOL Ray Tracing Interface - 3D Cylinder simulation . . . 17
3.5 Probability of diffuse reflection inside a rectangular cavity . . . 18
3.6 Effect of FEM in capturing the power distribution . . . 20
3.7 Relative error of 1 node per surface . . . 21
3.8 Method Verification via relative error . . . 23
3.9 Total absorbed beam power percentage by geometry . . . 24
3.10 Variable effect on total absorption percentage diffuse reflection of all geometries . . . 25
3.11 Relative difference in absorption between the specular and diffuse case for all the geometries studied. . . . 26
3.12 Relative difference between cylinder and other cone ratios with diffuse reflection . . . 27
3.13 Boxplot of the effect of each input variable in the relative power absorption difference between cylinder and cone . . . 28
3.14 Relative difference between FEM and Takken's method . . . 29
3.15 Variable effect on relative difference to Takken's estimate in both geometries 30

4.1 Block diagram of the transient zero-order model process . . . 39
4.2 Block diagram of the FEM model process . . . 43
4.3 Absorbed power distribution [%/m^2] for the cylindrical case of table 4.5 in both models. . . . 45

5.1 Geometries of interest to the case study in 2D axial view (not to scale) - CR = 0, 0.5, 1. . . . 49
5.2 Overview of the absorption efficiency optimization process . . . 51
5.3 Example of optimization verification plots . . . 52
5.4 T_{eq} optimal geometry verification plots . . . 54

5.5 n_{pipes} effect on η_{hx} and optimal duct shape at $\dot{m}$ = 251 mg/s and T_b = 700 K. 57
5.6 Correlation between overall efficiency and absorbed beam power in the case study for the cylindrical geometry 60

6.1 RAC manufacturing process 67
6.2 Nozzle manufacturing 70
6.3 Thruster support manufacturing 72
6.4 Exploded view of the thruster 73
6.5 Fully Assembled Thruster 73
6.6 Schematic of the experimental hardware 75
6.7 Example of thermowell setup assembled [43] 77
6.8 Load cell and amplifier 78
6.9 Nitrogen gas feed system with components indicated [45]. 78
6.10 TB-50m test bench with load cell and VTDC 80

7.1 LSB200 relationship between output voltage and mass load 82
7.2 Test bench with the thruster connected to its instrumentation on. 83
7.3 Example of successful calibration run without thruster on the test bench . 84
7.4 Example of a successful calibration run with the thruster on the test bench 85
7.5 Leaks detected during exploratory testing - red areas 87
7.6 Leak testing pressure and mass flow results - p_a = 1.066 bar 88

8.1 Test bench with the thruster connected to its instrumentation on. 93
8.2 RAC manufacturing process 96
8.3 Schematic of critical nozzle geometry studied by Johnson [48] 100
8.4 [47] 102

B.1 Specular reflection of a ray with an arbitrary angle inside a rectangular cavity 118

C.1 Probability of diffuse reflection inside a rectangular cavity 123
C.2 Probability of diffuse reflection inside a conical cavity 129

D.1 Variable effect on total absorption percentage specular reflection of all geometries 132
D.2 Variable effect on relative power absorption difference between diffuse and specular surfaces in a cylindrical cavity 133
D.3 Variable effect on relative power absorption difference between diffuse and specular surfaces in a concylindrical cavity 134
D.4 Variable effect on relative power absorption difference between diffuse and specular surfaces in a conical cavity 135

E.1 Variations of Q_c for a cylindrical cavity in different conditions [9]. 138
E.2 Convection heat loss for different geometries [10]. 139
E.3 The development of a two-phase flow in a vertical tube with a uniform wall heat flux (not to scale) [2] 144

E.4 The boiling curve of water at 1 atm and various heat transfer regimes [21] 144

H.1 Nitrogen Feed System and its components [3]. 163

I.1 NT-1 Results 170
I.2 NT-2 Results 171
I.3 NT-3 Results 172
I.4 NT-4 Results 173

J.1 Straight nozzle experimental data from Kayser and Shambaugh [1]. 175
J.2 Effect of pressure ratio and length-diameter ratio on mass flow number and discharge coefficient [2]. 176
J.3 Comparison of predicted and experimental values of discharge coefficients for L/D ratios equal to 1.0 and 2.0 [2] 176

List of Tables

3.1 Parameters for 2D and 3D ray tracing simulations . . . 17
3.2 Best regression model for each geometry depending on surface reflection 31
3.3 Comparison of the average simulation time for one simulation (t_s) for different simulation methods. - 10k rays and 100 nodes per surface . . . 32

4.1 Zero-Order model assumptions/constraints and rationale . . . 38
4.2 Zero-order model inputs . . . 38
4.3 Geometric and Operational Parameters for the model's comparison . . . 41
4.4 FEM model assumptions/constraints and rationale . . . 42
4.5 Difference between zero-order and FEM model - Case Study results . . . 45

5.1 Input Parameters for the Optimization Case Study . . . 50
5.2 Case study optimization results for both models . . . 51
5.3 Optimal geometrical values for each example coating (CR = 0) . . . 53
5.4 Optimal geometrical values for each example coating and no conduction . 55
5.5 Case study's heat exchanger efficiency at different bulk temperatures with $\dot{m} = 251$ mg/s . . . 56
5.6 Case Study heat exchanger efficiency - Nu and P^2/L variation at $\dot{m} = 251$ mg/s and $T_b = 700$ K. . . . 57
5.7 Case Study heat exchanger efficiency - Nu and P^2/L variation at $n_{pipes} = 2$, $\dot{m} = 251$ mg/s and $T_b = 700$ K. . . . 58
5.8 Overall efficiency for different lengths and cone ratios at $\dot{m} = 251$ mg/s and $D = 4$ cm . . . 59
5.9 Case Study RAC parameters with the optimal solution . . . 60
5.10 Manufactured RAC parameters . . . 61
5.11 Case Study - Laboratory Model expected performance at $\dot{m} = 251$ mg/s . . . 62

6.1 Nitrogen testing theoretical values - ideal conditions . . . 64
6.2 RAC design requirements . . . 65
6.3 Connection components requirements . . . 67
6.4 Nozzle design requirements . . . 69
6.5 Thruster support requirements . . . 71
6.6 Experimental instrumentation overview . . . 74

7.1 Averaged calibration results before the cold flow test . . . 85
7.2 Averaged calibration results after the cold flow test . . . 86
7.3 Mass flow sensor method results . . . 88

8.1 Nitrogen testing measured parameters . . . 93

8.2 Nitrogen testing experiment sets and expected values, p_a = 1.066 bar and T_c = 15°C . . . 94
8.3 Acceptance criteria for nitrogen testing . . . 94
8.4 Nitrogen testing averaged results and standard deviation, p_a = 1.066 bar for all . . . 96
8.5 Pressure drop estimate for each test . . . 98
8.6 Experimental mass flow adjustment . . . 98
8.7 Theoretical and experimental mass flows . . . 99
8.8 Nozzle flow quality $\xi_{I_{sp}}$ for the different tests . . . 101

A.1 Parameter Table . . . 112
A.2 Polygon coordinates table . . . 113
A.3 Ray termination bounding box criteria . . . 114
A.4 Parametric Sweep Settings . . . 114
A.5 Simulation results and time vs. Number of Rays of rectangular cavity with specular reflection . . . 116

NOMENCLATURE

Abbreviations

FEM	Finite Element Method
RAC	Receiver-absorber cavity
$RMSE$	Root mean square error
TUD	Technische Universiteit Delft

Greek Symbols

α	Absorptivity
η	Efficiency
Γ	Vandenkerckhove function
γ	Specific heat ratio
ρ	Density
σ	Stefan-Boltzmann constant
θ	Half-beam divergence angle
ε	Emissivity, error
φ	Angle
ξ	Quality factor

Latin Symbols

AR	Aperture ratio
CR	Cone ratio
LR	Length ratio
o	Beam origin
V_{ij}	View angle formula
$\dot{m}$	Mass flow
A	Area, Aperture diameter
B_{ij}	Gebhart factor
C_d	Discharge Coefficient
c_p	specific heat capacity
D	Diameter
f_{DB}	Darby-Weisbach factor
F	Thrust
F_{ij}	View factor
g_0	standard gravity
h	Height, Convective heat transfer coefficient
I_{sp}	Specific impulse
k	thermal conductivity
L	Length
L_s	Characteristic length
M	Molar mass
m	mass
Nu	Nusselt number
P	Power, Perimeter
p	Pressure
R	Specific gas constant
r	Radius
R_A	Absolute gas constant
T	Temperature
t	Time, thickness

U	Velocity
w	Width

Subscripts

a, amb	Ambient
abs	Absorbed
adj	Adjusted
$algo$	Algorithm
ap	Aperture
c	Chamber
con	Cone
$cond$	Conduction
$conv$	Convection
cr	Critical
cyl	Cylinder
dif	Diffuse reflection
e	Exit
eq	Equivalent
est	Estimate
exp	Experimental
f	Final
i	Initial, Inner
ins	Insulation
n	Nozzle
o	Outer
p	Propellant
RAC	Receiver-absorber cavity
rad	Radiation
rel	Relative
sim	Simulation
sp	Single-phase
$spec$	Specular reflection
$surf$	Surface
t	Throat
th	Theoretical
w	Wall

1

INTRODUCTION

Several spacecraft propulsion systems have been developed throughout the last decades [1]. For example, chemical propulsion has been consistently used by rockets [2] and electrical propulsion is commonly present in satellites for station-keeping purposes [3]. Other concepts, such as solar thermal propulsion and antimatter propulsion, have never flown in space or only the concept has been formulated. Each of these propulsion systems has its advantages and disadvantages.

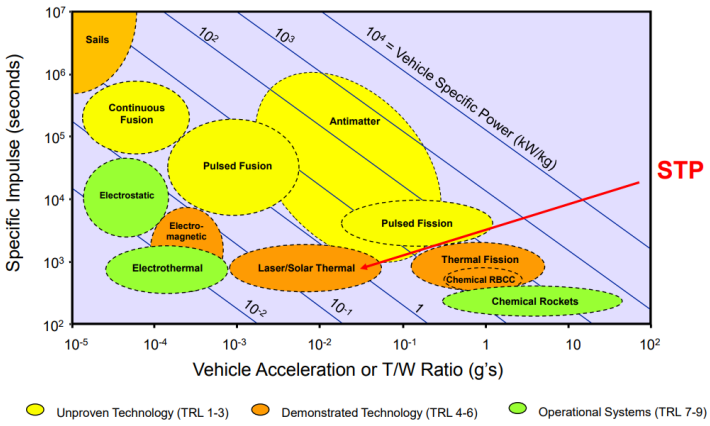

Figure 1.1: Propulsion system thrust/weight ratio and specific impulse values [4].

Fig. 1.1 shows the specific impulse I_{sp} and the thrust-to-weight ratio of several propulsion systems which are relevant quantities in propulsion [4]. The specific impulse, I_{sp}, is related to the amount of propellant mass needed for a certain thrust and dictates the amount of propellant required to be carried on board to perform a certain mission, according to the rocket equation; and thrust, F, determines the acceleration that can be reached [5]. For instance, chemical propulsion has high thrust levels and low specific

impulse which result in short burn times but high propellant mass demands, whereas electrical propulsion systems have high specific impulse but low thrust levels, leading to long burn times and, consequently, high gravity losses, despite their lower mass requirements [5].

The current limitations of existing spacecraft propulsion systems, including high propellant mass requirements and long acceleration times, as well as the rising mission costs and decreasing budgets, have resulted in payload restraints, making it challenging to explore deeper space missions [6] [7]. Consequently, there is a need for alternative propulsion systems that can address the limitations of existing spacecraft propulsion systems and enable more efficient and cost-effective deep-space exploration [7]. This could be achieved by systems that fit in between the two previously mentioned propulsion systems.

Beam-powered thermal propulsion utilizes an external energy beam to heat a propellant, accelerating the spacecraft. It is a technology whose specific impulse and thrust levels have been proposed theoretically to be between the electrical and chemical propulsion values [4]. The beam can originate from a laser or a concentrated sun ray and, thus, referred to as laser or solar thermal propulsion, respectively. Due to their similarities, developments in one can be extensively applied to the other. Using hydrogen as a propellant, a specific impulse as high as 800 seconds could be reached [8]. Recent research has suggested that a laser thermal propulsion system could be a solution to interplanetary travel [9]. Despite never having flown in space, beam-powered thermal propulsion is a promising and creative technology whose further investigation could lead to a new, reliable and efficient propulsion system alternative.

At Delft University of Technology, students have performed work in developing solar thermal propulsion technology. For example, Leenders [10] performed thrust experiments with a theatre lamp as the power source. Leverone [8] studied bi-modal solar thermal propulsion and power systems and, most recently, Takken [11] developed a prediction tool and unsuccessfully tried to perform laser thermal propulsion experiments.

Considering the previous work and the literature, the author decided to tackle beam-powered thermal propulsion and contribute to its numerical and experimental developments. Thus, this thesis contains a numerical component where advances in the prediction tools were made and an experimental part to contribute to the feasibility of these types of systems.

Thus, the thesis work starts with the background information in Chapter 2 to familiarize the reader with the topic and introduce the reasoning behind the work performed. In this chapter, the usual composition of beam-powered thruster systems is explored. In addition, a comprehensive review of existing literature and highlights of the contributions made by previous TU Delft students are presented. The chapter concludes by identifying research questions that address the gaps found in the literature and previous studies. These are tackled in the following chapters and are:

Q1 Can the beam power absorption be modelled to an accuracy of 5%?

Q2 How do the receiver-absorber cavity (RAC) and its duct geometry change affect performance?

Q3 What overall RAC efficiency values can be achieved?

Q4 How does the experimental data relate to the prediction model?

Chapter 3 introduces the numerical part of this thesis and answers research question Q1. It has the goal of developing an accurate prediction method for the total absorbed beam power by the receiver-absorber cavity (RAC). The RAC is one of the system's components whose purpose is to absorb the beam power and transfer it to the propellant. First, the theoretical background of laser absorption in a cavity is explained. Then, the prediction methods used and developed are explained and their findings are presented. In Chapter 4, the two developed receiver-absorber cavity (RAC) prediction tools are presented and verified. This chapter includes an initial description of the thermal processes involved in the RAC, a critical evaluation of the tools and offers recommendations for their further development. Next, the RAC design optimization using the tools developed is the topic of Chapter 5. Here the research questions Q2 and Q3 are tackled using the tool developments made in the previous chapter. Optimization trends are identified and explained with a case study similar to the experimental situation providing example results.

Regarding the experimental part of the thesis, Chapter 6 addresses the experimental design and manufacturing process, considering the established requirements and constraints. Moreover, the hardware used is described. In Chapter 7, the preliminary testing conducted (leak testing and thrust bench calibration) is documented. These are fundamental to interpreting the data gathered in the following thrust experiments. Research question Q4 is addressed in Chapter 8 by discussing the nitrogen cold flow testing in detail. This includes a description of the experimental procedure, a presentation of test results and their discussion. The experimental findings are compared to ideal rocket theory and Takken's developed model, with discrepancies analyzed in the context of related literature.

Lastly, Chapter 9 provides a succinct conclusion of the entire work, evaluating the success of the research concerning the initial research questions. The difficulties along the work are discussed and recommendations for future work are given, informed by the experiences and insights gained during the thesis. This final chapter aims to guide further research and development in the field of numerical and experimental beam-powered thruster systems.

2

BACKGROUND INFORMATION

Previous to the thesis, the author conducted an extensive literature study regarding the topic of beam-powered propulsion to familiarize himself with the topic and to find research gaps that could be addressed in the period of a thesis [12]. Thus, work performed by previous TU Delft students and other authors in academia was investigated and critically analysed.

In this chapter, the relevant information acquired about beam-powered propulsion is concisely presented. First, the common components of a beam-powered propulsion system and ideal rocket theory are presented. Then, the work developed at TU Delft is reported followed by the pertinent findings in the literature. Lastly, the research gaps and consequent questions are presented.

2.1. BEAM-POWERED THRUSTER SYSTEM

In a beam-powered thermal thruster, the beam energy is received and absorbed by the spacecraft and used to heat a propellant fluid to very high temperatures. A critical component in the effectiveness of this propulsion system is the RAC design since it determines the energy transfer efficiency to the propellant. This design directly influences the overall performance and efficiency of the propulsion system, making it a key area of research and development.

The beam-powered thruster system components will depend on its configuration. Three possible RAC configurations have been mentioned by previous students regarding solar thermal propulsion research: direct propulsion with direct absorption, direct propulsion with indirect absorption and indirect propulsion with indirect absorption [13] [14]. If the incoming radiation is used immediately to heat the propellant then it is direct propulsion; whereas if the energy is stored, for instance, in thermal storage, then it is considered indirect. Absorption can be direct if the radiation hits the propellant directly and indirect if it hits a medium that is in contact with the propellant. An example of direct propulsion with direct absorption is the design proposed by Duplay et al. [9] where there is a window in the thrust chamber that allows for the laser to hit the propellant. Examples of direct propulsion with indirect absorption are the cavities developed at

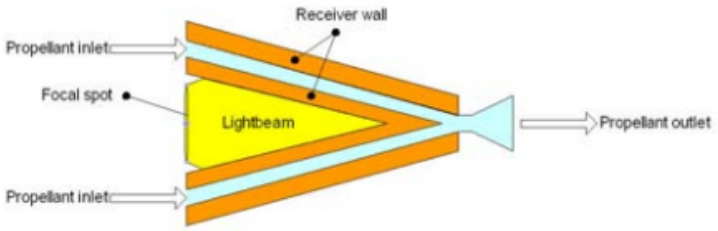

Figure 2.1: Conical RAC (cross-sectional view) - indirect heating and direct propulsion [10].

TU Delft by Leenders (Fig. 2.1) [10] and Takken [11] that are heated up with the incoming radiation and the propellant is flowing in between its walls.

Regarding, direct propulsion and absorption, its efficiency is related to the propellant's absorptivity [9]. However, hydrogen, the preferable propellant due to its low molar mass, has an inherent low absorption which presents itself as an obstacle. It is possible to seed the propellant with, for example, carbon particles that absorb the radiation and then heat the neighbouring hydrogen particles [15]. Although this can effectively fix the absorption problem, the carbon particles are also propelled and, therefore, increase the average propellant molar mass which defeats the purpose of hydrogen to some degree. Due to its added complexity in manufacturing, absorption and heat transfer processes, this design is not considered for either numerical or experimental development in this thesis.

Consequently, this thesis focuses on beam-powered thermal propulsion via indirect heating and, depending on the beam source, the beam-powered thermal propulsion system can be divided into the following distinctive components [9]:

- Laser System,
- Optical/Reflective System,
- Receiver/Absorber Cavity (RAC),
- Propellant and its tank, feed system and tubing,
- Nozzle.

Other additional elements may be present such as a thermal energy storage system, typically used in bi-modal propulsion systems [8]. This allows for thrust generation during occasional periods when beam energy cannot be received.

The laser system produces the beam. It can be onboard the spacecraft or located externally. The former requires the conversion of electrical (or solar) energy to laser energy while the latter suffers from beam spreading and needs a larger receptor. In the solar thermal propulsion case, the energy source is the sun.

The optical/reflective system collects, focuses and redirects the beam into the RAC. The RAC absorbs the incoming beam power and transfers that energy to the fluid flowing

in it - heat exchanger mechanism. The propellant system stores the propellant at the intended conditions and feeds the thruster system. Lastly, the nozzle accelerates the propellant flow and generates thrust.

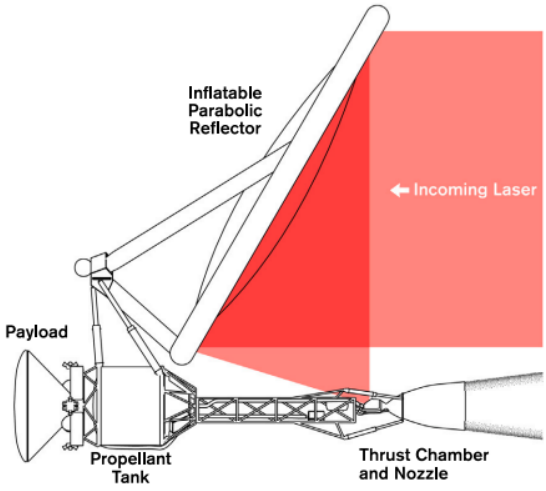

Figure 2.2: Spacecraft architecture overview - Inflatable Parabolic Reflector [9].

In Fig. 2.2, the components of a laser-powered thruster using a direct heating and propulsion configuration are illustrated [9]. The main difference is the RAC element being the thrust chamber but it still gives a good illustration overview of beam-powered thermal propulsion systems.

2.2. IDEAL ROCKET THEORY

Ideal rocket theory (IRT) calculates the performance of an ideal rocket motor and its development is established on the following assumptions [5]:

- The nozzle flow is one-dimensional, steady and isentropic.
- The propellant obeys the ideal gas law.
- The propellant has negligible velocity in the chamber.

Consequently, IRT can be used to compare the experimental to the expected values. Zandbergen's work [5] is a good and concise source to go deeper into the subject.

The produced thrust can be calculated by:

$$F = \dot{m} U_{eq}, \tag{2.1}$$

where $\dot{m}$ is the mass flow and U_{eq} is the equivalent exhaust velocity relative to the vehicle:

$$U_{eq} = U_e + \frac{p_e - p_a}{\dot{m}} A_e, \tag{2.2}$$

where U_e is the exhaust velocity, p_e and p_a are, respectively, the nozzle exit pressure and ambient pressure, and A_e is the nozzle's exit area. The maximum thrust is achieved when p_e and p_a are equal.

The exhaust velocity U_e can be calculated by:

$$U_e = \sqrt{2\frac{\gamma}{\gamma-1}\frac{R_A}{M}T_c\left(1-\left(\frac{p_e}{p_c}\right)^{\left(\frac{\gamma-1}{\gamma}\right)}\right)}, \tag{2.3}$$

where R_A is the absolute gas constant and M is the propellant's molar mass. Consequently, for instance, higher U_e can be achieved with higher T_c and lower propellant M.

The specific impulse is defined as the thrust produced per unit of propellant consumed and calculated by:

$$I_{sp} = \frac{U_{eq}}{g_0}, \tag{2.4}$$

where g_0 is the gravitational acceleration at sea level. Thus, it is only dependent on the propellant's exhaust velocity which is dependent on the propellant and the nozzle design.

Achieving critical conditions in the nozzle (sonic conditions in the throat) is desired. The ambient pressure no longer influences the mass flow for a certain chamber pressure, stabilizing the operating conditions. The mass flow reaches its maximum allowed value and, thus, the thruster operates at high efficiency. At critical conditions, density, pressure and temperature ratios between the chamber and throat conditions follow these relations:

$$\left(\frac{p_t}{p_c}\right)_{cr} = \left(\frac{T_t}{T_c}\right)_{cr}^{\frac{\gamma}{\gamma-1}} = \left(\frac{\rho_t}{\rho_c}\right)_{cr}^{\gamma} = \left(\frac{2}{\gamma+1}\right)^{\frac{\gamma}{\gamma-1}}. \tag{2.5}$$

Thus, to ensure critical conditions, the pressure ratio (the ambient pressure divided by the chamber pressure) needs to be lower than the critical value.

By knowing the propellant conditions at the chamber, it is possible to calculate the critical mass flow $\dot{m}_{cr}$:

$$\dot{m}_{cr} = \frac{\Gamma p_c A_t}{\sqrt{RT_c}}, \tag{2.6}$$

$$\Gamma = \sqrt{\gamma}\left(\frac{2}{\gamma+1}\right)^{\left(\frac{\gamma+1}{2(\gamma-1)}\right)}. \tag{2.7}$$

where R is the specific gas constant, Γ is the Vandenkerckhove function, which depends only on the specific heat ratio γ, A_t is the throat's area, and T_c and p_c are the temperature and pressure, respectively, in the chamber.

The relation between the nozzle exit area and throat area (hereby defined as expansion ratio) determines the ratio between the exit pressure and chamber pressure. Thus, it is possible to calculate the required nozzle exit area for a defined exit pressure or vice-versa. A large pressure drop is obtained with a high expansion ratio:

$$\frac{A_e}{A_t} = \frac{\Gamma}{\sqrt{\frac{2\gamma}{\gamma-1}\left(\frac{p_e}{p_c}\right)^{\left(\frac{2}{\gamma}\right)}\left(1-\left(\frac{p_e}{p_c}\right)^{\left(\frac{\gamma-1}{\gamma}\right)}\right)}} \tag{2.8}$$

With the presented equations, the ideal performance of a nozzle can be determined. However, real nozzles are characterized by greater complexity as they are subject to several factors which are not taken into account in ideal rocket theory and affect its performance.

For instance, the divergence of the flow in the nozzle exit sections may result in varying losses, which depend on the cosine of the divergence angle; a boundary layer may form in the nozzle throat, partially blocking the flow; and unsteady combustion and flow oscillations can also lead to minor losses [16]. Additionally, combustion-related and heating loss-related correction factors are present [5]. The considered correction factors for the nozzle tool are the ones used by Takken [11].

2.3. WORK AT TU DELFT

The two main works relevant to this thesis are the experimental work by Leenders [10] and the numerical and experimental work by Takken [11].

Leenders experimentally tested solar thermal propulsion using a theatre lamp, a concentrator lens and an insulated copper RAC with a nozzle [10]. This design is named Solar Thermal Thruster 1 (STT1). The tests were performed in the cleanroom of the aerospace faculty with nitrogen as the propellant due to its availability and less strict safety requirements. The produced thrust was measured as well as the mass flow, the temperature at various RAC points and the pressure in the nozzle chamber. Takken [11] discussed the results obtained and concluded that the attained propellant temperature and specific impulse were low compared to the literature examples. Low heat transfer capacity to the fluid, low input beam power and non-adapted nozzle were the reasons given. The overall efficiency of the system ranged from 32% to 52%. Takken also mentions that the results presented by Leenders could not be entirely reproduced, elevating the importance of clearly documenting and stating all inputs, results, properties and dimensions when an experiment is conducted.

Considering his conclusions, Takken stated that there were possible improvements to be made to the STT1. Therefore, Takken's research objective was to construct the Solar Thermal Thruster 2 (STT2) and prove its feasibility by attaining a minimum specific impulse of 90.0 seconds at sea level conditions with a nitrogen mass flow rate of 300 mg/s. It is relevant to understand that this specific impulse value is significantly lower than the ones presented previously due to using nitrogen as a propellant and temperature constraints.

Takken ended up developing three prediction tools: a feed system tool (pressure drop calculation from the tank to the RAC), a RAC tool (radiation power absorption and transfer to the propellant) and a nozzle tool (calculates the expected thrust considering ideal rocket theory and correction factors from the literature). In his RAC tool, it was observed that Takken's method for estimating the percentage of beam power absorbed by the cavity was slightly flawed as the view factors were used incorrectly. This is explained in

Chapter 3 which answers this topic.

Experimentally, Takken outsourced his manufacturing process to a fellow student due to his inexperience. However, design changes made to facilitate the manufacture of the model, particularly the reduction from 6 RAC inner ducts to 1 while maintaining its size, led to pressure losses in the order of 30 bar. Moreover, significant leaks arose from the threaded connections in the RAC. These alterations rendered the STT2 model incapable of being tested and his thesis ended up not having an experimental component.

2.4. OTHER LITERATURE FINDINGS

One of the main research focuses was on the relevance of the RAC's geometry since it has a significant impact on every heat transfer mechanism. From the literature, the most commonly analysed geometries, due to their simplicity, are spherical, cylindrical and conical. Daabo et. al [17] concluded that, from the three shapes (Fig. 2.3), the conical had a better optical performance.

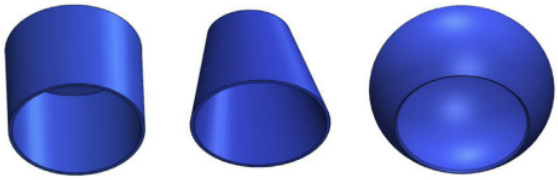

Figure 2.3: The three geometry shapes of cavity receiver studied by Daabo et. al [17].

More complex geometries were studied by Asselineau et al. [18] and showed that highly different geometries could result in similar efficiencies, despite their disparate energy distribution and temperature profiles. However, the most relevant research identified, including the two previously mentioned, is related to parabolic dish-receiver systems and solar power towers [19] [20] which is different since, for example, there is no fixed solar beam and the geometries have a unitary aperture ratio. Therefore, geometrical research is absent for beam-powered propulsion and the conclusions from the literature must be considered carefully. Nevertheless, considering the information available and geometrical simplicity, the conical, cylindrical, and cylindrical with a conical bottom appear to be the best candidates for further analysis.

The absorbed laser energy is determined by factors such as the RAC's geometry, material, surface and the laser focal distance [17] [21]. Unfortunately, no relevant research providing a model that predicts laser absorption in this scenario has been found. To address this, previous MSc students have used view factors to determine the fraction of laser energy absorbed, however, view factors are not suitable for the analysis of laser beams, as they are based on the assumption of diffuse radiation coming from all directions [22]. Consequently, establishing an accurate model for laser absorption will undeniably be beneficial for future research.

Regarding RAC duct layout, from previous work [10] [11] [23], the choice has been mainly between linear and spiral tubing. For its conical cavity, Leenders H. used linear tubing [10] while Takken A. chose spiral for its cylindrical cavity [11]. For the same cav-

ity's length, spiral tubing has the advantage over linear tubing since it can increase its contact length. Furthermore, Rohsenhow W. et al. mention that spiral flow has a higher heat transfer due to a secondary flow induced by the presence of centrifugal forces. Consequently, spiral tubing is widely used in industry [24]. However, spiral ducts are harder to manufacture compared to linear.

The amount of indirect heating laser thermal propulsion experiments available in the literature is small and recent. Japanese researchers [25] [26] used porous carbon as the heat exchanger and propellants such as helium and nitrogen achieving temperatures of 1500K at 20% overall efficiencies. The highest contributor to the low efficiency is the radiation loss from the porous carbon which is significantly high. There are more experiments published regarding solar thermal propulsion and since the setup is similar, they are valuable sources of information. Shimizu et al. [27] achieved a propellant temperature of 1850K at a 0.2 MPa chamber pressure which corresponds to 700 s of I_{sp} for hydrogen. Tucker et al. [28] used a silicon carbide heater as the heat source and achieved an equivalent hydrogen I_{sp} of 630 s.

Due to the undeniably small amount of experimental results in the literature, the beam-powered thermal propulsion field benefits from further experimental investigation. This is a crucial step in the demonstration of the technology's feasibility.

2.5. ENGINEERING PROCESS

To understand the motivation behind the thesis' research questions which are presented in the next section, a concise description of the general engineering process behind a beam-powered thermal propulsion system is given.

First, the mission determines the thruster performance requirements such as thrust and specific impulse. In addition, RAC requirements/constraints are established. Typical requirements are, for example, related to size/mass constraints and maximum operating temperature and pressure. Considering the requirements, the possible RAC configurations are defined and a down selection based on key criteria is made. Next, the analysis and optimization within the requirements of the performance of each RAC selection is done. For this, an accurate prediction model is crucial since it reduces the need for experimental testing of several options. This diminishes development costs and time.

A final comparison between the options is performed and a design is chosen for manufacturing. After manufacturing, experimental testing is done to ensure that the design performs as intended and satisfies the requirements. If the performance does not meet the expectations, adjustments to the experimental set-up or the prediction model are required.

2.6. RESEARCH QUESTIONS

From the literature study, there is a clear lack of optimization in the RAC design that might lead to higher propulsion system efficiency values. For the definition of RAC efficiency refer to section 5.1. In addition, only one student at the faculty successfully conducted experimental work and its experiment was limited by factors such as the light source [10]. Therefore, the main goal of this research project is to improve the numerical design tools of a beam-powered thermal thruster, manufacture a laboratory model and

perform experimental tests. From this goal, other subgoals appear such as achieving higher temperatures and efficiency than Leenders and testing. To achieve these goals, there are research questions that must be tackled which are presented in this section.

As mentioned, the RAC performance is highly related to the total power absorbed. However, no correct prediction method to calculate the absorbed beam power was found in the literature. Thus, the first research question addresses this absence in the prediction tools:

Q1 Can the beam power absorption be modelled to an accuracy of 5%?

This research question fits in the prediction model accuracy aspect of the engineering process mentioned previously. Without an accurate method to determine the power absorption, the predictive tool loses its value. Several sub-questions related to the results such as the effect of surface reflectivity are relevant as well.

Several variables determine the RAC's performance. One of the most concerning aspects is its geometry and surface properties, as they influence beam power absorption, emitted radiation loss, and convection loss. In addition, the ducts determine the heat transfer capacity from the RAC to the propellant. Therefore, the following is investigated:

Q2 How do the RAC and duct geometry change affect performance?

This research question focuses on familiarizing the user with the influence of each variable on performance, and, thus, allowing for a quicker and substantiated down-selection before optimization of each design.

Following the RAC geometrical analysis, the attention is focused on the possible efficiency values. The predicted efficiency determines if the model is capable of competing with similar systems and if it is worth considering. To explore this, optimization tools of the RAC performance are developed. Consequently, the following question is answered:

Q3 What overall RAC efficiency values can be achieved?

This question relates deeply to the optimization process of the designs. By developing those tools, the attainable values can be investigated.

With the RAC model and additional propulsion system components manufactured, experiments are performed to initially validate the simulation tool. Upon the gathering of the testing data and subsequent analysis, it is necessary to answer:

Q4 How does the experimental data relate to the prediction model?

This research question is related to the development of the prediction models as the data gathered allows for the validation or the need for improvement of them. Consequently, the next designs can be selected with higher chances of matching the experimental performance.

By answering all of these research questions, numerical and experimental developments in the field of beam-powered thermal propulsion are undeniably made. The prediction model becomes more accurate, the relationships between the RAC characteristics and its performance are studied deeper and experimental work is added to the existing small collection for validation of prediction tools.

3

BEAM POWER ABSORPTION THEORY

As explained in Chapter 2, there is a clear research gap in the prediction of the total beam power absorbed by the RAC. This chapter aims to present the theory behind the possible power absorption of a beam inside cavities thereby taking into account the power distribution over them and, consequently, serve as a step forward to the solution to this problem. Firstly, theoretical concepts such as beam reflections and their power distribution as well as view factors are introduced. Next, three different approaches to the problem are explained and their results and conclusions are presented. Lastly, regression models of the results are analysed.

The data used in this chapter can be found in the author's GitHub. [1]

3.1. BEAM REFLECTION

In each interaction between the cavity wall and the beam, the surface absorbs a percentage of the incoming power which depends on its surface's absorptivity coefficient, α. Thus, the number of interactions between the beam and the cavity wall is relevant to estimating the amount of energy absorbed by the cavity. This is determined by several factors such as the cavity geometry, but one of the main factors is the type of reflection the beam suffers.

Radiation reflection can be specular, diffuse and, more commonly, a combination of both [29]. In smooth surfaces such as mirrors, the first occurs and radiation reflects at the same angle of incidence; whereas in rougher surfaces, diffuse reflection occurs and the rays scatter in different directions [30]. Fig. 3.1 illustrates the difference between the two types. When a surface diffusely reflects a beam in all directions (i.e. ideal diffuse reflecting surface) it is said to exhibit Lambertian reflection [29]. Diffuse reflection increases the complexity of the incoming radiation absorption analysis [21].

[1] Thesis Github

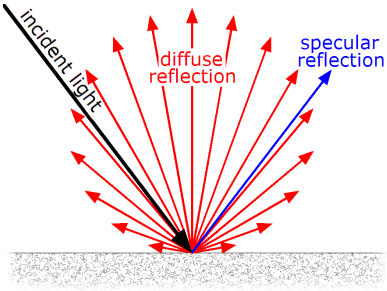

Figure 3.1: Specular and diffuse reflection. The rays represent the luminous intensity. [29]

For the Lambertian surface, the reflection probability density, in 2D and 3D respectively, is based on Lambert's cosine law [31]:

$$f(\theta,\varphi) = \frac{1}{2}\cos\theta \quad f(\theta,\varphi) = \frac{1}{\pi}\cos\theta\sin\theta, \tag{3.1}$$

where

$$\theta \,\epsilon\, \left[0, \frac{\pi}{2}\right], \quad \varphi \,\epsilon\, [0, 2\pi]. \tag{3.2}$$

Therefore, regarding specular reflection, one must know the direction of the incident light and its reflection point to predict the reflected ray. On the other hand, if the reflection is diffuse, the incident ray direction is irrelevant, only the reflection point matters. This difference is taken advantage of when developing the prediction methods.

Experimentally, the percentage of diffuse reflection of a surface (diffuse ratio) can be determined by measuring the angular distribution of light reflected from it [32]. The goniophotometer, glossmeter and bidirectional reflectance distribution function meter are examples of instrumentation that can be used for this purpose.

3.2. BEAM POWER DISTRIBUTION

Another essential aspect to consider is the power distribution within the incident beam. Most lasers have a Gaussian beam profile i.e. their beam intensity follows a Gaussian distribution (Fig. 3.2). Although less common, there are also top-hat laser beams which have near-uniform intensities.

Due to the nature of a Gaussian distribution, it is difficult to pin down a precise definition for the beam diameter. Nevertheless, the most common definition is the one that limits the width to the area whose intensity is greater than $1/e^2$ % or approximately 13.5% (Fig. 3.2). In a 3D or 2D axisymmetric beam, the released rays then comprise a fraction of about 86.5% of the total beam power. In a 2D sheet beam, this fraction is about 95.45%.

Considering θ the beam's divergence and θ_s the angle of the beam portion in question, then the power within that beam portion P_{θ_s} is, for the uniform case:

$$P_{\theta_s} = \frac{\theta_s}{\theta}, \quad P_{\theta_s} = \frac{1-\cos\theta_s}{1-\cos\theta}, \tag{3.3}$$

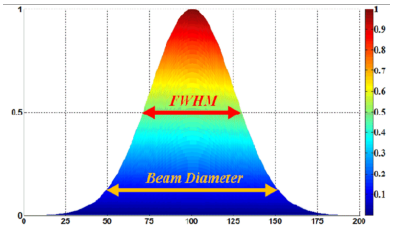

Figure 3.2: Laser beam Gaussian distribution and beam diameter.

for the 2D and 3D scenario, respectively. Concerning a Gaussian distribution beam in 3D case [33]:

$$P_{\theta_s} = 1 - e^{-2\cdot\left(\frac{\tan(\theta_s)}{\tan(\theta)}\right)^2}. \tag{3.4}$$

It is easier to understand the importance of power distribution with a practical example. Let us consider a system where the beam has a diverging half-angle of 5º and the section from 0º to 3º only reflects once in the cavity before bouncing back while the rest is fully absorbed. In the uniform distribution case, (64+36α) % of the total power is absorbed whereas in the Gaussian (40 + 60α) % would be absorbed. Additionally, the power absorption distribution throughout the cavity will have undeniable differences.

For the following sections, although the prediction methods can be adapted to Gaussian beams easily, it has been chosen to perform the simulations with a uniform beam distribution since the laser which was meant to be used has a uniform profile.

3.3. VIEW FACTORS

View factors are mathematical quantities used to determine the fraction of emitted radiation by a surface that is directly impinging on another surface [22]. They take into account the geometrical relationship between surfaces and their shape [30].

View factor calculation can be quite complicated. For complex geometries, it is not always possible to obtain the view factor algebraically [34]. In these cases, numerical methods must be used. Luckily, for the geometries being studied that is not the case. Additionally, three important and trivial relations are always respected [30]:

$$\sum_j F_{ij} = 1, \tag{3.5}$$

$$A_1 F_{12} = A_2 F_{21}. \tag{3.6}$$

$$F_{1(23)} = F_{12} + F_{13} \tag{3.7}$$

Equation (3.5) asserts that the sum of all view factors from one surface to the others equals one, as all emitted radiation is directed to some surface, maintaining energy conservation. Equation (3.6), on the other hand, pertains to the reciprocity of heat transfer

between two surfaces. It proves valuable in simplifying view factor calculations by enabling the determination of a single view factor when the other is known, particularly beneficial in intricate systems where direct calculation of all view factors might prove challenging. Lastly, equation (3.7) indicates that view factors can be added when their intersection is null, facilitating simplifications in calculations, such as those involving outer rings [34].

3.3.1. GEBHART FACTORS

The view factors, as discussed, only represent the portion of a surface's emitted radiation that arrives at other surfaces and, unless that surface is a black body, it will not absorb all the radiation and some of it will be reflected somewhere [34]. Thus, Gebhart B. developed the Gebhart factors which effectively calculate the fraction of radiation that is absorbed: it considers all the reflections [30]. Even though the calculation of these Gebhart factors requires the previous calculation of the view factors, it still requires less computational power than using Monte-Carlo ray tracing [35]. Similarly to the view factors, from [30], Gebhart factors obey to the following laws:

$$\sum_j B_{ij} = 1, \tag{3.8a}$$

$$\varepsilon_i A_i B_{ij} = \varepsilon_j A_j B_{ji}. \tag{3.8b}$$

The first equation is related to energy conservation and the second states that the rate of heat transfer between two surfaces has equal magnitude (reciprocity).

The Gebhart factors for an n-surface enclosure can be calculated by the following equation [30]:

$$B_{ij} = F_{ij}\varepsilon_j + \sum_k^n (1-\varepsilon_k) F_{ik} B_{kj}. \tag{3.9}$$

From equation (3.9), it is fairly easy to understand that it is not as straightforward as the view factors since each Gebhart factor depends on the values of others. Nevertheless, calculating the Gebhart factors is essentially solving a linear system. However, only n(n-1)/2 independent factors, in an n surface system, need to be calculated directly as the Gebhart factor algebra can easily determine the rest [30].

3.4. GEOMETRICAL CAVITY SHAPE

Several geometry types have been studied in the literature. One of the conclusions of the literature study was that the conical and cylindrical cavities appear to be the best candidates for further analysis [12]. In addition, a cylinder with a conical bottom geometry is also worth looking into: the conical bottom might lead to a higher number of reflections in the wall, improving energy distribution and beam absorption, and lower pressure losses due to not-so-significant bending. Consequently, the geometries tested in this thesis are the cylinder, cone and a mixture of the two, hereby referred to as con-cylinder geometry.

A cavity geometry can be defined fully by its aperture diameter, cavity diameter and length, and conical length (Fig. 3.3). However, when it comes to the beam reflection

and, by extension, its total absorption inside a cavity, it is the relative geometry that impacts the result. Thus, dimensional analysis is applied which allows the reduction of the number of cases analyzed while extending the applicability of results to numerous scenarios. Then, the cavity geometry is fully defined by the aperture ratio (AR), length ratio (LR) (normalized against the cavity's diameter) and cone ratio (CR) (conical length normalized against the cavity's total length). The aperture ratio and cone ratio are trivially limited to the 0 and 1 range. A cavity with a unitary cone ratio is a cone, while a cylinder has a cone ratio of 0.

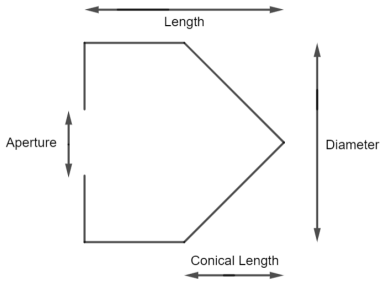

Figure 3.3: Cavity Geometry and its variables

Although not related to the geometry of the cavity, the origin of the beam is relevant to determining the absorption. To reduce the number of simulation cases, the origin o is defined by:

$$o = \frac{AR}{2\tan(\theta)}, \tag{3.10}$$

where AR is the aperture ratio and θ the beam divergence angle. Thus, The entire beam penetrates the cavity, with its outermost region tangent to the opening. This choice is made due to optimal results: the aperture wants to be as small as possible since it will increase the absorption and the inner radiation loss but without obstructing the beam because that would make it lose incoming power. Nevertheless, the methods can handle arbitrary origin distances.

3.5. RAY TRACING

In this section, ray tracing is briefly explained as well as the setup used to perform the simulations is presented. For a more detailed guide and analysis refer to the appendix A.

Ray tracing is a computational method used to simulate the propagation and interaction of electromagnetic rays [31]. Beams are modelled by dividing them into several different and independent rays. Each ray's path and different interactions with the simulation mesh are calculated. For this thesis, COMSOL was the chosen software due to its availability and familiarity to the user. Fig. 3.4 shows the COMSOL interface for ray tracing.

After selecting the Geometrical Optics model, the user can set up their variables in the parameter table, allowing for easier changes and parametric sweep of simulations.

Next, the user defines their geometry with the desired reflection type and absorption properties. The ray characteristics are set next. To decrease the computational effort slightly, termination criteria related to geometrical boundaries and remaining power in each ray are added. Lastly, the user can proceed with their simulation and when finished they can post-process the results.

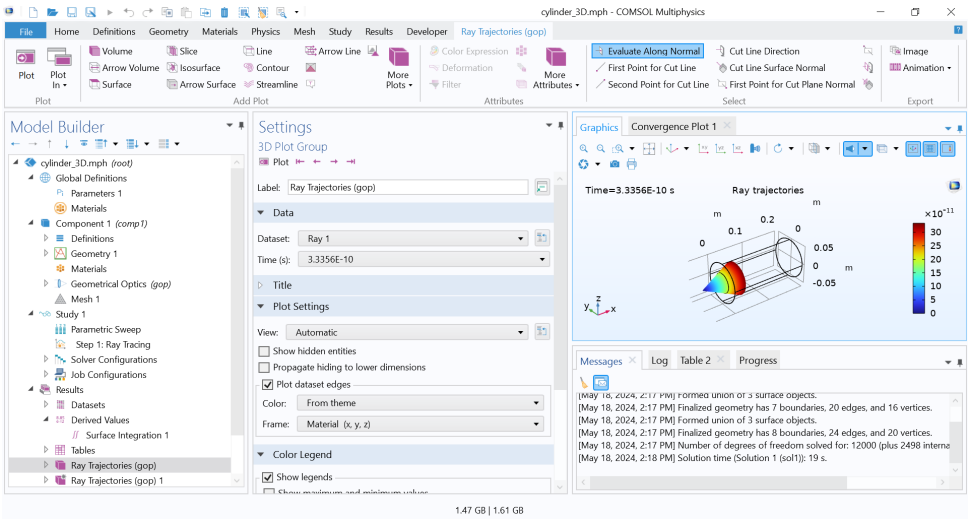

Figure 3.4: COMSOL Ray Tracing Interface - 3D Cylinder simulation

Besides the geometrical parameters, there are parameters which influence the result such as the number of rays simulated as well as the total simulation length. Sensitivity studies were performed and the decision was made taking into account computational demand as well.

Another noteworthy observation is that for the diffuse reflections, COMSOL does not split the incident ray into several with the remaining power divided amongst them after reflection, it randomizes the direction (according to the Lambertian cosine law) and keeps only one ray with the remaining power. This is done for computational demand reasons [31]. Consequently, the results of simulations with the same inputs will always vary a bit. The difference is lower as the number of rays increases due to convergence.

Table 3.1: Parameters for 2D and 3D ray tracing simulations

	2D	**3D**
α	`range(5,10,45)`	`range(5,20,45)`
ε	`range(0.1,0.1,1)`	`range(0.1,0.2,0.9)`
AR	`range(0.1,0.1,1)`	`range(0.1,0.1,1)`
LR	range(0.5, 0.25, 2.5) + range(3,1,10)	[0.5, 0.75, 1, 1.5, 2, 2.5, 4, 7, 10]
Total	8500	1350

Regarding the simulations, 2D and 3D scenarios for both specular and diffuse sur-

faces were performed for 6 different geometries (CR = [0, 0.1, 0.25, 0.5, 0.75, 1]). Thus, in total, twenty-four parametric sweeps. The parametric inputs varied for the 2D and 3D scenarios (table. 3.1) since 3D simulations took longer. Each parametric sweep took around 8 to 12 hours for the simulations to run and the post-processing of the absorption.

The number of rays stayed the same for 2D and 3D which decreased the accuracy of the 3D results due to a lower density of rays covering the beam path. This was decided since increasing the number of rays would greatly increase the computational time.

Although the ray-tracing model allows us to visualize the power distribution over the cavity surface, it appears to not be possible to couple this distribution to the heat transfer models. The literature regarding this coupling is lacking and the only alternative to simulate beam power in a heat transfer model is to manually apply the power distribution as a heat flux. However, since the distribution is not as simple as a one-reflection flux, this can not be done easily and would have to be done manually. Consequently, there is an obstacle in the use of COMSOL for the following heat transfer simulations.

3.6. THEORETICAL PREDICTIVE ALGORITHMS

In this section, the developed predictive algorithms considering the power absorption inside 2D cylindrical and conical cavities are presented. Regarding specular reflection, only the rectangular cavity scenario has been successfully developed. Since in Chapter 4 the focus is on diffuse reflection, its extensive explanation and derivation are available in Appendix B. The diffuse reflection (View Angle Method) has been investigated for both geometries and a brief explanation is presented in this section.

3.6.1. VIEW ANGLE METHOD - DIFFUSE REFLECTION

The view angle method was an attempt to theoretically calculate the total absorbed power in Lambertian surfaces. Unlike the specular rectangular case, it was not as successful. This stemmed from the complex mathematics that required numerical integral calculations. Below a succinct description of the method is given. For a more detailed overview refer to the appendix C.

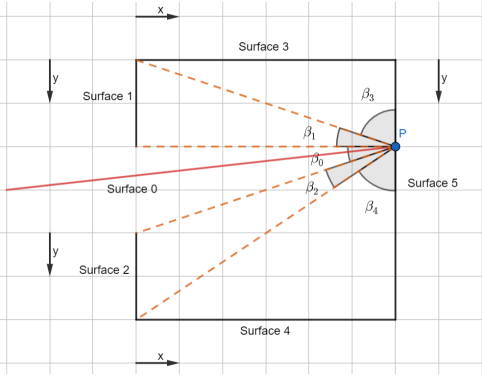

Figure 3.5: Probability of diffuse reflection inside a rectangular cavity

Fig. 3.5 illustrates the theory behind this approach. When a ray hits surface 5 at point P, the fraction of the reflected ray that goes into surface i depends on β_i and its position. This fraction can be calculated considering Lambert's cosine law. Also, the height at which it intersects surface 5, $h(\alpha)$, is a function of the incident angle α. With this information, the view angle formula from the first hit at surface 5 to surface i can be calculated. For example, the view angle from surface 5 to 3 is

$$V_{53}(\alpha, x) = \frac{1}{2} \sin \arctan \frac{L - x}{\frac{D}{2} - h(\alpha)}. \tag{3.11}$$

The view angle formula can then be integrated in terms of α and x with the appropriate boundaries to get the fraction of the beam that does a certain two-reflection trajectory.

To calculate further reflections, the view angle formulas need to be derived in terms of the surface coordinate variable. This gives information about the power distribution. In general, the formula for the fraction of the beam that hits the surface z after reflecting into n surfaces $i, j, k, ..., x, y$ is:

$$f_{ijk...xyz} = \frac{1}{\alpha_0} \int_0^{\alpha_0} \int_0^{L_j} \int_0^{L_k} \cdots \int_0^{L_x} \int_0^{L_y} P_{ij}(\alpha, j) V'_{jk}(j, k) ... \\ V'_{xy}(x, y) V_{yz}(y) dy dx ... dk dj d\alpha, \tag{3.12}$$

where L_j is the length of the surface j and V'_{jk} is V_{jk} derived in terms of k.

From the general equation (3.12), to calculate a fraction which entails n reflections, $n-1$ integrals need to be calculated and all of the functions being integrated are indirectly related, making it impossible to separate them to simplify the integration process. Also, the functions are not trivial. Consequently, the calculation process for each fraction becomes highly computationally demanding as the number of reflections goes up. Moreover, the number of integrals increases exponentially. Despite the efforts to produce a theoretical algorithm, it ended up having to be truncated to 4 reflections due to computational demand.

This method showed plenty of obstacles: several complicated formulas have to be deduced and their nature only allows for integration by numerical methods, limiting the calculation extended. Thus, it was decided to not approach the 3D case as the mathematics would be even harder. Nevertheless, the method developed in the next subsection was successful in tackling this problem.

3.7. FINITE ELEMENT METHOD

In the finite element method (FEM), the domain of interest is divided into smaller subdomains, called finite elements. Although typically used to solve differential equations in areas such as structural analysis, in this case, FEM is used to allow the determination of the absorbed power by using view factors.

The main problem with using view factors to determine the beam absorption is that view factors consider that the surface radiates equally throughout the surface. This is not true in the case of a beam hitting a surface since the power distribution is not uniform. For example, consider a cylindrical cavity in which half of the lateral surface gets hit with

a portion of the beam. Then, using the view factor of the whole lateral surface to estimate how that portion of the beam is reflected would not be accurate. What if instead of one lateral surface, the lateral surface was divided into two parts (the one that gets hit by the beam and the other) and the view factors of both were calculated and used to estimate the absorption? That would be more appropriate considering the definition of view factor but even the half that gets hit does not have a uniform power distribution. Nevertheless, it is possible to divide that half into n surfaces until the irregularity of the distribution is captured well enough, allowing the use of view factors to accurately determine the absorbed power. In Fig. 3.6, the difference between the two cases is illustrated. For the ten elements per surface, in the lateral surface, the incident ray power through the incident region goes from 75%/m^2 to 40%/m^2 and in the bottom surface from almost 91%/m^2 to 58%/m^2. Whereas, in the one-element case, the lateral surface has 30%/m^2 and the bottom has 70%/m^2. As n tends to infinity, the solution converges to its real value and at infinity it would be the view angle method from the previous chapter.

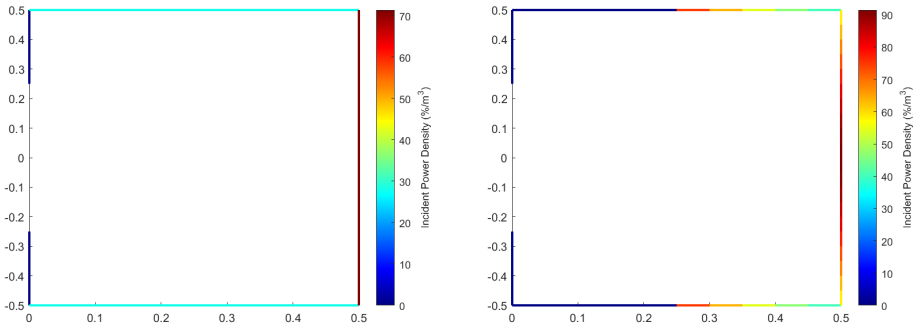

(a) Case I - only one element per surface

(b) Case II - ten elements per surface

Figure 3.6: Effect of FEM in capturing the power distribution

The view factor FEM works as follows. For each axial surface, the user can define the number of divisions each surface is divided equally into (n_1, n_2 and n_3 are the divisions of the surface 1, 2 and 3, respectively). A conical geometry has only 2 surfaces while cylindrical and concylindrical have 3. Additionally, the user defines the origin of the beam as well as the geometrical characteristics of the cavity. Then the algorithm calculates the Gebhart factors for each sub-surface and how much beam power each sub-surface gets hit initially. Next, with those two pieces of information, the total beam power absorbed by each sub-surface and the amount that left the cavity are calculated.

Regarding computational demand, the 2D and 3D scenarios differ only in the view factor formulas and, thus, no increase is observed. Moreover, the time required for the simulations is drastically lower than ray-tracing. For example, with 100 nodes on each surface, one parametric sweep takes around 30 minutes, a substantial decrease from 8 to 12 hours.

Unlike the previous methods, FEM gives information about the absorbed power distribution since the absorbed value for each node is known. This is extremely useful as it

allows accurate determination of the equilibrium temperature as will be seen in the next chapter. Moreover, for example, accurate transient temperature simulation can also be performed and information for other studies, such as structural, can be provided.

3.7.1. SENSITIVITY ANALYSIS

Due to its numerical nature, the result of the FEM developed depends on the number of surface divisions. Naturally, the value obtained approaches the real absorption value as the number of divisions increases. However, for a cylinder, there are three surfaces and, thus, three variables for the divisions. Therefore, it is relevant to understand each variable's importance by performing a sensitivity analysis.

Firstly, it is necessary to determine what the considered real value is. For that, higher numbers are continuously tested until their increase does not result in significant changes in the outcome. The value obtained by dividing the three surfaces by 500 nodes each was set as the real absorption value after comparison with the 100 nodes case. The relative difference between the two cases had a 0.0032% mean and 0.03% standard deviation.

After setting the real value, it is now possible to perform sensitivity analysis. First, the scenario where only one node is set for each surface is examined. The relative error between the real value and that case is illustrated in Fig. 3.7. Although a significant portion of the data is around the 0 mark, there is an undeniably large amount of configurations where the values are too far off.

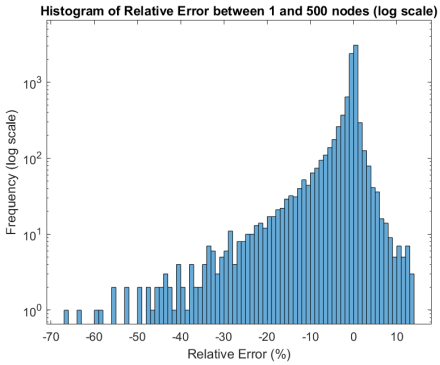

Figure 3.7: Relative error of 1 node per surface

After closer examination, it is concluded that most cases further away from the real value share common characteristics. First, lower absorptivities lead to higher discrepancies which is expected. Lower absorptivity values increase the importance of internal reflections whose calculations depend on the view factors which are too simplified with only one node per surface, also lower absorptivities lead to lower absorption percentages and thus any absolute changes are bigger in percentage. Another aspect in common is the incident angle: higher values result in bigger errors. This can be explained by the fact that a higher angle expands the distribution of the incident radiation which cannot be accurately taken into account with only one node. In addition, higher aperture and length values contribute to bigger errors in the same way: incident energy distribution

is not as focused. These conclusions substantiate the importance of not simplifying the absorption calculation.

Next, the impact of increasing the number of nodes on only one surface was studied. The increase in only the number of nodes on either the bottom surface or the top surface led to no significant improvements. On the other hand, increasing the number of lateral surface nodes led to irrefutable improvements. Consequently, it is clear that, in these circumstances, the feature with the highest impact on the algorithm is the number of nodes in the lateral surface. It can be intuitively explained by the huge difference in Gebhart factors along the surface and the increase in discretization of the incident radiation.

Then, increasing the node number on all surfaces was studied. The relative error converges to zero as the nodes are increased similarly to the lateral nodes case. Nevertheless, as the node number increases, the convergence is better than the lateral-only case whose convergence appears to stagnate. Therefore, the relevance of increasing the number of nodes in the bottom and top surfaces is evident, despite their undeniable lower importance.

For this specific scenario of beam origin and geometrical dimensions, 100 nodes per surface is a good rule of thumb. Despite not requiring high computational effort, the user might want to compromise accuracy for simulation time if more scenarios are to be studied. Thus, no general rule for the necessary number of nodes is defined since it ends up being a trade-off between accuracy and computational demand. Also, a greater length might require more lateral nodes and a beam origin closer to the RAC might require more bottom nodes. Besides understanding that the lateral nodes are of most importance, the desired number of nodes should be investigated by the researcher within its inputs of interest by increasing the nodes and comparing the relative difference and computational demand increase between iterations.

3.8. VERIFICATION

In this section, the results obtained with the specular algorithm and the FEM method for diffusing surfaces are verified with the ray tracing result simulations. Firstly, the specular case for the cylinder is examined and then the 3D diffuse case is presented to all geometries. Unfortunately, for the conical and concylindrical geometries, no algorithm as capable as the one for the cylindrical cavity could be developed. Therefore, the results of the ray tracing are used in the following stages and cannot be verified by any other method.

3.8.1. SPECULAR REFLECTION

As mentioned and explained previously, an algorithm was constructed to calculate the total power absorbed in the cylindrical cavity with specular reflections scenario. Thus, the simulation results can be validated by the algorithm itself. The relative difference formula used in this case is:

$$\varepsilon_{rel} = \frac{P_{sim} - P_{algo}}{P_{algo}}, \tag{3.13}$$

where P_{sim} and P_{algo} are the absorbed beam power values obtained from the ray-tracing simulation and algorithm, respectively. Consequently, positive values of ε_{rel} occur when the ray tracing result exceeds the algorithm.

In Fig. 3.8a, a boxplot of the relative error between the simulation and algorithm results for the 2D and 3D cases is presented. Regarding the 2D scenario, the values are undeniably close to each other: the median is 0 and the spread is negligible (under 0.1%). Consequently, the algorithm for the 2D is verified by the ray tracing results. On the other hand, the 3D case shows a higher spread with a median also close to zero. This spread can be easily justified by lower ray density in the 3D simulations. Consequently, it is expected that by increasing the number of rays in the 3D scenario, the relative error distribution converges to 0. Nevertheless, the distribution is irrefutably still within a small interval (2% spread, which is within the research question value), verifying the results.

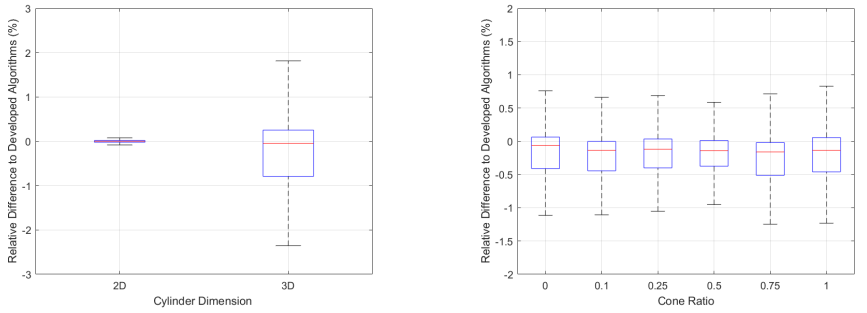

(a) Ray-tracing vs Specular Cylinder Algorithm

(b) Ray-tracing vs FEM results in diffuse surfaces

Figure 3.8: Method Verification via relative error

Regarding the conical and concylindrical geometries, since the ray-tracing results for the cylindrical case performed well, it is reasonable to expect these to not be significantly far in terms of performance.

3.8.2. DIFFUSE REFLECTION

With the development of the FEM for the absorption of diffuse surfaces, these results can be verified by the results of the ray-tracing simulation. Only the 3D cavity case is presented. Although 2D FEM was also formulated, these bear no interest in the following stages and, thus, their verification is not shown here to avoid repetition. Additionally, the view angle method is not used in this section due to its limitations.

Considering that the ray-tracing results' accuracy was reduced to reduce simulation time but staying within at least 5% of the higher demand simulation result, an acceptable difference between the two is of the same order since the FEM model results should be within 0.09% (three standard deviation interval) of the real result.

In Fig. 3.8b, the relative error between the ray tracing and the FEM results of all geometries is presented in boxplots. For all the geometries, the relative error is smaller than the acceptable difference with similar distributions. Consequently, the developed FEM is verified.

3.9. RESULTS AND ANALYSIS

In this section, the results obtained for all the studied scenarios are presented and discussed. First, the total possible absorption is shown followed by a study on the effect of each variable. Next, the effect of surface reflectivity is demonstrated and the comparison between geometries is made. Finally, we analyze the differences from the previous method's results to highlight the relative improvements achieved. The power distribution analysis is not performed in this thesis and is considered future work.

3.9.1. TOTAL ABSORPTION

In Fig. 3.9, the percentage of total incident power absorbed by the cavity is shown for all the studied inputs. This comparison includes both the specular and diffuse scenarios across all geometries. The trivial unitary absorptivity case has been deleted from this plot.

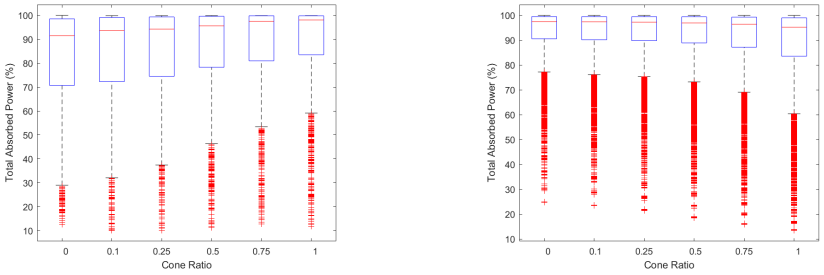

(a) Specular Scenario

(b) Diffuse scenario

Figure 3.9: Total absorbed beam power percentage by geometry

The data indicates that absorption values close to 100% can be achieved. In all boxplots, the mean is above 90%, signifying that high absorption values are typical and not outliers. However, there are still some considerably low values present, underscoring the importance of performing this estimation to confirm that the designed model achieves high absorption.

To better understand the relationship between the parameters and the total absorption, a deeper analysis of each variable effect is made in the next subsection.

3.9.2. VARIABLE EFFECT

To study the effect of each variable, the total absorption is grouped in the same categories and plotted in boxplots to study the trends. The diffuse scenario is shown below (Fig. 3.10) and the outliers were removed to emphasize the trend. For the specular scenario plots, refer to the appendix D.1.

Regarding the incidence angle (Fig. 3.10a), there is a negative trend with its increase. However, it is not as accentuated as other variables. This reduction is expected due to areas closer to the cavity and, thus, with higher exit Gebhart factors being hit. The absorptivity has an undeniably high effect on increasing the absorption (Fig. 3.10b). It is also expected since it determines the power absorption in each reflection. Concern-

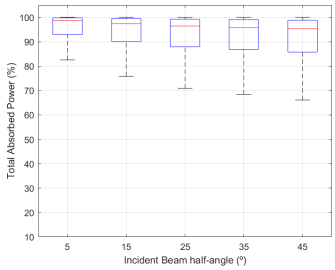

(a) Effect of incident beam angle

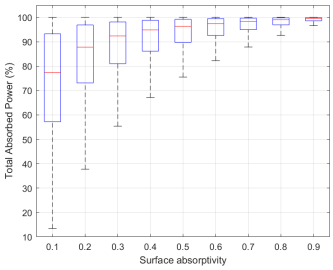

(b) Effect of surface absorptivity

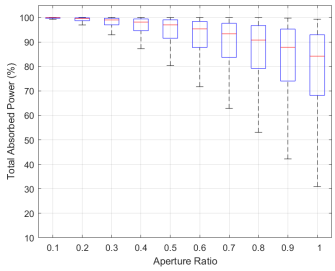

(c) Effect of aperture ratio

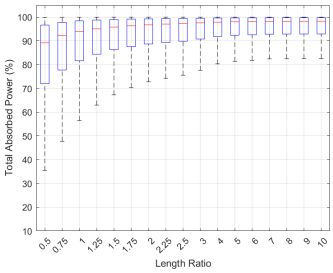

(d) Effect of length ratio

Figure 3.10: Variable effect on total absorption percentage diffuse reflection of all geometries.

ing the aperture ratio, it presents a similar trend to the absorptivity but in an opposed way (Fig. 3.10c). Lower aperture ratios lead logically to a higher number of reflections and, thus, higher absorption values. Lastly, the length ratio has a clear logarithmic positive effect with the major differences being in the early numbers (Fig. 3.10d). Higher lengths lead to the areas being hit to have a lower exit Gebhart factor and, thus, increasing absorption. However, this effect appears to have diminishing returns. After plotting the same graphs by geometry, the aforementioned trends were confirmed to not change with it.

With specular reflection (appendix D.1), the absorptivity, aperture ratio and length ratio trends are similar. On the other hand, for the incident beam angle, its increase leads to a still small but rather positive trend in total absorption. However, when analysing each geometry, this trend changes: as the geometry approaches a cone it goes from small positive to small negative. This results from the difference that for specular reflection the angle of incidence in reflections matters. In a cylindrical structure, a higher incidence angle reflecting into its lateral surface leads to a higher number of lateral reflections before leaving the cavity. Thus, this positive trend emerges. But for a conical cavity, since the lateral surface has an angle, as the incident beam angle increases the first reflection approaches the cavity, leading to lower absorptions.

To sum up, the aperture ratio and absorptivity present the highest influence on the total power absorption. While the length ratio shows a positive effect but with diminishing returns, the incident beam angle shows the smallest influence but its direction

depends on the type of reflection and geometry.

3.9.3. SURFACE REFLECTIVITY

As mentioned before, the reflection of the rays and, thus, the total absorption of the incoming radiation energy depends on the surface reflectivity. To study this effect, the results for the same geometrical and absorptivity conditions are compared to when the surface is considered fully specular and fully diffuse. The comparison is mainly driven by the relative difference between the two cases which will be defined as follows:

$$\varepsilon_{s.r.} = \frac{P_{dif} - P_{spec}}{P_{spec}} * 100, \tag{3.14}$$

where $\varepsilon_{s.r.}$ is the relative difference between the absorbed power in the diffuse case and the specular case, P_{dif} and P_{spec} respectively. Consequently, positive $\varepsilon_{s.r.}$ values equal a higher absorption in the diffuse case.

In Fig. 3.11, the relative difference in absorption due to surface reflectivity is illustrated for all the geometries studied with boxplots. The outliers have not been removed to show the extreme difference that can occur from this change. Firstly, it is evident that the surface type appears to play an undeniable part in some scenarios. This is shown by the numerous high-value outliers, going as high as 800% and as low as -50%. Despite the high variation in certain cases, the medians stay close to 0%, starting at 5% for the cylinder case and monotonically decreasing as the cone ratio increases, reaching -0.8%. This closeness to 0% can be caused by the influence of the high absorptivity cases (where the total absorption is less sensitive in percentage to the number of reflections). Another remark is that as the cone ratio increases, the interquartile ranges decrease and the outliers seem to reduce their distance. Consequently, the surface reflectivity seems less relevant for more conical shapes.

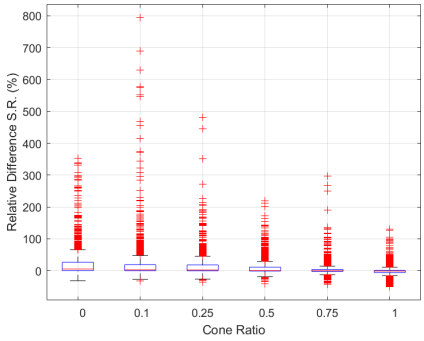

Figure 3.11: Relative difference in absorption between the specular and diffuse case for all the geometries studied.

Next, the influence of each input variable is studied more closely to understand if any particular aspect determines the difference between the two scenarios. The boxplots for

this data are available in the appendix D.2. The conclusion from this analysis is given below.

In all geometries, the input variable with the most influence is the absorptivity. At high absorptivity values, the difference can be rather small. Additionally, one geometry's results can be influenced by one certain input that other geometry does not show any influence. For example, the cylinder shows a trend with the angle of incident whereas the cone does not. Moreover, the aperture ratio increase tends to cause an increase in relative difference in a cylinder, whereas a cone tends to lower the relative difference.

To sum up, the difference in absorption between the specular and diffuse cases can be extremely significant. The relative difference is affected differently by the variables depending on the geometry. Consequently, the surface reflectivity is quite a relevant factor to take into account experimentally whose effect can only be reduced effectively by high surface absorptivity.

3.9.4. GEOMETRY

In this subsection, the effect of the geometry on the total radiation absorbed in diffuse reflections is studied. To quantify the difference, for each set of inputs the value obtained is compared to the absorbed value in a cylindrical configuration with equal inputs. The formula is set so that positive values mean higher absorption than the cylindrical case and negative values lower.

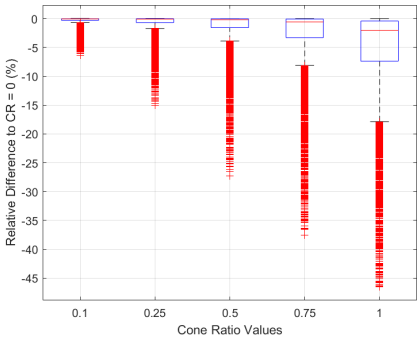

Figure 3.12: Relative difference between cylinder and other cone ratios with diffuse reflection

In Fig. 3.12, the results for each geometry are shown via boxplot illustration. The outliers have not been removed to highlight the possible differences. Firstly, the maximum of each distribution is practically 0% (the highest is 0.04% at a 0.1 cone ratio and it decreases to 0.01% as the cone ratio increases). Thus, for any input, the cylindrical cavity undeniably shows the highest absorption. Additionally, as the cone ratio increases, the median decreases and the spread increases. For example, the maximum relative difference is around the -45% mark which is undeniably significant. Consequently, shifting from a cylindrical geometry towards a conical one leads to lower absorption values as well as a higher chance of the difference being more significant.

In Fig. 3.13, the difference between the absorbed power of a cylinder and a cone is

plotted against each input. By looking at the angle plot (Fig. 3.13a), there is no significant trend and, thus, does not affect the difference between the two geometries. On the contrary, an absorption increase tends to diminish the difference between the two geometries, as expected (Fig. 3.13b). Regarding the aperture ratio (Fig. 3.13c), it has a similar but opposite effect as the absorptivity. Lastly, the length ratio also affects the disparity between the two geometries (Fig. 3.13d). The mean goes from -8% to -0.6% in a somewhat logarithmic way and most significant is the decrease in the central spread of the data.

All of the other geometries show the same trend for the absorptivity, and aperture and length ratios with the difference that at lower cone ratio values the plots converge faster and to a value closer to zero. However, in the angle plot, contrary to the cylinder versus cone one, the difference tends to reduce its spread as the angle increases. This trend is more evident at lower cone ratio angles but not as significant in absolute terms as the other trends present.

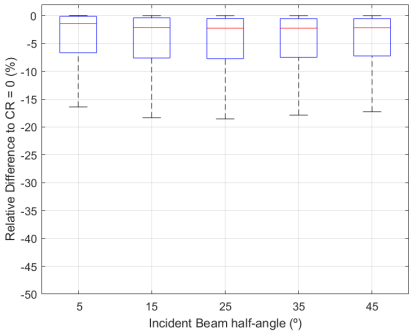

(a) Effect of incident beam angle

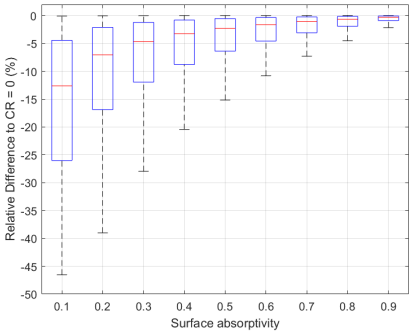

(b) Effect of surface absorptivity

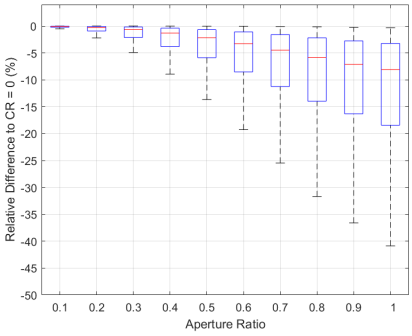

(c) Effect of aperture ratio

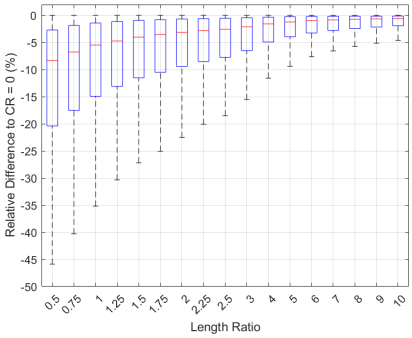

(d) Effect of length ratio

Figure 3.13: Boxplot of the effect of each input variable in the relative power absorption difference between cylinder and cone

3.9.5. COMPARISON TO PREVIOUS METHODS

As mentioned previously, Takken [11] predicted total power absorption in a quick but rather incomplete manner. Below, his method's results are compared with those obtained through the developed FEM in terms of relative difference to the FEM case. This comparison focuses solely on the diffuse scenario with conical and cylindrical geometries, as Takken's calculations were specific to these cases.

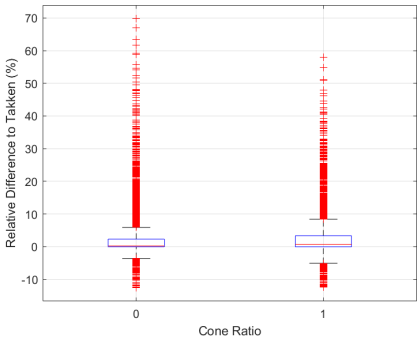

Figure 3.14: Relative difference between FEM and Takken's method

Fig. 3.14 shows the relative difference between the 500 node FEM result and Takken's method for a cylinder and a cone. A positive result means that Takken's result is higher than the FEM. The trivial unitary absorptivity scenario has been eliminated. For both geometries, the mean is close to zero and the spread is slighter bigger in the conical case. In both geometries, Takken's method has a clear tendency to overestimate the result and the outliers (which are 10-15% of the data) can achieve significant values. Despite the difference between the results generally not being considerable, since Takken's approach tends to overestimate the results, it could lead to a design that in reality performs worse.

The effect on the relative difference of each variable is presented in Fig. 3.15. The increase in angle leads to an increase in the overestimate of Takken's result (Fig. 3.15a. This is expected since Takken's method does not take into account the angle and as the angle increases, the FEM result decreases. Absorptivity and aperture ratio predictably show the usual tendency (Fig. 3.15b and 3.15c). Lastly, the length ratio spread initially decreases but starts increasing around the unit mark.

In conclusion, there is a clear difference between the two methods' results, despite being small in the cases where the absorption is high. Moreover, Takken's method shows a tendency to overestimate the total absorption in scenarios where this is low. This could cause design errors. Also, these differences in prediction could exacerbate RAC temperature estimates due to inaccurate incident power distribution.

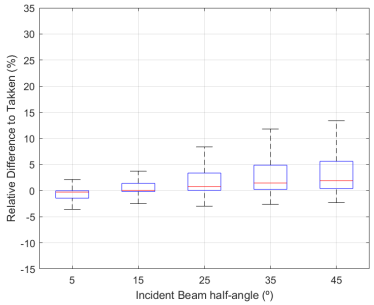

(a) Effect of incident beam angle

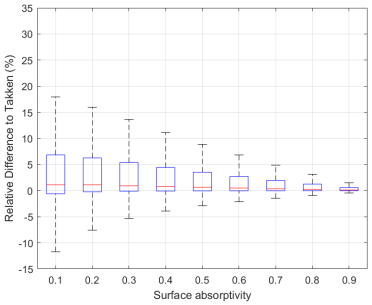

(b) Effect of surface absorptivity

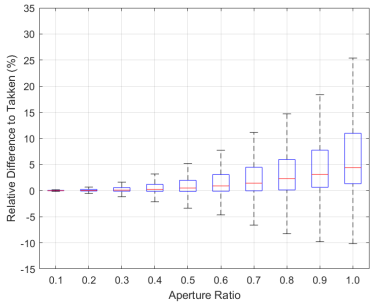

(c) Effect of aperture ratio

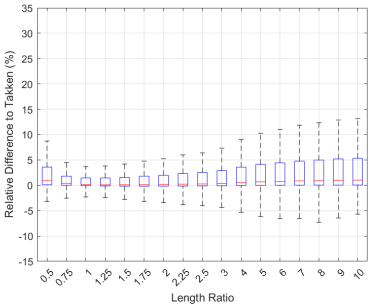

(d) Effect of length ratio

Figure 3.15: Variable effect on relative difference to Takken's estimate in both geometries

3.10. MODEL REGRESSION

Regression models are created with the data gathered from all the simulations to extend the prediction domain. These are mainly needed for the scenarios for which algorithms were not developed: non-cylindrical specular surfaces. The available MATLAB regression learner app is used to train different models from linear to neural networks to the data.

Initially, linear regression models are used as they give a better understanding of the influence of each input variable. However, first-order regression models get no better than 0.6 R^2 range and second-order, although reaching 0.9 R^2 values, has too many terms to make sense of them.

By using the regression learner app, more complex regression models were available to train without any additional difficulty. A five-fold cross-validation method is used, protecting against overfitting. The training time for each run (i.e. one geometry and one surface type) took around 15 and 30 minutes for specular and diffuse reflection, respectively. This difference emerges due to the difference in data size. In tables 3.2, the best regression model fit and its characteristics for each geometry and their reflection type are presented.

From table 3.2, the usual best fits are Gaussian Process Regression (GPR) models and

Table 3.2: Best regression model for each geometry depending on surface reflection

	Specular			Diffuse		
CR	Reg. Model	RMSE	R^2	Reg. Model	RMSE	R^2
0	GPR Rat. Quad	1.272	1.00	GPR Matern 5/2	0.093	1.00
0.1	3-layer Neural	3.2551	0.98	GPR Rat. Quad.	0.090	1.00
0.25	GPR Rat. Quad	3.9041	0.97	GPR Matern 5/2	0.090	1.00
0.5	Wide Neural	3.1451	0.98	GPR Matern 5/2	0.092	1.00
0.75	GPR Rat. Quad	4.27	0.95	GPR Matern 5/2	0.101	1.00
1	3-Layer Neural	2.9568	0.98	GPR Matern 5/2	0.106	1.00

neural networks such as the wide and trilayered neural networks. The diffuse scenario has undeniably better regression fits. The more drastic change in specular surface absorption results with geometry than diffuse is probably the main reason for this difference. Moreover, the smaller data size can play a part in this as well. Nevertheless, the fit values are undeniably satisfactory.

To sum up, regression models were fit to the available data successfully. These are mainly needed for the following chapters in the cases where only ray tracing was possible - cylindrical and concylindrical with specular reflection. For the others - the three geometries with diffuse reflection and the cylindrical with specular -, two options are available: the regression models are simpler and faster to use but the algorithms will undeniably provide the correct result.

3.11. CONCLUSIONS AND FUTURE WORK

In this chapter, we address the research gap in estimating the total power absorbed by open cylindrical, conical, and concylindrical cavities. A preliminary overview of beam properties and view factors is provided, given their critical role in the prediction methods employed. We then explain the three methods explored: ray tracing, theoretical prediction, and finite element method (FEM). Verification, presentation, and analysis of the results are conducted, followed by training regression models for future use.

Each prediction method has its advantages and disadvantages. The COMSOL ray tracing model is user-friendly, allows for the analysis of complex geometries, and is essential when other alternatives are not available. However, it is computationally demanding, resulting in significant simulation times. The theoretical predictive algorithms succeeded only in the case of specular reflection within a cylindrical cavity, offering a substantial time-saving over ray tracing. The diffuse reflection scenario, despite its mathematical complexity and initial lack of success, led to the development of the FEM approach. The FEM code effectively estimated absorption in the diffuse case for the studied geometries, providing a faster and more accurate alternative to ray tracing. The comparison between simulation times can be seen in table 3.3, highlighting the improvement with the FEM model. Additionally, it offered spatial information about the absorbed power, useful for subsequent steps.

Ray-tracing results confirmed the validity of the developed algorithms. Absorption values exceeding 90% are achievable even at low absorptivity levels. Among the four pa-

Table 3.3: Comparison of the average simulation time for one simulation (t_s) for different simulation methods. - 10k rays and 100 nodes per surface

	Ray-tracing 2D	Ray-tracing 3D	FEM
t_s (s)	3.4-5	21-32	0.2-0.25

rameters (incident beam angle, absorptivity and aperture and length ratio), the incident beam angle had the least impact, while absorptivity and aperture ratio had the greatest. Surface reflection type significantly affected absorbed power, though inconsistently, underscoring the need for precise estimation using these methods. Geometrically, a higher cone ratio generally resulted in lower absorption. A comparison with Takken's method revealed that his approach tends to overestimate absorption, but the difference is typically less than 10%. Regression models were successfully trained to fit the existing data, with better results for diffuse surface scenarios.

In conclusion, this work successfully bridged the research gap by enabling accurate estimation of beam power absorption by cavities with the studied geometries. Future work could involve developing the theoretical model for specular reflection in non-cylindrical models, incorporating power distribution into specular prediction models, and expanding the FEM code to include other geometries such as spheres.

4

Receiver-Absorber Cavity Performance Prediction Tools

Developing accurate prediction tools for preliminary design in engineering is essential for optimizing performance, reducing costs, and ensuring reliability. These tools allow engineers to make informed decisions early in the design process, identifying potential issues and analysing design concepts quickly and efficiently. By providing quick estimates, prediction tools bridge the gap between theory and practical implementation, streamlining the path from design to prototype.

In this chapter, the developed RAC performance prediction tools for indirect heating and direct propulsion are explained. The geometries considered are cylindrical, concylindrical and conical since these are the ones that have been extensively and justifiably studied. The code developed is available on the author's GitHub [1].

First, the heat transfer mechanisms at play are outlined. Understanding radiation, convection, and conduction is crucial for effective thermal modelling of the RAC. Next, their implementation in two different analytical tools is explained: the zero-order model and the finite element method (FEM) model. Each tool has its assumptions and capabilities, offering unique insights for RAC system design. Regarding the zero-order model, the approach is mainly based on the work of Takken [11]. Lastly, the models are verified by conservation of energy, comparing the results against predictions and other previously developed models.

4.1. Heat Balance

Thermal equilibrium is the state in which there is no net flow of heat between the system and its surroundings [22]. In other words, the rate of heat flow into the system, Q_{in}, is equal to the rate of heat flow out of the system, Q_{out}:

[1] Thesis Github

$$Q_{in} = Q_{out} \Leftrightarrow \Delta Q_{syst} = 0. \tag{4.1}$$

The equilibrium temperature of a system depends on a variety of factors, including its geometry, the temperature of its surroundings and the thermal energy process involved. In the RAC's case, the Q_{in} is the total absorbed beam power which was analysed in the previous chapter, whereas the Q_{out} formula components such as radiation and convection losses are described in the following sections.

While the equilibrium temperature provides a steady-state understanding of the system, it is crucial to consider the transient evolution of temperature to capture the dynamics of the system when conditions change. For instance, consider that the RAC is at a certain equilibrium temperature T_0 without any incident beam power. As soon as the beam hits the RAC, the net flow of heat is no longer zero and the temperature evolves towards the new equilibrium temperature T_{eq}. This transient analysis is described by the following equation [36]:

$$\frac{dQ_{RAC}}{dt} = m_{RAC} c_p \frac{dT_{RAC}}{dt}, \tag{4.2}$$

where m_{RAC}, T_{RAC} and c_p are, respectively, the RAC's mass and temperature, and the specific heat capacity of the material. The main result from equation (4.2) is that the temperature increase rate depends on the system's mass and specific heat capacity of the material. For an equal amount of energy, greater m_{RAC} and greater c_p imply a lower increase rate in temperature. Thus, it is advantageous to optimize for lower mass and low c_p if fast start-up times are, for example, a concern.

However, the RAC's specific heat capacity and mass do not affect its final equilibrium temperature. Other factors such as its geometry, that affect the amount of energy being lost are the ones that determine the final equilibrium temperature.

4.2. THERMAL RADIATION

Thermal radiation is the process by which heat energy is emitted as electromagnetic waves, primarily in the infrared spectrum, from the surface of an object due to its temperature [37]. Unlike conduction and convection, thermal radiation does not require a medium to transfer energy and, thus, occurs in a vacuum.

The rate of heat transfer by emitted radiation by a surface, Q_r, is determined by the Stefan-Boltzmann law of radiation [36]:

$$Q_r = \sigma \varepsilon A_{surf} \left(T_{surf}^4 - T_{amb}^4 \right), \tag{4.3}$$

where σ is the Stefan-Boltzmann constant, ε is the surface's emissivity, A_{surf} is the surface's area, and T_{surf} and T_{amb} are the surface's and surrounding's temperature, respectively. Furthermore, the emitted radiation from surface 1 that hits surface 2 Q_{12} requires the addition of the Gebhart factor term B_{12}:

$$Q_{12} = B_{12} \sigma \varepsilon A_{surf} (T_{surf}^4 - T_{amb}^4). \tag{4.4}$$

The RAC experiences thermal radiation losses which can be significant due to its high temperature. The two sources of energy loss via thermal radiation are the cavity's inner wall and the RAC's exterior wall.

Regarding the inner wall's radiation loss, this will be highly determined by its geometry, more specifically, its Gebhart factors, and its surface's emissivity. Due to it being a cavity, some of the emitted radiation will be absorbed by another surface. By minimizing the radiation able to escape, the RAC's efficiency can be improved.

The exterior wall does not have the same ability to reabsorb some of the emitted radiation and the main factor for its loss will be its temperature, area and emissivity. Thus, it is interesting to analyze how the temperature could be lowered in the outer wall or how it could be insulated. For instance, MLI insulation, which is highly used in the space industry, could be applied to reduce drastically the radiation losses [38]. Additionally, Leenders [10] used Saffil M-Fil insulation whose properties can be found in its data sheet [39]. In his experiment, Leenders got a temperature increase between 150 and 200 K by implementing the insulation [10].

4.3. CONDUCTION

Conduction is the process of transferring heat through a solid material through molecular interactions [36]. In the RAC's case, this process involves both axial and radial conduction in its wall.

The rate of heat transfer is dependent on the thermal conductivity k of the wall material, the temperature gradient between the two points and the cross-sectional area. From [36], the general equation for thermal conduction is:

$$Q_{cond} = -kA_x \frac{dT}{dx}. \tag{4.5}$$

Regarding radial conduction, concerning a cylindrical shell, Zandbergen [5] provides a steady-state unidirectional conduction formula:

$$Q_{cond} = \frac{2\pi kL}{ln\left(\frac{r_o}{r_i}\right)} (T_i - T_o), \tag{4.6}$$

where L is the cylinder's length, r the radius and the subscripts i and o the inner and outer surface, respectively.

On the other hand, radial heat transfer in a cone is a more complex situation due to its varying radius and, consequently, there are no theoretical solutions. Ray S. et al. investigated this situation and came up with correlations for the equivalent inner radius of the cylindrical shell to quickly calculate a cone's heat conduction [40]. A possible alternative could entail using the cylindrical shell formula by dividing the cone into enough segments such that their radial variation is not significant, allowing for the approximation.

Concerning axial conduction, for a hollow cylinder with radius r, thickness t and length L, the conduction from side A to B follows trivially from equation (4.5):

$$Q_{cond} = k\pi \left(2tr + t^2\right) \frac{(T_A - T_B)}{L} \approx 2k\pi tr \frac{(T_A - T_B)}{L}, \tag{4.7}$$

where the final approximation is valid if $r \gg t$. Whereas, for a hollow cone section with radial thickness t, initial and final radius r_A and r_B, respectively , and cone half-angle θ:

$$Q_{cond} = \frac{2\pi k t \tan\theta}{\ln \frac{2r_B+t}{2r_A+t}} (T_A - T_B) \approx \frac{2\pi k t \tan\theta}{\ln \frac{r_B}{r_A}} (T_A - T_B). \tag{4.8}$$

When θ approaches 0, the cone approaches a cylindrical configuration and its axial conduction formula should approximate to the cylinder case. This is, in fact, true, verifying the formula. The final approximation can be made if $r_A \gg t$.

Previous prediction tools developed by Leenders [10] and Takken [11] ignored both the RAC's wall axial and radial conduction phenomenon by assuming that the small size and high thermal conductivity would result in a uniform temperature. Takken explains that this approximation is valid due to the material's high thermal conductivity and to support his claim, he further points out that all the temperature data points from Leenders are close. However, Leenders H. only measured outer wall temperature points, which differ by a maximum of around 40K, and it would be more relevant for the claim to have access to the inner wall temperature.

In the FEM tool developed in this thesis, the RAC's inner wall conduction is considered which constitutes an improvement from previous versions. Thus, the uniform temperature assumption can be studied and verified beforehand. If it is not verified, the temperature's spatial distribution can be studied. Regarding the RAC's inner to outer wall conduction, this is not yet implemented to not increase significantly the computational demand of the tool as the number of nodes would duplicate (inner and outer node). Thus, the inner and outer temperatures are considered the same. Given the usual small thickness and high thermal conductivity of the material, this assumption is reasonable. Nevertheless, further iterations should implement it for confirmation purposes.

Conduction was taken into account in previous models if and only if insulation was considered [11] [10]. Since the insulation's temperature is the one determining the outer temperature and, by extension, its outer radiation and convection loss, it is relevant to know how much heat is transferred to it. The conduction through the insulation is set equal to the power that is lost due to convection and radiation at the outside of the insulation:

$$Q_{ins,cond} = Q_{ins,rad} + Q_{ins,conv}. \tag{4.9}$$

By knowing the RAC's temperature, this relation can be solved numerically to determine the exterior losses.

In the FEM tool developed, insulation has not been implemented. To add it, conduction would need to be considered by adding an extra layer of nodes and their governing equations adapted.

4.4. CONVECTION

Convection is the heat transfer mechanism related to the transfer of heat between a bounding surface and a fluid in motion or across the flow plane within the interior of the fluid. When the fluid motion is caused by, for example, a pump or a fan, it is called forced convection, and, when the fluid motion is caused by density differences due to

temperature differences, it is named natural convection [24]. Convection is governed by Newton's law of cooling:

$$Q_c = h_c A \Delta T, \tag{4.10}$$

where Q_c is the convection rate of heat transfer, h_c is the convective heat transfer coefficient, and ΔT is the temperature difference whose formula depends on the situation [24]. The value of h_c can vary drastically depending on several factors such as geometry and temperature, and it can be calculated by:

$$h_c = \frac{Nu \cdot k}{L_s}, \tag{4.11}$$

where k is the fluid's thermal conductivity, L_s is the characteristic length which depends on geometry, and Nu is the Nusselt number [5]. There are several empirical relations to calculate Nu which depend highly on the scenario. In this case, Nu is obtained from formulas related to heat transfer in fluid flow in ducts.

The RAC will experience natural convection in its inner cavity and outer wall. On the other hand, forced convection occurs inside the propellant tubes from the hot wall to the fluid. For the relevant findings in the literature study about these phenomena applied to cylindrical and conical geometries, refer to the literature study section available in the appendix E.

Due to the irrefutable high complexity of the relationships found for inner and outer convection loss, it has been decided to not add to this FEM model iteration. It is, then, considered that the RAC is in a vacuum. A possible way to add this feature is to calculate the losses considering a one-point body (i.e. weighted-average temperature) and then apply those losses proportionally to each node's area and temperature. They are applied, however, in the zero-order tool since it does not have spatial dependency.

4.5. ZERO-ORDER MODEL

The zero-order model is the simplest approach to developing the RAC tool. The name derives from the fact that the RAC is treated as a single point, with its properties such as temperature being averaged out. Thus, the model does not introduce any spatial dependency.

In his thesis, Takken [11] developed a zero-order model that served as an inspiration for this work. Takken's model was taken as a starting point and changes/additions were made. For example, the properties of the fluid are now taken from the NIST Webbook by a web scraper and the possibility for two-phase flow was added. Moreover, some relationships, mainly for RAC convection losses, found in the literature replaced Takken's choices.

4.5.1. ASSUMPTIONS

Given the foundational role of assumptions in shaping the zero-order model, it is crucial to explicitly state them. These assumptions as well as their reasoning are presented in table 4.1 and are inspired by Takken's [11].

Table 4.1: Zero-Order model assumptions/constraints and rationale

ID	Assumption/Constraints	Rationale
ZO-A-01	The RAC has a conical, cylindrical or concylindrical shape.	Geometries with their beam absorption studied in the previous chapter.
ZO-A-02	The RAC is made of one material.	Reduces model complexity
ZO-A-03	The RAC is in a vacuum or still air.	Forced outer convection would add complexity.
ZO-A-04	The inner wall has perfectly specular or diffuse reflection	The trained models do not consider situations in between
ZO-A-05	The ducts can only be straight or spiral	Other possibilities would add too much complexity
ZO-A-06	The RAC has a uniform temperature	High thermal conductivity allows the approximation for small dimensions.
ZO-A-07	The RAC can have upwards or sideways orientation.	Natural convection literature found for both cases.

4.5.2. OVERVIEW

The zero-order model follows the same logic as implemented by Takken [11]. The tool's inputs are the beam's output power, half-angle and origin, ambient temperature, the RAC (material, dimensions, absorptivity, emissivity, mass and geometry), the pipes (number, if spiral or linear, dimensions and length), and the propellant (initial temperature and pressure, and mass flow). Also, insulation can be added by adding its thickness and thermal conductivity. Table 4.2 clearly represents the required inputs. Consequently, the relevant outputs are the RAC's and propellant's final temperature as well as total pressure loss. Concerning the propellant properties, these are extracted from the NIST Webbook by a web scraper.

Table 4.2: Zero-order model inputs

Beam	RAC	Propellant	Surface	Ducts
Power	Diameter	Type	Absorptivity	Geometry
Half-angle	Length	Init. Temperature	Emissivity	Number
Origin	Cone Ratio	Init. Pressure	Diffuse/Specular	Length
	Aperture	Mass flow	**Insulation**	Linear/Spiral
	Mass	**Amb. Temperature**	Thickness	
	Spec. heat capacity	**Run time**	Thermal cond.	

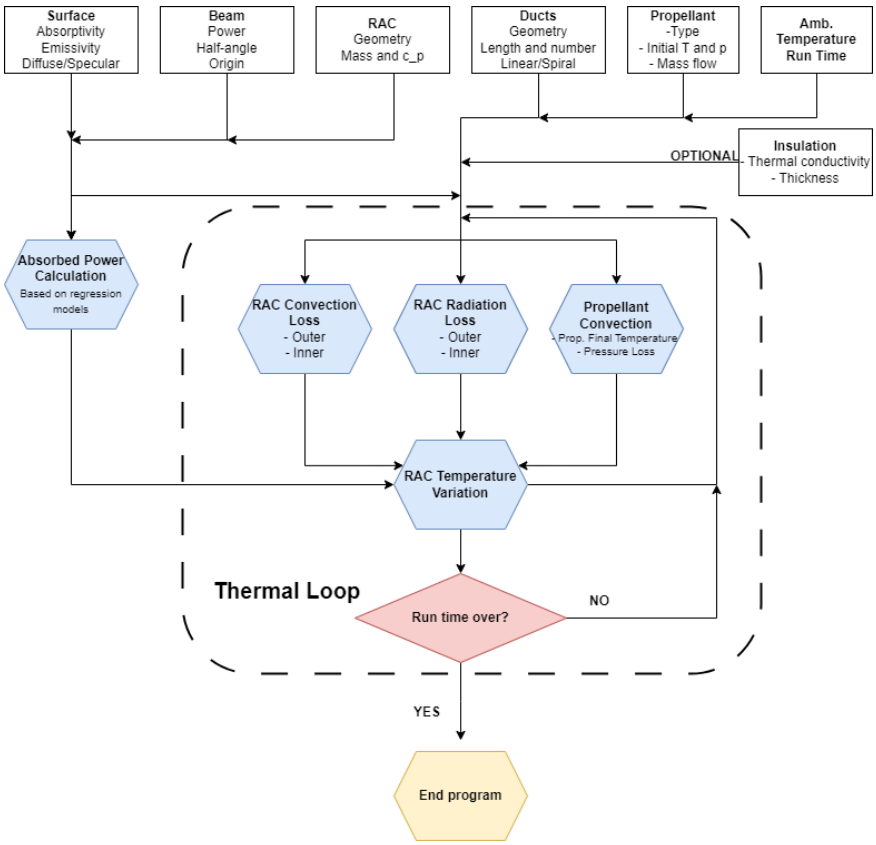

Figure 4.1: Block diagram of the transient zero-order model process

The fundamental process of the tool is quite simple and Fig. 4.1 illustrates the overall process. The absorbed beam power is estimated according to the respective regression models developed in the previous chapter. Then, considering the initial temperatures, the radiative and conductive losses are easily calculated as they follow direct formulas identified from the literature and depend only on the RAC geometry. On the other hand, the heat transfer to the propellant is more complex. A first estimate for the propellant final temperature is made assuming single-phase flow throughout the whole pipe. Afterwards, it is determined if somewhere within the duct the fluid reaches boiling temperature. If not, then the first estimate is the final result. Otherwise, the point where the boiling starts is determined by the bisection method. As soon as it is determined, the heat transferred to the fluid for the remainder of the pipe is calculated with the two-phase flow equations. Then, the heat is compared to the required energy to fully evaporate the fluid. If it is not enough, then the final temperature is the previous, otherwise, again, the point where the fluid finishes evaporating is calculated by the bisection method. The remainder of the pipe length is used in the single-phase flow equations to calculate the final temperature. Now with all the heat transfer calculated, the RAC's temperature is up-

dated taking into account the transient heat equation. With the new RAC temperature, the mentioned process repeats until the equilibrium temperature is reached.

4.5.3. VERIFICATION

Verification of the zero-order model was mainly performed by comparing expected behaviour and actual results, conservation of energy and comparison to Takken's model.

First, the radiation model was verified, i.e. no convection losses or heat transfer to the propellant, and the tool performed as expected. For example, decreasing the inner emissivity and the aperture diameter led to higher equilibrium temperatures. Also, adding external radiation losses led to a decrease in equilibrium temperatures. The beam absorption percentage part was already verified in Chapter 3.

Regarding inner and outer convection, their addition to the model led to lower equilibrium temperatures as expected since they result in energy losses. Adding insulation also resulted in higher equilibrium temperatures by diminishing outer convection and radiation losses.

With the propellant flow considered, the final propellant temperature would increase and the RAC's equilibrium temperature would decrease. This is predictable due to the energy transfer from one to the other. By decreasing the mass flow or by increasing the number of ducts, the difference between the propellant's final temperature and the RAC equilibrium temperature diminished until they became equal. This is anticipated since the heat transfer capacity from the RAC to the propellant increases, leading to equal temperatures. Also, higher RAC temperatures led to higher final propellant temperatures which is predicted.

Throughout all of these processes, it is verified that the sum of the heat transfer mechanisms equals zero when the temperatures become constant. Thus, energy is conserved.

Regarding verification with Takken's tool, both tools are run with the same inputs and their results are analysed. For all the scenarios, the equilibrium and final RAC and propellant temperature results differ by at most 5%. Table 4.3 shows an example of the inputs tested between Takken's model and the zero-order model developed. For this input, the RAC equilibrium temperature and propellant final temperature are 521.2 K and 465.2 K, respectively, for this thesis model, whereas Takken's model calculates 523.1 K and 464.8 K, respectively. This difference can be justified by the addition of web scraping for the propellant's properties and slightly different equations for the convection losses.

The two-phase flow addition to the tool could not be verified with Takken's since it had not been implemented. However, the model captures the transition phase correctly since the temperature stales at the boiling temperature for that pressure. Nevertheless, the heat flow to the propellant during this phase requires verification. This could be done by comparison to commercial CFD software. Due to this lack of verification, the cases examined further in this thesis consider gaseous flow only.

Table 4.3: Geometric and Operational Parameters for the model's comparison

Parameter	Value
Geometry	Cylinder
Vacuum	Yes
Insulation	Perfect
Propellant	N_2
D [cm]	6
A [cm]	4
L [cm]	10
α/ε	0.5/0.1
T_{amb} [K]	293.15
P_{laser} [W]	50
P_{abs} [W]	48.3
n_{pipes}	8
h_{duct} [cm]	0.2
w_{duct} [cm]	0.2
p_i [bar]	6
$\dot{m}$ [mg/s]	250

4.6. FEM MODEL

The FEM model arises from the FEM approach developed to calculate the total absorbed beam power. With spatial power distribution information, further tool development becomes feasible, incorporating heat transfer mechanisms and predicting the RAC's behaviour. It is an improvement from the zero-order model as it contains spatial information about the properties and does not average out the temperature.

This model and its development are relevant in many ways. First, the zero-order model's uniform RAC temperature assumption can be confirmed or denied. If confirmed, then the zero-order model results are more relevant since its assumption is substantiated. If not, then it cautions the user about the results of using the zero-order model. Additionally, it calculates temperatures more accurately and allows other types of studies. For example, although the equilibrium temperature is below the melting point there might be a point in the heating stage that a section is above it. Moreover, structural analysis such as stress fatigue can be performed to estimate the RAC's life cycle.

4.6.1. ASSUMPTIONS

Table 4.4 presents the assumptions in the developed FEM model. These are similar to the zero-order model but with further considerations due to the addition of spatial temperature variations. For example, only diffuse reflection is considered since the specular absorption methods do not give spatial information and now thickness is required to calculate the conduction heat transfer between nodes. Moreover, the RAC is in a vacuum and has no propellant flow. These additional developments are considered future work as they are not simple features and if the temperature gradient is not extreme, the zero-order model can be used.

Table 4.4: FEM model assumptions/constraints and rationale

ID	Assumption/Constraint	Rationale
FEM-A-01	The RAC has a conical, cylindrical or concylindrical shape.	The beam power distribution calculations were made for these geometries.
FEM-A-02	The RAC is made of one material and has constant thickness	Reduces model complexity regarding conduction
FEM-A-03	The RAC is in vacuum	Outer convection is considered future development work
FEM-A-04	The RAC has a perfectly diffuse reflection in its walls.	The specular prediction does not give spatial information.
FEM-A-05	The emissivity and absorptivity are constant through the walls.	Different values would increase complexity.
FEM-A-06	The RAC's thickness is small enough to consider that the inner and outer temperature of a node is equal	Considering would duplicate the number of nodes and the complexity of their equations.
FEM-A-07	The RAC has no fluid flow	Propellant heat transfer is considered future work.

4.6.2. OVERVIEW

Regarding the FEM model, the inputs are similar to the zero-order model, only the thickness, thermal conductivity of the material, and the number of nodes are added. No inputs regarding the ducts and propellant are needed since the model does not consider convection. Below, the development of the tool through incremental and logical steps is outlined and Fig. 4.2 illustrates the model's logic.

First, the cavity surfaces are divided into different nodes whose quantity is defined by the user input. Then, the absorbed beam power and its distribution are calculated. Next, depending on the desired simulation and conditions, each node's heat balance equation is defined. For example, in a vacuum and considering no insulation, each node's heat balance equation considers their heat flux from the beam power, their inner and outer radiation emission to surrounding surfaces and their conduction flow.

There are two options: equilibrium state and transient simulation. Each node's equilibrium temperature or temperature change is calculated considering its radiation and conduction net change.

Convection losses and propellant flow have not been added and are considered future work. A possible way to perform this has already been suggested regarding the implementation of convection losses. Regarding propellant flow, it will be necessary to add spatial information about the ducts so that the governing equations can be adjusted where needed. Again, in case the developed FEM model shows that the temperature distribution is sufficiently uniform (this definition will depend on the user's criteria), the user can predict these by using the zero-order model.

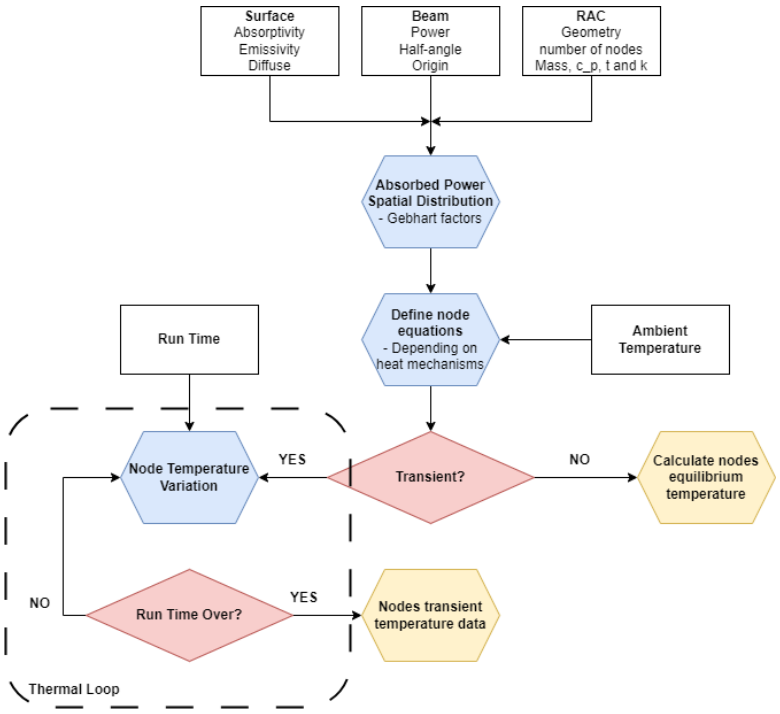

Figure 4.2: Block diagram of the FEM model process

4.6.3. VERIFICATION

The verification process of the FEM model was mainly done by comparison between expected behaviour and the tool's results and numerically by the conservation of energy. In addition, a comparison to the zero-order model is performed.

The beam power absorption percentage of the model has already been verified in section 3.8 of the previous chapter. Concerning its distribution, it was verified due to a comparison between expectations and results, and COMSOL distribution results. For example, as the absorptivity lowers, the power distribution which focuses on the incident areas at high absorptivity values starts to spread out to the other surfaces. Moreover, the distribution is coupled with the absorbed percentage and, consequently, the verification of the latter supports the verification of the former.

Regarding the node's heat flow equations, they were developed in incremental steps to identify and rectify errors in a consistent and orderly manner. Consequently, verification for each advancement in the model was also possible by analysing the results to the expectations and calculating if the heat balance equation with the equilibrium temperature stayed null:

$$\Delta Q_{RAC} = 0. \tag{4.12}$$

The first development of the model was calculating the equilibrium temperature of each node considering only inner radiation loss. Thus, no conduction, no convection,

no outer radiation loss, and no propellant flow. Regarding conservation of energy, the general heat balance equation, in this case, is:

$$\eta_{abs} P - \sigma \varepsilon \sum_{i=1}^{n} B_{i0} A_i \left(T_i^4 - T_{amb}^4\right) = 0, \tag{4.13}$$

where n is the total number of nodes and 0 is the aperture's surface number. To verify this result, it is expected that the temperature of the nodes that get hit by the laser is higher than the rest. Also, this difference should increase with the increase in absorptivity and decrease in emissivity. Both these predictions were verified consistently. The conservation of energy property was extensively tested with all the geometries, different inputs and number of nodes, thus, verifying the equations for this scenario. For instance, the usual result is below 10^-6 W for a laser power of 20 W, which is undeniably infinitesimal.

The next step was to add conduction through the nodes. As explained in section 4.3, only the conduction between inner wall nodes is considered, since considering conduction to the outer wall would require twice the nodes (FEM-A-06). The nodes' equations were rewritten considering the conduction equations in section 4.3.

Regarding verification, null thermal conductivity should give the same result as the previous situation and as thermal conductivity increases, the temperature across the RAC becomes more uniform. The two cases were confirmed by different inputs and by analysing the effect of changing the thermal conductivity. Regarding numerical verification, due to the reciprocity of conduction, the heat balance equation remains the same as the previous case (4.13). By analysing its result, the errors in the equations were identified and corrected. In the end, the result of the equation was of similar order as the only inner radiation case.

In case the RAC is not externally insulated, there is a significant outer radiation loss. The incorporation of this is easily done by adding the outer radiation loss in each done. The general heat balance equation used to verify the result trivially becomes:

$$\eta_{abs} P - \sigma \varepsilon \sum_{i=1}^{n} \left(B_{i0} A_i \left(T_i^4 - T_{amb}^4\right) + A_i \left(T_i^4 - T_{amb}^4\right)\right) = 0. \tag{4.14}$$

Thus, this situation is numerically verifiable. In addition, with the element, the nodes' temperature reduces as expected with the higher temperature nodes decreasing more.

The results between the zero-order and the FEM model were constantly compared during the verification process. Differences between the equilibrium temperatures are expected due to the additional spatial component of the FEM model but at high thermal conductivity values, these differences ought to be small. It is relevant to understand that the equilibrium temperatures when referring to the FEM model results are the area-weighted averaged nodes temperature.

Table 4.5 shows the differences in equilibrium temperature for the case study in Chapter 5. As can be seen, there are differences in the equilibrium temperatures but they undeniably are within the same range.

The absorbed power is slightly different since the zero-order model uses the regression models while the FEM model uses the developed algorithm with view factors. Nevertheless, if the absorbed power is brute forced to be the same in the zero-order model the differences are still of the same order. The explanation comes from the assumed

Table 4.5: Difference between zero-order and FEM model - Case Study results

	Zero-order				FEM			
CR	L [cm]	D [cm]	P_{abs} [W]	T_{eq} [K]	L [cm]	D [cm]	P_{abs} [W]	T_{eq} [K]
0	5	4	11.13	898.4	5	4	11.24	907.0
0.5	5	4	8.86	915.1	5	4	8.92	918.3
1	5	4	6.77	935.3	5	4	6.80	941.8

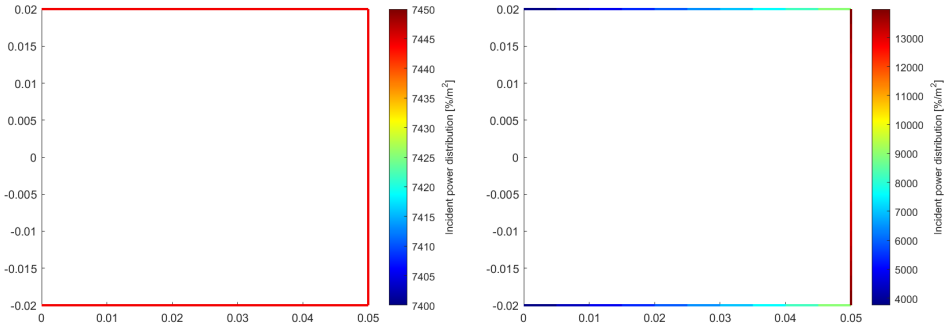

(a) Zero-order model distribution

(b) FEM model distribution

Figure 4.3: Absorbed power distribution [%/m^2] for the cylindrical case of table 4.5 in both models.

incident absorbed power distribution which can be seen in Fig. 4.3. Zero-order model assumes an equal distribution of around 7450 %/m^2 while the FEM model varies drastically from 4000 to 13000 %/m^2. This results in different equations for each node and, thus, slightly different results which are approximated due to the high thermal conductivity. Since higher incident power is attributed to the furthest nodes from the aperture, more of its energy is perceived within the cavity, thus, explaining the higher temperatures.

If the number of nodes in each surface is set to one and then the absorbed power in the zero-order model is hard set to equal the FEM model, then the results differ by less than 0.1%. This is expected due to the averaging out of the power distribution.

To conclude, the FEM model was successfully verified by comparing its results with the expected behaviour, satisfying conservation of energy and similar results to the zero-order model when high thermal conductivity is present.

4.7. CONCLUSION AND RECOMMENDATIONS

In this chapter, we have provided a comprehensive overview of the relevant heat transfer mechanisms— radiation, convection, and conduction — and their application to the receiver-absorber cavity (RAC). The foundational principles behind these mechanisms were discussed in detail, elucidating how they govern the thermal behaviour within the RAC.

Two predictive models were developed and verified: the zero-order model, inspired

by Takken's work, and a more sophisticated Finite Element Method (FEM) model, resultant of Chapter 3 work. The zero-order model, being a simplified approach, provided a fundamental understanding of the heat transfer processes, while the FEM model incorporated spatial components for more detailed predictions. Both models were scrutinized for their assumptions and operational frameworks, with successful verification demonstrated through their alignment with expected behaviour, numerical energy conservation, and comparative analysis against established models (the zero-order model with Takken's model and the FEM model with the zero-order model under conditions of high thermal conductivity).

The further development of the FEM model stands out as a critical area for future work. To enhance its accuracy and applicability, several key improvements are recommended:

- **Incorporation of Convection Losses:**
  - Currently, the FEM model accounts only for radiation and conduction mechanisms. Introducing convection losses into the model will provide a more accurate model when not in a vacuum.
- **Integration of Propellant Heat Transfer:**
  - Extending the FEM model to include heat transfer to the propellant will allow for predicting the RAC's performance, reflecting the true operational conditions and improving the model's predictive capabilities.
- **Addition of Insulation:**
  - Insulating the RAC can be modelled by incorporating an extra layer of nodes. This modification will enable the evaluation of insulation effects on thermal performance, guiding design improvements for better energy efficiency.
- **Commercial software verification**
  - The FEM model verification would be enriched if its results were compared to commercial FEM software results for the same scenario. In this scenario, the node governing equations could be verified by adding equal beam heat fluxes to each node.
- **Development of a User-Friendly Interface:**
  - To facilitate the practical application of the developed tool by future students and researchers, creating a user-friendly interface is essential. This interface should simplify model setup, execution, and analysis, making the tool accessible to users with varying levels of expertise.

By implementing these recommendations, the FEM model can evolve into a more robust and versatile predictive tool, significantly contributing to the field of thermal analysis and design optimization for RAC systems.

5

RAC Design Optimization

Efficiency is a central concern in engineering, even though the ideal of reaching 100% remains beyond reach. Nonetheless, engineers continuously strive to maximize efficiency, minimising waste and enhancing performance wherever possible. This process typically involves leveraging previously developed tools to estimate the performance of potential designs.

With the prediction tools developed in the previous chapter, RAC design optimization becomes the next logical step and is the topic of this chapter. First, the overall RAC efficiency is defined and dissected into two parts. The chapter's case study is then presented. A conical, cylindrical and concylindrical with a 0.5 cone ratio are the optimization designs and their lengths and diameters are the optimization variables. Next, the optimization tools for the two different efficiencies are presented alongside the study case's result. Moreover, interesting findings concerning optimization trends are revealed. The code developed is available on the author's GitHub [1].

It is relevant to note that in this chapter the optimization is only related to efficiency, but usually other criteria such as size and mass can play a part in the optimization. For example, one design might be preferred to another despite being slightly less efficient due to its favourable lower mass.

5.1. RAC Efficiency

Efficiency is usually related to its mechanical definition: the ratio between the device's power output and its power input. Consequently, in this propulsion system, the RAC's efficiency can be related to how much of the incoming energy i.e. the beam power is transferred to the propellant [10]:

$$\eta = \frac{\dot{m}\Delta H}{P_{beam}}, \tag{5.1}$$

[1] Thesis Github

where $\dot{m}$ is the propellant mass flow, ΔH is the enthalpy change and P_{beam} is the incoming beam power.

This overall efficiency can be divided into two crucial and somewhat independent efficiencies: absorption efficiency by the cavity and heat transfer efficiency to the fluid.

The absorption efficiency is related to the ability to absorb and retain the beam incident power. Consequently, it depends on the surface's emissivity, absorptivity and cavity geometry. However, no ordinary efficiency formula can translate the RAC's absorption efficiency. It depends on the thermal processes involved. Consider, for example, a RAC perfectly insulated and in space (no outer or inner convection and null ambient temperature), therefore, the only energy loss is via inner radiation. The equilibrium temperature T_{eq} can be calculated:

$$\eta_{abs} P = \sigma \varepsilon A B_0 T_{eq}^4 \Leftrightarrow T_{eq} = \sqrt[4]{\frac{P}{\sigma}} \sqrt[4]{\frac{\eta_{abs}}{\varepsilon A B_0}}, \tag{5.2}$$

where P is the laser power, η_{abs} the percentage of power that is absorbed by the cavity, σ the Stefan-Boltzmann constant, ε the surface's emissivity, A the inner area, B_0 the inner surface's exit Gebhart factor. Consequently, the absorption efficiency is related to:

$$\sqrt[4]{\frac{\eta_{abs}}{\varepsilon A B_0}}. \tag{5.3}$$

The higher this factor the higher the absorption efficiency. Thus, the absorption efficiency is related to maximizing the equilibrium temperature when no propellant is flowing. This is expected since, for equal beam power, the higher the temperature in this situation, the higher the propellant's enthalpy change will be.

Unlike usual efficiency formulas, this factor has $1/m^{\frac{1}{2}}$ units and is not capped at 1. Thus, the absorption efficiency, in this case, is related to the laser half-angle, RAC geometry and surface properties (absorptivity and emissivity). As more thermal transfer processes are involved, the more complex this factor becomes, making it challenging to discern the influence of each variable and, therefore, less straightforward.

The second efficiency is dependent on, for example, the propellant, its mass flow, duct geometry and layout. Lienhard J. et al [36] state that this second efficiency, namely heat exchanger efficiency, can be determined from:

$$\eta_{hx} = 1 - exp\left(\frac{-hPL}{\dot{m}c_p}\right) = 1 - exp\left(\frac{-\mathrm{Nu}kP^2L}{4A\dot{m}c_p}\right), \tag{5.4}$$

where h is the convective heat transfer coefficient, L is the duct's length, P and A are the cross-sectional perimeter and area of the duct, respectively, Nu is the Nusselt number (whose formulas are taken from the literature and can be seen in the Appendix E), k and c_p, respectively, are the thermal conductivity and the specific heat capacity of the propellant [36]. Unlike the previous efficiency, this one has a typical formula.

Although these efficiencies are not related directly in terms of processes, making changes in one another may impact the other. For example, in a scenario where decreasing the RAC's diameter increases the absorption efficiency, it reduces the length of the spiral ducts, reducing the heat exchanger efficiency. Consequently, there are characteristics related to both and their alteration affects both.

5.2. CASE STUDY - INPUTS AND CONSTRAINTS

To show the optimization results, a case study to which the optimization process is applied is presented. This case study is related to the experimental part of this thesis and, thus, some of the RAC's manufacturing requirements and constraints are applied. Consequently, the differences between the manufactured and optimal models can be demonstrated.

The beam is a focused solar ray and, thus, its absorptivity is taken in the solar spectrum region. It has a diverging half angle of 5º and its output power is set to 20 W. The origin is set to where the beam's outer region is tangent to the RAC's aperture (similar to the Chapter 3 case).

Figure 5.1: Geometries of interest to the case study in 2D axial view (not to scale) - CR = 0, 0.5, 1.

Concerning the RAC, it is made of aluminium (thermal conductivity of 237 W/mK), must fit inside a standard 1U (10x10x10 cm), its aperture is 4 cm, its length must be at least 5 cm and has a thickness of 4 mm. The cone ratios optimized are 0, 0.5 and 1 (Fig. 5.1). The cavity has no surface coating and thus has the surface characteristics of aluminium ($\alpha/\varepsilon = 0.15/0.05$ [22]). The RAC has eight inner ducts. Their width and height values can range from 0.5 to 5 mm and 1 to 3 mm, respectively. Due to the manufacturing process, the surface reflection is considered fully diffused and only linear rectangular ducts are considered. The melting point of the material is ignored since what is relevant is to show the optimization process and its trend related to each variable.

Regarding the propellant used, it is gaseous nitrogen. The initial pressure ranges from 3 to 6 bar and the mass flows considered are the theoretical critical mass flows for those pressure values with a 0.5 mm diameter throat nozzle - from 122.5 to 251 mg/s.

The optimization process is performed considering a vacuum, perfect outer insulation and a 50 K ambient temperature. Although vacuum and a low ambient temperature are not the experimental conditions, they could be the scenario in space conditions. The surrounding temperature was arbitrarily set for the example: way lower than ambient temperatures on Earth but higher than space temperature since the system would be inside a spacecraft. Nevertheless, the effect of convection is studied and the ambient temperature does not affect the optimization trends (leading to equal results).

Table 5.1 summarizes the optimization case inputs and parameter ranges. The nomenclature follows the used standard in the thesis. Considering this setup, the length and diameter of the RAC are the variables optimized in the absorption efficiency optimization phase. Regarding the heat exchanger efficiency, the width and height of the ducts are optimized for higher heat transfer.

Table 5.1: Input Parameters for the Optimization Case Study

Parameter	Value	Parameter	Value
P_{in} **[W]**	20	θ **[º]**	5
o **[cm]**	$\frac{A}{2\tan\theta}$	L **[cm]**	[5,10]
D **[cm]**	[4,10]	A **[cm]**	4
CR	[0, 0.5, 1]	t **[mm]**	4
k **[W/mK]**	237	α/ε	0.15/0.05
n_{ducts}	8	L_{ducts} **[cm]**	L
T_{amb} **[K]**	50/293.15	p_i **[bar]**	[3,6]
$\dot{m}$ **[mg/s]**	40.83 p_i	$T_{p,1}$ [K]	293.15
h_{ducts} [mm]	[1,3]	w_{ducts} [mm]	[0.5,5]

5.3. ABSORPTION EFFICIENCY OPTIMIZATION

As previously investigated, the main factors which influence the absorption efficiency are the cavity geometry and its surface properties. The goal is to optimize to the highest RAC temperature within the boundaries of each parameter which are defined by the requirements. In this case study, the optimization parameters are the RAC length and diameter and their requirements are in Section 5.2. First, the optimization method and its verification process are briefly explained. Then, lastly, the effects of the surface coating, conduction and convection are explored.

5.3.1. OPTIMIZATION METHOD

Since two RAC tools were created, the absorption efficiency optimization was developed for both. However, the FEM model does not have the convection losses incorporated. Thus, only vacuum optimization is considered. For simplicity of the following examples, when insulation is considered, the RAC is perfectly insulated outside.

The variables to be optimized in intervals are:

- Beam half-angle,
- RAC Length,
- RAC Diameter,
- RAC Aperture.

The other characteristics such as geometry, surface reflection, emissivity and absorptivity, are initial inputs which can also be changed. Initially, emissivity and absorptivity were part of the optimized variables but higher absorptivity and lower emissivity are always desired and, therefore, it does not make sense to optimize for intervals. Rather the optimization should be done in input pairs considering the properties of the available coatings.

After defining the equilibrium temperature as a result of the heat balance equation, the variables can be optimized to maximize it with the MATLAB Optimization Toolbox. This toolbox allows the use of methods such as Sequential Quadratic Programming

(SQP), Genetic Algorithms (GA), and others. The SQP was used due to its speed and ability to set constraints inside the optimization tool. The extensive study of different optimization methods and their performance in this case is out of the scope of this thesis.

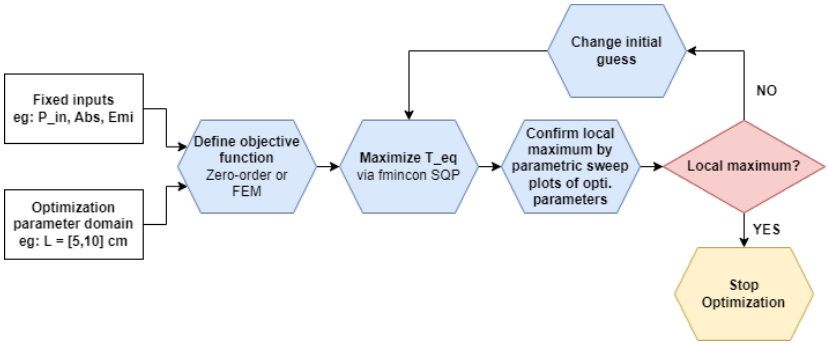

Figure 5.2: Overview of the absorption efficiency optimization process

Fig. 5.2 illustrates the absorption efficiency optimization process via a flow chart. To illustrate the result of the optimization process, the previously mentioned case study is optimized for three different cone ratios.

Table 5.2: Case study optimization results for both models

	Zero-order				FEM			
CR	L [cm]	D [cm]	P_{abs} [W]	T_{eq} [K]	L [cm]	D [cm]	P_{abs} [W]	T_{eq} [K]
0	5	4	11.13	898.4	5	4	11.24	907.0
0.5	5	4	8.86	915.1	5	4	8.92	918.3
1	5	4	6.77	935.3	5	4	6.80	941.8

In table 5.2, the optimization results for the example provided are shown. For all geometries, the length and diameter optimal values are the lowest boundary. This means that for these emissivity and absorptivity values, it is more advantageous to decrease the area. Regarding the equilibrium temperature, the cone reaches the highest value although it absorbs only 6.7 W compared to 10.24 W of the cylindrical case, emphasizing the importance of reducing the emission loss. Despite the equal optimization, the T_{eq} values are slightly higher for the FEM model compared to the zero-order, however, it is not significant in terms of percentage and a divergence is already expected due to the model's differences.

The computational demand of the optimization process for this specific optimization domain is small. The zero-order optimization runs for each geometry take less than 10 seconds whereas the FEM model optimization with 10 nodes in each surface takes around 10 seconds. Since the optimization is performing the equilibrium temperature calculation, its speed will depend directly on that process's speed. Consequently, for the FEM model the optimization process time increases by increasing the number of nodes. For higher optimization domains, the optimization process is expected to take longer

but, since the equilibrium temperature calculation tends to be fast, it should not entail huge operational periods.

The difference in T_{eq} between geometries is relatively low since the differences in absorbed power get neutralized by the differences in inner radiation loss. By increasing the absorptivity while maintaining the emissivity, the radiation loss relation remains the same. At the same time, the absorbed power relative differences diminish, leading to a higher T_{eq} difference between geometries. For example, by increasing the absorptivity to 0.9, the power absorbed differs from 19.6 W in the cylindrical case to 19.1 W in the conical. Consequently, the cylindrical cavity reaches 1000 K while the conical reaches 1220 K.

The optimization process does not entail a straightforward verification process. In fact, the optimization method itself does not guarantee that it finds the global maximum. Nevertheless, to identify that the optimization code is running as it should two approaches are performed.

The first approach entails comparing what is expected to the result. For example, when the emissivity and absorptivity were incorporated into the optimization variables, their optimal value was their lower and upper boundary, respectively. This equals maximizing the absorption and minimizing the radiation losses which is expected. Another aspect that works similarly is the aperture, whose optimal value is its lowest boundary for the same reason.

The second method is to plot in a grid two of the optimization intervals and their equilibrium temperature (with the other variables with their optimal value). Fig. 5.3 shows the plots for the cone optimization results from the previous example. In addition, it shows the effect of changing the incident angle. From it, it is clear how the smaller dimensions and beam angle lead to the maximum temperature. Previous analysis shows that increasing the angle tends to decrease absorption on diffuse surfaces, corroborating the result. That way the shape of the graph is visualized and the optimal values can be confirmed. By performing this on all possible variable pairs, the local optimal solution is verifiable. If the plots show another optimal point, the initial guess can be adjusted and the optimization runs once again, until the optimal points match.

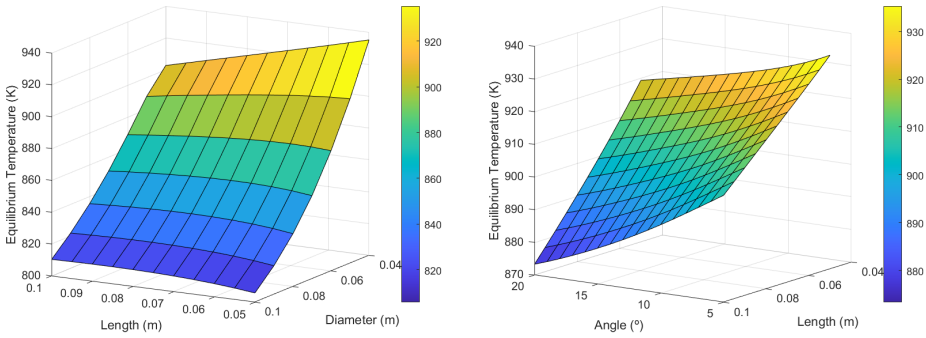

(a) Length and diameter influence on T_{eq}

(b) Length and beam half-angle influence on T_{eq}

Figure 5.3: Example of optimization verification plots

An additional noteworthy comment refers to the effect of increasing the length in Fig. 5.3a plot. The optimal length dimension for absorption efficiency is the lower boundary at 5 cm. Doubling the length would lower the temperature from 940 K to 910 K. However, the linear duct's length would also double, increasing the heat exchanger efficiency and perhaps leading to a higher overall efficiency. Consequently, the importance of considering both efficiencies is emphasized.

5.3.2. SURFACE COATING EFFECT

To the surface, a coating can be applied, changing its emissivity and absorptivity. These two factors influence the radiation loss and the absorption of the laser. It is trivial that higher absorptivity and low emissivity values are desired to increase the equilibrium temperature. Nevertheless, their effect on optimization trends is studied. For that, the previous optimization scenario is considered with four different emissivity and absorptivity ratios. The ratio between absorptivity and emissivity is hereby defined as the coating ratio.

Table 5.3: Optimal geometrical values for each example coating (CR = 0)

Coating	**1**	**2**	**3**	**4**
α/ε	0.15/0.05	0.15/0.15	0.15/0.4	0.15/0.9
L [cm]	5	10	10	10
D [cm]	4	4	4.35	10
T_{eq}	907	779	720	703

Table 5.3 shows the optimization results for the four different coatings. The optimization considered the FEM model with conduction and the results are only for the cylindrical case. As anticipated, the equilibrium temperature diminishes due to the increase in the radiation loss factor. On the other hand, the optimal length and diameter depend on the coating's properties and a trend is seen. When the ratio is high, the optimization tends towards the lower boundary of both variables. As it goes down, the optimal values begin to approach the higher boundary: first the length and then the diameter until both are at their maximum possible values. This trend has been consistently captured in several studied scenarios and appears, not only in the cylinder but in all the geometries. Fig. 5.4 plots clearly illustrate and verify the trend. This is a result of the flattening of the absorption efficiency term related to the inner radiation loss $\left(\sqrt[4]{\frac{1}{\varepsilon A B_0}}\right)$ throughout the optimization domain. This term's maximum is at the lowest dimensions, however, the difference between the minimum and the maximum in coating 1 and 4 is, respectively, 1.7 and 0.03 $m^{-\frac{1}{2}}$. Consequently, the absorption efficiency term related to the beam power absorption effect increases with the decrease in surface coating ratio, leading to an optimal design which maximizes it.

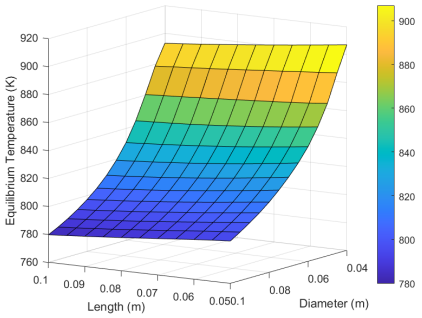

(a) Coating 1

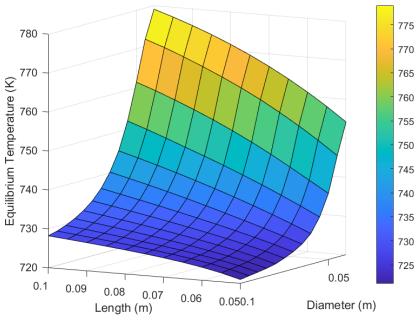

(b) Coating 2

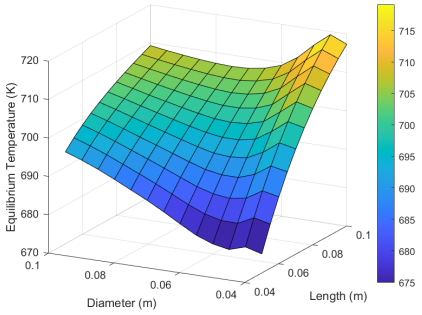

(c) Coating 3

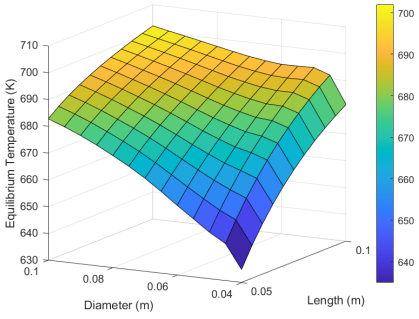

(d) Coating 4

Figure 5.4: T_{eq} optimal geometry verification plots for each coating

To sum up, absorptivity and emissivity play a part in the optimal geometric properties of the cavity, mainly its length and diameter. A trend related to the coating ratio has been found for all geometries. Nevertheless, optimizing the dimensions for the specific requirement is still relevant as the trend is merely qualitative and its transaction phases depend on factors such as thermal conductivity as shown in the next subsection.

5.3.3. CONDUCTION EFFECT

To study the effect that conduction has in the FEM model, the study case is optimized with the FEM model considering a null thermal conductivity i.e. no conduction heat exchange. The scenario in table 5.3 with the aluminium thermal conductivity is similar to the infinite conductivity case and, thus, not represented here.

Table 5.4: Optimal geometrical values for each example coating and no conduction

Coating	**1**	**2**	**3**	**4**
α/ε	0.15/0.05	0.15/0.15	0.15/0.4	0.15/0.9
L [cm]	5	10	10	10
D [cm]	4	4	4	4
T_{eq}	900	797	757	742

The optimization process results without conduction are shown in table 5.4. Concerning the equilibrium temperature, its value is lower for the first coating but higher for the others when compared to table 5.3. Although it also shows a downtrend with the coating ratio increase, without conduction it is slightly slower. The optimal length and diameter are for the first case the lower boundary values and for the others the length reaches its maximum value while the diameter stays at its minimum. Compared to the conduction case, this is the first stage of the defined trend (Figs. 5.4a and 5.4b). However, by increasing the ratio even further, the spotted trend is the same. Thus, for the no-conduction case, the transaction between the plots in Fig. 5.4 requires a larger coating ratio. Additionally, when low thermal conductivity values are used, it was found that the transition in trend phases is more sensitive to the coating ratio with higher thermal conductivity. Consequently, length and diameter at their maximum values would be optimal.

In conclusion, the conduction heat exchange in the FEM model significantly impacts the optimization process. While the trend observed without conduction follows a similar pattern to the case with conduction, the transition between phases necessitates a larger coating ratio. Additionally, the sensitivity of trend phases to changes in the coating ratio is proportional to the thermal conductivity.

5.3.4. CONVECTION EFFECT

In space, inner convection losses are not a concern. However, if testing is done outside a vacuum chamber, it is necessary to account for it in a prediction tool. Thus, the convection effect on optimization in the case study is analysed. As stated, the inner convection loss has been implemented only in the zero-order model. Also, the surrounding temperature has been changed to 20ºC since the air data properties available have only values upwards of 0ºC.

The addition of inner convection loss results in a lower equilibrium temperature as expected. When comparing the no convection to the convection case with different coating ratios, it is clear that the presence of convection loss leads to an advance in the optimal value shift of length and diameter from the lower to the higher boundary. This means that for the optimal values to be their maximum, the coating ratio does not need to be as low. For example, the inputs of Fig. 5.4a with inner convection lead to the Fig. 5.4d plot.

5.4. HEAT EXCHANGER EFFICIENCY OPTIMIZATION

As mentioned, the heat exchanger efficiency is related to the capacity of transferring the RAC's thermal energy to the propellant and is given by equation (5.4). The formula de-

pends on the mass flow, the ducts' geometrical characteristics, the propellant's properties and the convective heat transfer coefficient. Considering the propellant convection formulas, the efficiency calculation is possible and so is its optimization.

5.4.1. OPTIMIZATION METHOD

In this case, since the efficiency does not depend on the spatial temperature distribution, there is no distinction between the RAC tools and the optimization process is equal for both. For simplicity, only the single-phase propellant case is considered for this tool, the duct is linear and can be either rectangular or circular shaped. The optimization process overview is similar to the absorption efficiency (Fig. 5.2) just changing the inputs and objective function.

The variables that can be optimized are the duct shape and the propellant's mass flow. The other parameters are initial inputs whose optimization is trivial or not applicable. For example, the pipe's length optimal value will always be the upper boundary as it maximizes efficiency and is unrelated to any other property. The specific heat capacity and the thermal conductivity of the propellant are properties that are not subject to optimization. Although a low mass flow appears to be optimal, it influences Nu so the lower boundary might not be desirable. Thus the duct shape appears to be the most influential optimization variable since it influences P, A and also Nu.

The properties of the propellant depend on the considered temperature which is also an input of the optimization process. The bulk temperature is not known at this stage since it is the mean of the inlet and outlet temperature and the latter is not initially known. Consequently, the user ought to make either an educated guess of the bulk temperature or perform optimizations for several possible values and determine if the optimization results differ. Since the inlet temperature and the maximum RAC temperature without propellant are known an interval for the possible values is trivially determined.

For the case study, eight 10 cm linear and rectangular-shaped ducts are considered with an inlet propellant temperature of 293.15 K. The minimum and maximum height are 1 and 3 mm, and the minimum and maximum width are 0.5 mm and 5 mm. The mass flows considered are the theoretical critical mass flows for the experiments (from 122.5 to 251 mg/s). Thus, only the duct shape is optimized in the case study.

Table 5.5: Case study's heat exchanger efficiency at different bulk temperatures with $\dot{m} = 251$ mg/s

T_b [K]	300	500	700	900
η_{hx}	0.922	0.975	0.989	0.994

The optimization results are 3 mm in height with a 0.5 mm width for all mass flow cases and possible bulk temperatures. The efficiency values range from 0.92 to 1, decreasing with the increase in mass flow and increasing with the bulk temperature estimate. Table 5.5 shows the bulk temperature effect on efficiency for the highest mass flow case.

The decrease in efficiency with the increase in mass flow follows trivially from the efficiency equation and appears to not have a significant effect on Nu to increase it. The increase with the increase in bulk temperature is a result of the increase in the nitrogen's thermal conductivity and specific heat capacity ratio which doubles from 300 to 900 K.

Table 5.6: Case Study heat exchanger efficiency - Nu and P^2/L variation at $\dot{m} = 251$ mg/s and $T_b = 700$ K.

h [mm]	w [mm]	Nu	P^2/A	η_{hx}
1	0.5	3.73	18.0	0.925
3	0.5	3.78	32.7	0.989
1	5	3.81	28.8	0.98
3	5	3.95	17.1	0.92

The optimized value is the result of maximizing the perimeter and area ratio of the ducts. In all scenarios, the flow is laminar and the Nusselt number does not change enough to affect the optimal values as can be seen in table 5.6. This can be seen for all the mass flow values in the case study. However, this is not always valid since there are regions where Nu changes more drastically.

5.4.2. NUMBER OF DUCTS EFFECT

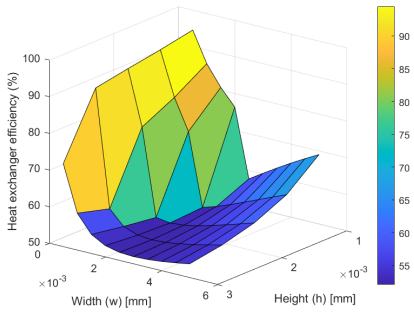

(a) $n_{pipes} = 2$

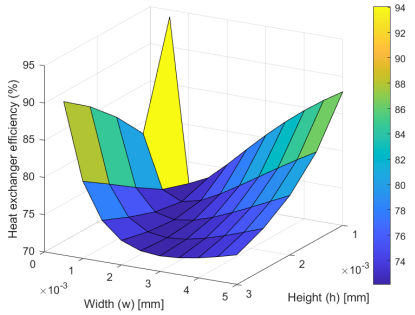

(b) $n_{pipes} = 4$

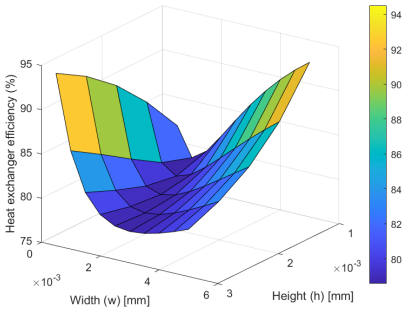

(c) $n_{pipes} = 5$

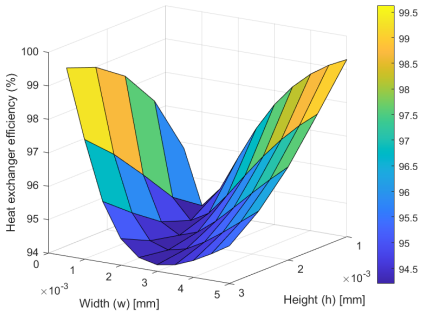

(d) $n_{pipes} = 10$

Figure 5.5: n_{pipes} effect on η_{hx} and optimal duct shape at $\dot{m} = 251$ mg/s and $T_b = 700$ K.

The number of ducts affects the amount of mass flow in each duct. Thus, studying the number of ducts is also studying the mass flow effect in the heat exchanger efficiency. As previously seen, the mass flow influences both the numerator (directly) and the denominator (indirectly) of the efficiency term. To study its effect, the number of ducts in the case study is changed.

In Fig. 5.5, the heat exchanger efficiency results for different height and width dimensions and the number of pipes are presented for the case study. At low pipe numbers, the optimal result tends to be the lowest dimension possible due to the propellant flow being turbulent. The possible efficiency values can be drastically different ranging from 95% to almost 50%. As the number of pipes increases, the difference between the possible heat exchanger efficiencies diminishes and the optimal efficiency increases as well. With the increase in the number of pipes, the flow becomes laminar and in that scenario, the optimal solution is the one which maximizes the perimeter-area ratio.

Table 5.7: Case Study heat exchanger efficiency - Nu and P^2/L variation at $n_{pipes} = 2$, $\dot{m} = 251$ mg/s and $T_b = 700$ K.

h [mm]	w [mm]	Nu	P^2/A	η_{hx}
1	0.5	17.85	18.0	0.945
3	0.5	4.3	32.7	0.727
1	5	4.45	28.8	0.69
3	5	4.9	17.1	0.54

Table 5.7 shows the Nusselt number variation for the case study considering only 2 ducts at $\dot{m} = 251$ mg/s and $T_b = 700$ K. The P^2/A ratio only doubles from the first case while Nu reduces to approximately a fourth of its value. Consequently, the optimal solution tends to be the turbulent case due to the significant relative increase in Nu compared to P^2/A.

To sum up, the number of ducts defines the propellant flow regime which defines the optimal solution: turbulent has higher efficiency at the lowest values possible and laminar has higher efficiency at higher perimeter-area ratios. Also, a higher number of ducts leads to higher heat exchanger efficiency, as predictable, and reduces the efficiency differences within the possible dimensions.

5.5. OVERALL EFFICIENCY OPTIMIZATION

In the previous sections, the optimization of the absorption and heat exchanger efficiency were addressed. However, as mentioned, despite dealing with different aspects, their results depend on common characteristics and, thus, the optimal scenario for one might not be optimal for the other. Consequently, overall optimization is required.

The optimization process follows trivially from the previous examples. The user defines the optimization ranges for the desired variables and sets the others. The parameters to be optimized are the RAC's geometry (diameter, length and aperture diameter) and the duct shape. However, unlike the previous cases, the optimization is performed by parametric sweeps and not an optimization algorithm.

Considering the case study, since the ducts are linear, the RAC's diameter does not

influence the heat exchanger efficiency and it has a consistent negative influence on the absorption efficiency. Consequently, one might conclude the optimization process for the overall efficiency addresses only the RAC's length: higher length leads to higher heat exchange efficiency but lower absorption efficiency. However, this is not true as will be demonstrated.

The dimensions of the ducts will have the same optimal value since it is not related to the absorption efficiency.

Table 5.8: Overall efficiency for different lengths and cone ratios at $\dot{m}$ = 251 mg/s and D = 4 cm

CR	L [cm]	5	6	7	8	9	10
0	P_{abs} [W]	11.1	12.1	12.9	13.6	14.1	14.6
	$T_{eq,\,RAC}$ [K]	352.22	352.0	352.1	352.3	352.5	352.8
	$T_{p,f}$ [K]	335.1	338.8	341.8	344.3	346.3	347.9
	η_{RAC} [%]	55	60	64	67	70	72
	Q_{prop} [W]	11.0	12.0	12.8	13.5	14.0	14.5
1	P_{abs} [W]	6.8	7.6	8.3	8.9	9.5	10.0
	$T_{eq,\,RAC}$ [K]	329.7	330.5	331.4554	332.5	333.6	334.6
	$T_{p,f}$ [K]	318.8	321.8	324.5	326.9	329.1	331.0
	η_{RAC} [%]	34	38	41	44	47	50
	Q_{prop} [W]	6.7	7.47	8.2	8.82	9.4	9.9

The optimization with a 4 cm fixed RAC diameter resulted in an optimal length value equal to its upper boundary for all mass flow cases. The results for the case study optimization for the highest mass flow rate for cylindrical and conical geometries are shown in table 5.8. The 0.5 cone ratio scenario results are not displayed since they follow the same trends, having a performance in between the other two geometries.

First general trend remarks for both geometries are identified. As the length increases, so does the absorbed laser power. The RAC temperature stays fairly in the same range with the length having a slightly positive effect due to the higher absorbed power. The propellant final temperature approaches the RAC equilibrium temperature with the increasing length, which is expected due to the increase in heat exchanger efficiency. Regarding the overall efficiency, it goes up significantly in both geometries.

Concerning the comparison of the results between geometries, the cylinder has higher absorbed power, as expected. On the other hand, the cylindrical cavity obtains higher RAC temperatures as well as higher final propellant temperatures. Consequently, the cylindrical has higher efficiency values. However, this was not expected as the conical geometry presented itself as the geometry with the highest absorption efficiency. The key component in this change is the amount of absorbed power that gets transferred into the propellant.

When comparing the absorbed power P_{in} and the power transferred to the propellant Q_{prop} these are practically equal, meaning that the inner radiation loss is almost negligible. Thus, the higher the absorbed power, the more power there is to transfer to the propellant and the higher the efficiency. This is not considered when analysing the absorption efficiency as it was defined. Consequently, the absorption efficiency might not be a metric as useful as initially defined to guide a design. Nevertheless, it might be

more useful in scenarios where the heat efficiency is lower or the RAC's area is bigger and, thus, radiation losses play a more significant part.

By identifying that the absorbed power is the primary driver in the case study, the diameter becomes an optimization variable alongside the length. Higher diameter leads to higher power absorption so it is expected that the optimal diameter is no longer the minimum of the range but its maximum value.

A parametric sweep of the length and diameter domain was performed for both geometries and the previous findings for the 4 cm diameter remained the same: higher length and same diameter led to higher efficiency. Moreover, higher diameter led to higher efficiency as well due to the increase in absorbed power and the inner radiation loss still being lower than 2% of the absorbed power. Consequently, the optimal RAC dimensions for this case study are the maximum values for length and diameter, respectively, 10 and 10 cm. Regarding the conical geometry, its efficiency goes from a 34% minimum to a 75% maximum and for the cylindrical geometry it goes from 55% to 83%. Thus, the cylindrical geometry is preferred. In table 5.9, the parameters of the optimal RAC design are presented.

Table 5.9: Case Study RAC parameters with the optimal solution

CR	L [cm]	D [cm]	A [cm]	α/ε	n_{ducts}	h_{ducts} [mm]	w_{ducts} [mm]
0	10	10	4	0.15/0.05	8	3	0.5

Fig. 5.6 shows the direct relationship between the overall efficiency and absorbed beam power for the case study scenario. These plots are undeniably similar and illustrate the described phenomenon.

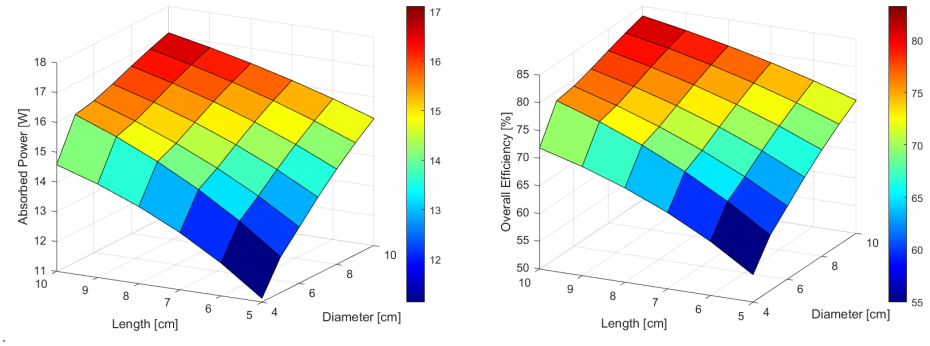

(a) Length and diameter influence on P_{abs}

(b) Length and diameter influence on η

Figure 5.6: Correlation between overall efficiency and absorbed beam power in the case study for the cylindrical geometry

Considering the other mass flows, lower mass flow values lead to slightly lower efficiency (maximum of 1% reduction from the 251 mg/s case to the 122.5 mg/s). Moreover, the trend of increase in efficiency with length and diameter remains. However, if one

keeps decreasing the mass flow, the amount of heat transferred to the propellant diminishes and the radiation loss starts becoming a significant part of the absorbed power. Therefore, the absorption efficiency trends start showing up as it is relevant to maximize the radiation energy retention and the optimal case scenario starts shifting to the lower dimensions.

A theoretical way to calculate the highest possible overall efficiency for a certain RAC geometry is to calculate it considering a duct length big enough that the RAC and the final propellant temperatures reach equilibrium, i.e., unitary heat exchange efficiency. By doing that to the case in table 5.8, the overall efficiency increases less than 0.5% in all cases. This small value is expected since most of the absorbed power is already going to the propellant.

Although, in this case, the optimization trend was simple, its extension to other cases needs caution. For example, higher cavity areas can allow the inner radiation loss to be significant and, thus, increasing the RAC's dimension to increase the absorption might not be enough to outweigh it.

In conclusion, the RAC can be optimized considering its overall efficiency. Regarding the case study, increasing its length and diameter leads to a higher overall efficiency and its performance is mainly limited by the absorbed power. This could be improved by increasing its absorptivity with a surface coating. Moreover, it was concluded that the results from the absorption efficiency section can be misleading regarding overall efficiency. For each scenario, the user must perform an individual optimization since the trend found might not apply.

5.6. BASELINES FOR LABORATORY MODEL

The next step in the engineering process is manufacturing the laboratory model for testing. For that, the insights gathered with the work of this chapter are taken into account. Mainly, one should strive for a cylindrical geometry with higher lengths and diameters to maximize beam power absorption and, for the expected mass flow values, a duct geometry that maximizes the perimeter and minimizes the area.

Table 5.10 shows the RAC parameters of the laboratory model manufactured. For a detailed description of the design and manufacturing process refer to Chapter 6.

Table 5.10: Manufactured RAC parameters

CR	L [cm]	D [cm]	A [cm]	α/ε	n_{ducts}	h_{ducts} [mm]	w_{ducts} [mm]
0	10	4	4	0.15/0.05	8	1	0.5

When comparing the parameters of the manufactured laboratory model to the optimal case (table 5.9), there are only two differences: the diameter and the height of the ducts. These differences are the result of manufacturing constraints and budget. Their optimal value is the maximum while the manufactured is the minimum of the defined range. Consequently, the absorbed power is reduced and the heat exchanger efficiency is lower as well. Table 5.11 shows the expected performance for the laboratory model. The efficiency is 72% which is lower than the optimal parameters case of 83%.

Table 5.11: Case Study - Laboratory Model expected performance at $\dot{m}$ = 251 mg/s

P_{abs} [W]	Q_{prop} [W]	$T_{eq,\text{RAC}}$ [K]	$T_{p,\text{f}}$ [K]	η [%]
14.6	14.3	365.9	347.7	72

5.7. CONCLUSIONS AND FUTURE WORK

In this chapter, we began by defining various efficiencies and their dependencies. We demonstrated that while absorption efficiency is challenging to quantify, the heat exchanger efficiency is more straightforward to determine. A case study related to the experimental aspect of this thesis was presented, providing a practical example of the optimization process and results.

The optimization tools were then introduced, starting with the absorption efficiency. It was shown that the optimal result varies depending on the governing equations. A trend for optimal values was identified, and the effects of the surface coating ratio, the RAC's conductivity, and the presence of convection were explored.

Next, the optimization of heat exchanger efficiency was discussed. It was found that the propellant fluid regime significantly influences the trends of optimal values. For laminar flow, maximizing the perimeter-area ratio was crucial, whereas turbulent flow favoured the smallest possible dimensions.

Finally, we optimized the overall efficiency. As previously explained, achieving a scenario where both efficiencies are optimal simultaneously is difficult due to their common input variables. The absorption efficiency results revealed having lower importance in the overall efficiency due to most of the absorbed power being transferred to the propellant and, thus, diminishing the impact of inner radiation loss. Therefore, absorption efficiency conclusions are only relevant in scenarios where inner radiation losses are a significant part of the power absorbed. In the case study, it was observed that increasing the cavity's length and diameter improved the efficiency, with values reaching around 83% across all mass flows.

The optimal case scenario RAC parameters were then compared to the laboratory model manufactured for the experimental part of the thesis. The differences reside in the diameter and duct height, reducing the theoretical efficiency from 83% to 72%, and are a result of manufacturing and budget constraints.

Future work regarding optimization focuses mainly on the improvement of the FEM model. Enhancements in the FEM model to include convective heat mechanisms will provide a more accurate and comprehensive optimization process, leading to better performance predictions and potentially higher efficiencies. Additionally, the optimization tools were not developed as user-friendly interfaces due to time restraints. This could be developed in the future to facilitate the process.

6

Experimental Design and Hardware

In this chapter, the process of the experimental set-up design and further manufacturing and assembly is explained in detail. Initially, the key locations for the development and testing are mentioned. Next, a concise report of the thruster design and manufacturing is given followed by the instrumentation hardware used in the tests. The design and manufacturing processes were inspired by the work and conclusion from the work of Takken [11]. The chapter ends with conclusions and recommendations for further work.

6.1. Locations

For this thesis, several locations were constantly visited, each having its distinctive purpose: the Student Walk-in Workshop (IWS) and the Employee Walk-in Workshop (EWW), the DEMO, the 3mE Welding facility, the Meetshop and the Cleanroom. The first four locations are related to the manufacturing of the laboratory model and the last two refer to used instrumentation and where the experiments were performed, respectively. For a more detailed description of the locations, refer to Appendix F.

Although not used, the laser facility is also mentioned in the appendix to explain the process that the author went through and the problems faced. This is useful information for following students.

6.2. Thruster General Requirements

The thruster developed has no requirements related to a specific mission. Thus, the general requirements follow down from the manufacturing and instrumentation constraints. In this section, the thruster requirements are given taking into account information that is explained in more detail in the next section.

The thrust is one of the measured parameters in the experimental procedure. Consequently, the thruster needs to be designed to operate within thrust levels that can be measured. The limiting factor is the instrumentation that measures it: load cell and test

bench. The load cell intended to be used had a maximum capacity of 100 mN. Moreover, the test bench could be easily assembled in a way to increase the relationship between measured and real thrust by 25%. Thus, the following requirement was defined:

- TGR-01: The expected experimental thrust must not exceed 125 mN.

In the planned testing, the only control variable is the inlet absolute pressure and, thus, the mass flow, directly proportional to the thrust, is a dependent variable. The critical mass flow is proportional to the nozzle's diameter and the smallest available drill at IWS is 0.5 mm. The expected thrust is determined by IRT, presented in Chapter 2.

Table 6.1: Nitrogen testing theoretical values - ideal conditions

p_c [bar]	3	4	5	6
$\dot{m}$ [mg/s]	137.9	183.9	229.9	275.8
F [mN]	54.8	79.7	104.6	129.5
I_{sp} [s]	40.5	44.2	46.4	47.9

Considering nitrogen as the propellant, an ambient temperature of 15ºC and pressure of 1 atm and a 0.5 mm diameter throat nozzle with only a convergent section, the theoretical values can be calculated for various chamber pressures (table 6.1). From the data, the chamber pressure can not exceed 6 bar as it no longer satisfies TGR-01. Also, if the nozzle diameter is increased, the possible testing pressures diminish. Thus, the nozzle throat diameter is selected as 0.5 mm. Regarding inlet pressure, this is limited to 6 bar. Although a 6-bar chamber pressure does not satisfy TGR-01, the thrust value is close to the limit value and there will be factors such as the pressure drop from the inlet to the chamber and the discharge coefficient which will reduce the real thrust to the allowed range.

6.3. THRUSTER DESIGN AND MANUFACTURING

In the section, an overview of the design and consequent manufacturing process of the thruster is given. Since the thruster being developed is not attributed to a specific mission, the requirement lists are mostly related to manufacturing constraints as well as experimental simplicity. For each component, first, the requirements are given, followed by the final design and manufacturing process.

6.3.1. RAC

REQUIREMENTS

Table 6.2: RAC design requirements

ID	Requirements	Rationale
RAC-01	The material must be approved for use in the IWS machines.	The author will use the IWS machines.
RAC-02	The material must be suitable for soldering or welding.	Due to the inner geometry, four sub-pieces need to be made and assembled.
RAC-03	The material has to have high thermal conductivity.	Uniform temperature throughout the RAC which is an assumption of the zero-order model (Chapter 4).
RAC-04	The wall thickness of the pieces must be a minimum of 2 mm.	Instruction given by the IWS staff.
RAC-05	The material must withstand a maximum operating pressure of at least 10 bar.	Maximum range of the pressure sensors.
RAC-06	The design must be cylindrical with linear ducts.	Conical sections and spiral ducts are more difficult to manufacture.
RAC-07	The diameter must be sufficient to capture all laser radiation.	Reduces test set-up complexity by avoiding the need for radiation protection.
RAC-08	The cavity's length must be at least twice its diameter.	Improves the absorbed radiation power (Chapter 3).
RAC-09	The inlet, ducts and outlet must be big enough to not form a nozzle.	No significant pressure drops before the nozzle allowing for it to choke.

The list of requirements for the RAC can be seen in table 6.2 and these guide the design process.

DESIGN

The material chosen for the RAC was aluminium since it satisfies the first three requirements. Steel was the other available option but it is harder to manufacture and has an 80% lower thermal conductivity. The rest of the requirements defined the geometrical design.

Considering all the requirements, a final RAC design was made. The RAC is a cylinder with a height of around 110 mm and a maximum outer diameter of 60 mm. For the intended laser experiments (5^o half-beam angle and RAC at 40 cm distance), all of the laser radiation would hit the RAC, satisfying RAC-07. The cavity has 40 mm diameter and 100 mm length, respecting RAC-08. Both the inlet and outlet diameters are 3 mm. When the propellant goes through the inlet, it passes through a manifold ring which guides it to the straight slits (RAC-06). There are 8 rectangular slits of 1mm by 0.5 mm where the propellant flows through. Considering the nozzle's dimensions, which are given next, no

section of the RAC forms a second nozzle in the thruster (RAC-09). Consequently, the main problem that Takken [11] experienced is avoided.

Regarding the maximum operational pressure, values have been calculated for the inlet and outlet pipe and the inner slits using Barlow's equation. Regarding the former, with a safety factor of 10, the maximum allowed pressure is around 83 bar and for the slits (assuming a circle with 1 mm of diameter, which should result in the worst case) is around 165, double the previous number. Therefore, the RAC satisfies its maximum operating pressure requirement (RAC-05).

MANUFACTURING

The RAC was the first component to be manufactured (Fig. 6.1). Due to its internal structure, it is not possible to build it in one single piece. A two-part manufacturing process (two capped cylinders) with consequent welding was proposed but the IWS staff recommended separating the cylinders with their respective caps. Consequently, four pieces were constructed: the inner cylinder, the outer cylinder and their caps. Although available free of charge in the IWS, the aluminium pipes were of small size and too much material would be wasted if an aluminium rod was used. Therefore, the author had to buy two differently-sized aluminium rods to carve the cylinders. The cost for twice the amount needed (in case it had to be redone) came to around 70€.

The outer cylinder was a simple piece compared to the inner cylinder and only the lathing machine (Fig. 6.1a) was needed. On the other hand, the inner cylinder had ducts which required the use of the milling machine with a saw (Fig. 6.1b) after the rest of the layout was carved with the lathe. Lastly, the caps were created with the lathe. The manufactured pieces before welding can be seen in Fig. 6.1c.

After manufacturing the four RAC sub-pieces, they had to be welded together. As mentioned before, this process was done by a friend of the author at the 3mE welding facility. Aluminium is not as easy to weld as steel due to its high thermal conductivity and, therefore, if not done by an experienced user it can go wrong. The assembled RAC can be seen in Fig. 6.1d.

6.3.2. CONNECTION PIECES

REQUIREMENTS

There are several connection pieces in the thruster assembly. Depending on their purpose, their requirements are different. Nevertheless, an overall requirements list is provided (table 6.3.

(a) Lathe machine at IWS

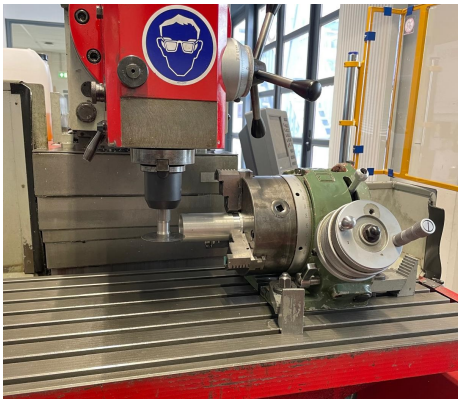

(b) Cutting the slits with the milling machine

(c) RAC's four sub-parts before welding

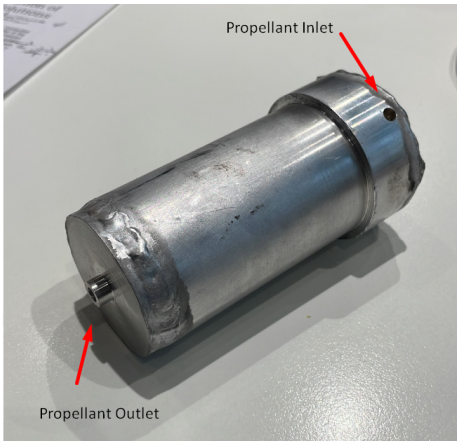

(d) RAC pieces welded together

Figure 6.1: RAC manufacturing process

Table 6.3: Connection components requirements

ID	Requirements	Rationale
CON-01	The material has to have low thermal conductivity.	Lower RAC energy losses by conduction and respect maximum temperature instrumentation requirements.
CON-02	The dimensions have to be able to fit the instrumentation where required.	Instrumentation needs to fit to collect data
CON-03	The dimensions cannot form nozzles.	No significant pressure drops before the nozzle caused by a second nozzle.

DESIGN

The material chosen for the connection pieces when manufactured by the author was steel due to its low thermal conductivity. This avoids energy losses by conduction as well as lowering the temperature suffered by the instrumentation.

Three connection pieces were manufactured: the inlet piece, the thermowell piece and the pressure chamber piece. The inlet piece is a three-end piece whose purpose is to connect the RAC to the feed system and to measure the inlet pressure. Thus, the dimensions were made to fit one pressure sensor in one end, to connect with the RAC with a threaded connection in another end and the last end to a barb connection which will be connected to the plastic tube from the feed system. The thermowell piece is located after the RAC and before the nozzle to measure the temperature with a thermowell. The pressure chamber piece is connected to the nozzle chamber to accommodate the other pressure sensor and read the chamber pressure.

Additionally, two stainless steel pipes were purchased online to enhance overall conductive thermal insulation from the RAC to the instrumentation. Each pipe has a 1 mm inner diameter, 3 mm outer diameter, and a length of 20 cm, satisfying CON-03. These characteristics were chosen as increased insulation to the instrumentation is achieved with longer lengths and reduced diameters. These dimensions are too small to be constructed at IWS and that is why they were ordered. One of them was cut in two parts. Thus, one piece connects the RAC to the thermowell piece, another the thermowell piece to the nozzle and the last the nozzle to the chamber pressure piece. A schematic of the connection pieces can be seen in Fig. 6.4.

MANUFACTURING

The manufacturing of the three pieces was rather simple and the lathing machine was mainly used. Any threads and holes were then threaded and drilled with the respective machines. To prevent any leakage, any connection (threaded or not) between these pieces was soldered with silver.

6.3.3. NOZZLE

REQUIREMENTS

Table 6.4: Nozzle design requirements

REQ-I	Requirements	Rationale
NOZ-01	The material has to be steel.	Ability to solder with the connection pieces and manufacturing done at IWS.
NOZ-02	The throat dimension needs to be small enough to cause choked flow.	It would not cause sonic flow.
NOZ-03	The nozzle only has a convergent section	A divergent section would increase the manufacturing complexity.
NOZ-04	The thrust produced needs to be within the test bench's possible measuring ranges.	Otherwise, the produced thrust cannot be measured.
NOZ-05	The nozzle must allow perpendicular alignment with the bench.	If angled, only one portion of the thrust would be measured.
NOZ-06	The nozzle must be designed with a closing mechanism.	Needs to close for leak testing

Regarding the nozzle, the list of requirements is shown in table 6.4.

DESIGN

From the requirements, the material of the nozzle piece is already defined to be steel (NOZ-01). Next, the nozzle piece was designed into three sub-parts: the nozzle part, its cap and its support.

Besides the converging section which ends at the nozzle throat without any diverging section (NOZ-03), the former is a cuboid structure with two holes: one to connect to the propellant flow and the other connected to the chamber pressure piece. The throat has a 0.5 mm diameter which is the smallest drill available at IWS. This will cause a choked flow following requirement NOZ-02. From the ideal rocket theory, the thrust levels achieved go from 50 to 110 mN which the test bench can measure (NOZ-04). The end of the nozzle is threaded so the cap can be inserted and the nozzle closed (NOZ-06).

The nozzle support piece is made to fit the nozzle and has two threaded holes perpendicular to the nozzle. These threaded holes allow screws to go through and attach the nozzle support to the thruster support. Consequently, the nozzle and, by extension, the propellant exit flow are aligned perpendicularly to the test bench (NOZ-05).

Regarding the nozzle cap, it is simply a cylinder with a threaded hole to close out the nozzle exit.

MANUFACTURING

Although not complex, the nozzle was difficult to manufacture due to its small dimensions. The 0.5 mm drill breaks quite easily since the drill has to be manually made and

the machines are not specifically made for these dimensions. After several trials, the throat production succeeded. The nozzle ended up having a 70º converging section going from 2.5 to 0.5 mm. Next, the milling at EWS was used to square off the nozzle to fit in its support.

The nozzle support was fully done in the milling machine (Fig. 6.2a). Due to its small size, it was also challenging but eventually, the manufacturing was successful. After the two sub-parts were manufactured, the nozzle was inserted into its support and welded together to form a unique piece. In Fig. 6.2b, the nozzle and its support before welding can be seen.

Regarding the nozzle cap, it was done in the lathing machine fairly quickly due to its simplicity.

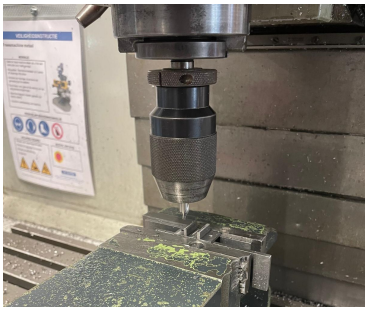

(a) Nozzle support manufacturing in the milling

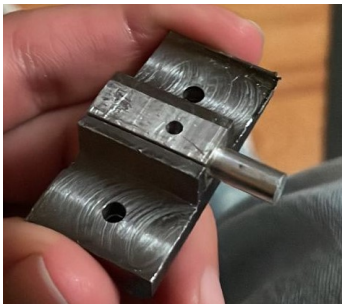

(b) Nozzle and its support before welding

Figure 6.2: Nozzle manufacturing

6.3.4. THRUSTER SUPPORT

REQUIREMENTS

Table 6.5: Thruster support requirements

ID	Requirements	Rationale
SUP-01	The material has to be readily available at IWS	Reduces costs and is convenient.
SUP-02	The material has to have low thermal conductivity.	It is in contact with the RAC and other thruster elements
SUP-03	The support has to be able to support and fix a cylinder	The RAC is cylindrical
SUP-04	The support has to be adjustable for other thruster configurations.	Can be used by next students
SUP-05	The support has to secure the nozzle in a fixed position.	The nozzle cannot change its orientation throughout the experiments
SUP-06	The support has to be able to be put in the thrust bench	Otherwise, it would not be possible to use it in the test bench and, thus, for testing

Regarding the thruster's support, the requirements are presented in table 6.5.

DESIGN

The support is made of carbon steel since it can be used at IWS, has low thermal conductivity and is free of charge (SUP-01 and SUP-02).

At the bottom, a rectangular steel base is used. The lateral sides are bent to improve stability by increasing resistance to bending. Four holes 2.5 cm apart are made so the support can be connected to the thrust bench by screws. In addition, two more holes are made to fix the nozzle. Then two rectangular hollow steel sections are inserted vertically. The bigger one is fixed to the base and the other can slide inside. The one inside can be fixed by screwing two screws that pass by threaded holes in the bigger rectangular hollow section. The top rectangular section is connected to a triangular piece where the RAC can be stably put.

MANUFACTURING

The rectangular steel base was laser-cut from a steel plate free of charge (fig. 6.3a) and then the lateral sides were bent with a metal-bending machine at IWS.

The rectangular hollow sections and the triangular piece were already available at IWS. The bottom rectangular hollow section had two threaded holes made and then welded into the steel base. Lastly, the inner rectangular hollow section was welded to the triangular piece.

The final thruster can be seen in Fig. 6.3b.

(a) Laser cutting machine used for the support's base

(b) Thruster support assembled

Figure 6.3: Thruster support manufacturing

6.4. THRUSTER ASSEMBLY

Fig. 6.4 shows all the thruster pieces (except for the thruster support) in an exploded manner before they were assembled. Also, before assembly, it is essential to verify that all components have been produced according to the plan.

As mentioned, every connection between steel and stainless steel was silver soldered. Thus, only two connections are leak-tightened with Teflon tape: the inlet connection piece to RAC and RAC to one of the stainless steel connections. The pressure sensors are leak-tight due to their washes. The thermowell washer was unsuccessful in preventing leaks. Thus, the thermowell connection was closed with fire sealant as mentioned in the leak testing chapter. The fully assembled thruster with its support and no instrumentation is shown in Fig. 6.5.

Unfortunately, during preliminary testing, it was found that the connection between the nozzle chamber and the chamber pressure piece got clogged. This could have been the result of rust formation or the silver soldering blocking the pipe. Consequently, the nozzle chamber pressure could not be measured in the following experiments. Alternatives for future designs to avoid this problem are described in section 8.5.

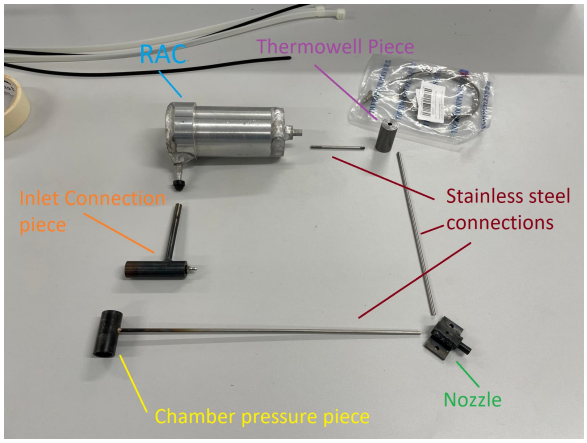

Figure 6.4: Exploded view of the thruster

(a) View A

(b) View B

Figure 6.5: Fully Assembled Thruster

6.5. TEST SET-UP HARDWARE AND SOFTWARE

A clear understanding of how the test set-up hardware works and its limitations is crucial for a successful experiment. In addition, code has to be developed for each instrumentation device. Fortunately, a significant portion of the Labview code for the relevant instrumentation had already been produced by Versteeg [41] and is available on the Cleanroom's desktop. Thus, only case-specific adjustments had to be performed by the author. In this section, all the hardware used in testing as well as how they are connected

is explained.

Table 6.6: Experimental instrumentation overview

Component	Function	Reference
Cleanroom Desktop	Read and save data, control VTDC	-
PC	Read and save data	-
IFM PU5404 pressure sensors	Measure inlet and ambient absolute pressure	Datasheet G.1
Brooks Mass flow sensors	Measure inlet mass flow	Manual [42]
Thermowell and MAX6675	Measure propellant temperature	Online Guide [43]
LSB200	Measure experienced load	Datasheet G.2
Scaime CPJ	Amplify LSB200 signal	Manual [1]
Nitrogen Feed System	Supply nitrogen to the thruster at a controlled pressure	-
VTDC	Produce known force to calibrate test bench	-
TB-50m	Measures produced thrust	
- NI USB-6008 DAQ	Measure, process and transmit data from sensors to the desktop and PC	Online specifications[2]

An overview of the used hardware instrumentation is available in table 6.6. Additionally, a concise schematic showing the location of the measurements is shown in Fig. 6.6. The green blocks are thruster components, the blue blocks are the measuring hardware, the yellow blocks are the computers used and the red ones are the hardware that connects them to the sensors. The test bench in purple connects the nozzle and VTDC to the load cell and the nitrogen feed system is white coloured.

6.5.1. CLEANROOM COMPUTER AND PC

In the cleanroom, an offline desktop is available for the conducted experiments. It has been used throughout the years for instrumentation data acquisition from several different devices. Consequently, the electronics for the used instrumentation were already set up and the author only had to become familiar with it. This consists mainly of USB connections as well as a DAQ device integrated with a PCIe card. For an extensive look and explanation of this setup, the work of L. Cramer [44] is recommended. Also, some of the LabVIEW code was already available on the desktop and only adaptations to the author's case were needed. The instrumentation that is dealt with by the offline desktop is the mass flow sensor, the power supply to the variable-turn density coil and the load

[1] SCAIME CPJ Manual
[2] NI USB-6008 DAQ Specifications

Figure 6.6: Schematic of the experimental hardware

cell.

Besides the cleanroom's computer, the author uses its PC to acquire data. The pressure sensors' DAQ and the thermowell's Arduino are both connected to the PC via USB. Changes could have been made to use only the cleanroom's computer. However, the instrumentation was already functioning in the PC and any changes would take an unknown time to execute and could even lead to unwanted modifications in other devices.

6.5.2. PRESSURE SENSORS

The pressure sensor is a device that measures the local pressure of the propellant. Pressure is a fundamental parameter in the calculation of the expected thrust. Moreover, by having two or more pressure readings, pressure losses suffered in that segment can be determined. Consequently, two pressure sensors are chosen to incorporate the test setup: one before the RAC and another at the end reading the nozzle's pressure.

The pressure sensors were borrowed from the Meetshop and are both IFM PU5404. The datasheet is available in the appendix G.1. They are connected to a NI USB-6008 DAQ that is then connected to the author's PC via USB. The measuring range is from 0 to 10 bar with an accuracy of 0.5% and connections to the thruster are done via G1/4" threads. Jacques Brenkman[1], the Meetshop responsible, provided the Labview program to simultaneously read both sensors. For all experiments, the measurement frequency is set to 10 Hz.

The maximum operating temperature conditions is 90ºC and the main reason for

[1] J.A.Brenkman@tudelft.nl

wanting to thermally insulate them from the RAC which would experience higher temperatures.

6.5.3. MASS FLOW SENSORS

The mass flow sensor is a device that measures the mass flow passing through. In the cleanroom, this device is mounted at the end of the propellant feed system, just before the last plastic tube. At the time of the experiments, two mass flow sensors were available:

1. Brooks 5850S Smart Mass Flow: Range from 0-2 ln/min of nitrogen (0-41.69 mg/s),

2. Brooks 5851S Smart Mass Flow: Range from 0-47.3 ln/min of nitrogen (0-860.83 mg/s).

The two mass flow meters measure different ranges. No information about the last calibration is given for the two sensors. The measurement accuracy is 0.5% but, at lower mass flow ranges than 20% of its full range, the sensor becomes more inaccurate [42]. Hutten [45] mentions that the Brooks 5850S mass flow sensor can not measure below 1% of its full range. This has been confirmed for both of the sensors.

Both sensors' connection to the cleanroom computer are equal which facilitates their change. They are connected to a DAQ device by a Printed Circuit Board (PCB) [11]. However, when making the change, the voltage read-out needs to be adjusted in the Labview code since they are 0-5V and 1-5V respectively.

For this thesis, both mass flow sensors were used. The first, which has a lower range, was used to measure the leak rate of the thruster. The second was used for the nitrogen testing since the expected mass flow values were above the first sensor's range.

6.5.4. THERMOWELL AND MAX6675 AMPLIFIER

The thermowell or thermocouple is a device capable of measuring absolute temperature due to the Seebeck effect. There are several types, each made with different metal combinations.

A thermowell was added to the thruster after the RAC to measure the propellant's final temperature. However, no thermowells were available at the cleanroom or the Meetshop. Thus, a type-K thermowell was ordered from AliExpress at a 4.40€ cost. Despite it being advertised as an M6 thread, it was a 1/4" thread. The typical maximum temperature range for type-K thermocouples is at least 1000ºC which is way above the melting point of aluminium. Unfortunately, not much information about the thermowell is given by the vendor.

To use the thermowell, a thermocouple amplifier is needed. The used thermocouple amplifier is the MAX6675 which was ordered from AliExpress as well at 1.65€ per piece. The MAX6675 amplifies the voltage from the thermocouple allowing it to be measured by the Arduino. Next, the code to read the temperature needs to be uploaded into the Arduino. Lastly, wires connecting the Arduino and the MAX6675 are inserted. These steps were performed according to the available online guide "Arduino: K-Type Thermocouple with MAX6675" [43]. Fig. 6.7 shows what the thermowell setup looks like.

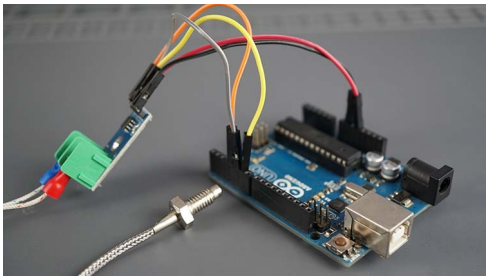

Figure 6.7: Example of thermowell setup assembled [43]

The thermowell was set to read a temperature measurement per second. On the other hand, the resolution is 0.25ºC and can not be changed. This is a result of the 12-bit resolution of the MAX6675.

6.5.5. LOAD CELL AND SIGNAL AMPLIFIER

The load cell is a sensor that can measure the experienced force by outputting a related voltage. The used load cell is the Futek LSB200 [2] (Fig. 6.8a). The Futek LSB200 available online data sheet can be consulted in Appendix G.2. It is fed with 5V, has a 100g capacity and, contrary to what the available datasheet states, has a sensitivity output of 1.0893 mV/V. Considering the data sheet, the combined uncertainty of the load cell by calculating the root mean square is ± 0.15 g or ± 1.4715 mN.

The hardware connections from the load cell to the computer were already set for another load cell compatible with this one. Only changes in the Labview code were needed.

The load cells were also different physically. Unlike the LRF400, the LSB200 has one threaded hole in each side and is, therefore, secure by two M3 screws. One of the screws is screwed into the load cell bypassing a threaded hole in the thrust bench, making a physical connection with the thrust bench. The other screw is screwed into the load cell but needs to be fixed somehow. Thus, a new support to fixate the load cell to the test bench was needed. A new load cell support was 3D printed to fit precisely into a section of a Boikon profile while also allocating for the screw that would connect it to the load cell (Fig. 6.8a).

Another remark is that the zero of the load cell is highly sensitive to the position of the load cell's cable. Therefore, taping it down to avoid any movement and being careful to not cause any changes is essential.

Like the thermowell, the load cell needs an amplifier so the NI USB-6008 DAQ can read the produced signal. The SCAIME CPJ (Fig. 6.8b) is a sensor analogue conditioner that can be used as a signal amplifier and was borrowed from the Meetshop. The signal is amplified up to 10 V. The maximum load to be measured can be adapted to 10V, thus, increasing the resolution of the measured thrust. This is done by selecting the correct

[2] Two load cells were initially available in the cleanroom: the Futek LRF400 and the Futek LSB200. The measuring ranges are 100 mN and 1000 mN, respectively. Initially, the Futek LRF400 was the choice since it had recently been used by Cramer [44] and the setup was done. Despite the expected thrust exceeding 100 mN, by modifying the position of the load cell in the thrust bench, this problem would be surpassed effortlessly. However, the author broke the load cell while trying to adjust it from its position.

(a) Futek LSB200 and its support

(b) SCAIME CPJ

Figure 6.8: Load cell and amplifier

sensor sensitivity. The calculation for it is presented in the SCAIME CPJ's manual[3] and is as follows:

$$\text{Sensitivity} = \frac{\text{max. load measured}}{\text{load cell capacity}} \cdot \text{load cell's sensitivity.} \tag{6.1}$$

After the calculation, the user checks what jumper position has the value inside its range and inserts it there. This selection procedure for this thesis' experiments is explained in Section 7.1.1.

6.5.6. NITROGEN FEED SYSTEM

The feed system used in these experiments is the one available in the cleanroom (Fig. 6.9). Gaseous nitrogen is used due to its non-reactive properties, relaxing the needed safety measurements.

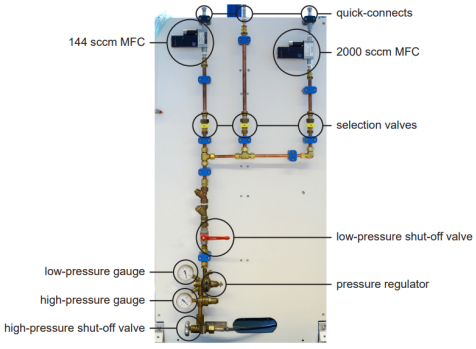

Figure 6.9: Nitrogen gas feed system with components indicated [45].

[3] SCAIME CPJ Manual

The propellant is stored in a high-pressurized tank (200 bar maximum pressure). After opening the storage tank, the nitrogen flows through a black pipe until it reaches a high-pressure shut-off valve. Since it is a high-pressure pipe, the black pipe requires caution. Next, a pressure regulator valve reduces the pressure from the bottle from 0-200 bar to 0-15 bar. The user can select the end pressure at this valve by rotating the valve. The low-pressure gauge has a 0-15 bar range with 0.5 bar resolution. There is no information about its accuracy, however, this is not a significant problem since the thruster inlet pressure is being measured as well. A low-pressure shut-off valve follows, allowing flow to reach the three selection valves. Depending on the pipe to be used, the correct selection valve is turned on to allow flow. All the valves are operated manually. After the selection valve, the mass flow sensor is placed. For the tests, only one branch of the feed system is used with the mass flow sensor being switched depending on the experiment. After the mass flow sensors, a plastic pipe guiding the flow to the thruster is connected to the feed system via quick-connect.

The nitrogen tank is provided by the TU Delft Gassenteam. As soon as the nitrogen tank pressure is not enough for the required experimentation, instructions to follow are displayed on the feed system's board.

6.5.7. VARIABLE TURN DENSITY COIL

The Variable-Turn Density Coil (VTDC), developed by Bijster [46] in 2014, is a force-producing device used in test bench calibration (fig. 6.10). By creating a homogenous magnetic field induced by electrical current, the magnet inside the coil suffers an acceleration and, therefore, produces force.

The relation between current and force was studied in the past by Versteeg and Papadimitriou, achieving a 0.826 mN A^{-1} with 3σ confidence interval of ± 0.006 mN A^{-1}. Takken [11] reported a 0.823 mN A^{-1} value when calibrating the TB-50m test bench. This 0.4% reduction could have been the result of human error, imperfect alignment or magnetic computer interference [11].

The coil is connected to a power supply, allowing for control of the induced current. The power supply is then connected to the cleanroom's computer. Consequently, the induced current can be controlled via Labview and the main structure of the code was already present.

6.5.8. TEST BENCH

For this thesis, the TB-50m is used as the test bench and its description is taken from the Takken [11]. Despite suffering modifications throughout the years, the TB-50m main concept has prevailed: a beam is mounted in a bearing, allowing it to freely rotated. The thruster is mounted on one side while the load cell is set up and fixed on the other side. Whenever thrust is produced, a force is produced to rotate the beam but since the beam is fixed, a counter-acting force is produced and measured by the load cell. By knowing the distance to the centre of both parties involved, the measured force can be translated into the produced thrust.

The beam has numerous and consistently spaced M3 thread holes. This allows for a firm instalment of the thruster via screws. Moreover, the LSB200's threads are also M3 which simplifies the connection process to the test bench to require only one screw. This

was not the case with the LRF400, which had a M5 thread.

The TB-50m test bench with the load cell and its structure and the Variable-Turn Density Coil can be seen in Fig. 6.10. This is the test set-up for the first stage of the test bench calibration. For a picture of the test bench with the thruster and all its instrumentation, refer to the test bench calibration section.

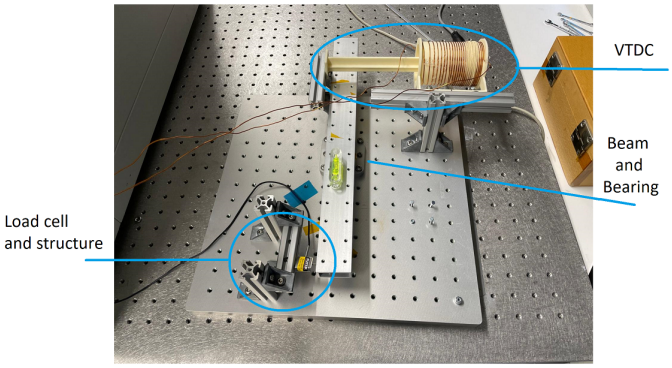

Figure 6.10: TB-50m test bench with load cell and VTDC

6.6. SUMMARY

In this chapter, the design, manufacturing, and assembly of the experimental setup for thruster testing are described in detail. The general requirements for the thruster are presented, emphasizing constraints due to manufacturing and instrumentation limits. Following these guidelines, the design rationale and manufacturing process of each component was given. Lastly, the hardware used for the test setup was presented, explaining the roles of the various instruments. A schematic was provided to illustrate the integration of these components within the experimental framework.

Regarding the chapter's purpose:

- **Comprehensive Understanding:** It provides a thorough understanding of the experimental setup, from design to final assembly, crucial for replication or further development.
- **Guidance for Replication:** Future researchers can use the detailed guidance on design and manufacturing processes to replicate or build upon this research, avoiding common pitfalls.
- **Reference for Troubleshooting:** Detailed component descriptions act as a reference for troubleshooting issues during experiments.
- **Foundation for Further Work:** The conclusions and recommendations provide a foundation for future research, suggesting areas for improvement and guiding further study.

By documenting the experimental design and hardware, this chapter aims to ensure the reader can fully understand, replicate, and build upon this setup for future research.

7

PRELIMINARY TESTS

Conducting preliminary tests plays a crucial part in validating the results obtained from nitrogen testing. Consequently, calibration of the test bench to ensure a correct thrust measurement and leak testing to quantify the mass flow losses through the system are performed. The test procedures are described in the appendix H. The final step of preliminary testing involves conducting an initial nitrogen cold flow test. This test verifies that all equipment is functioning correctly and that data is being accurately recorded. The results of this test are not displayed since its primary purpose is to confirm the system's proper operation before the actual test.

7.1. THRUST MEASUREMENT CALIBRATION

As mentioned, the produced thrust is measured indirectly by a load cell embedded in a thrust bench. Thus, the relationships between the actual thrust and the load cell measurements need to be defined. Moreover, ensuring the reliability and consistency of these relationships is crucial for the accurate assessment and interpretation of experimental results.

The procedure for the load cell calibration was taken from Takken [11]. Regarding the test bench calibration, the procedure was inspired by the work of Verstegg [41], however, it had to be slightly adapted since he used another test bench.

7.1.1. LOAD CELL

The LSB200 load cell is the first item to be calibrated. Since no previous mention of the weight-voltage output relationship was found, establishing that is required to determine the measured load.

The first step is to adjust the Scaime CJP signal amplifier. After connecting it to the load cell, the signal amplifier is connected to the computer and the measured voltage can be seen. By fine-tuning the relevant signal amplifier's screws, the zero-load scenario can be matched to zero voltage. Additionally, by repositioning the sensor sensitivity jumper in the signal amplifier, the maximum load to be measured can be adjusted.

Next, known weights are applied to the load cell in a vertical position and their voltage output is measured. Thus, this measure is performed at compression of the load cell. These weights are available in a box inside the cleanroom and were weighted again with the Mettler Coledo AG electronic scale (accuracy of 0.1 mg). In Fig. 7.1, the relationship between output voltage and weight mass is shown which is irrefutably linear due to the unitary R^2.

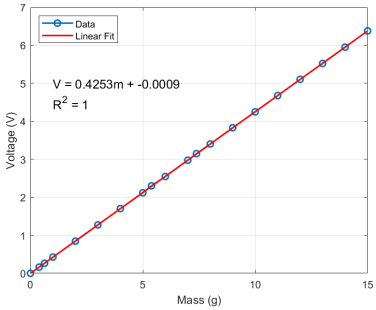

Figure 7.1: LSB200 relationship between output voltage and mass load

By using a gravitational constant of 9.81 m/s^2, the relationship between the weight and the output voltage is:

$$F_{LSB200} = 23.066\Delta V_{LSB200} \pm 1.4715\text{mN}, \tag{7.1}$$

where F_{LSB200} is the measured load in mN and ΔV_{LSB200} is the difference in V between the measured voltage when a load is applied and when a load is not applied. The uncertainty derives from the load cell data sheet only since the linear fit uncertainty is ignored (lower than 0.01%).

The no-load voltage output does not have to be null, what matters is the voltage difference between the no-load and load case. For example, when the zero voltage is set as the no-load scenario when the load cell is vertical, as soon as the load cell is positioned horizontally (which is the case in the test bench), the no-load scenario will not have zero voltage anymore. Nevertheless, the linear relationship between the output voltage and the endured force remains the same.

7.1.2. TEST BENCH

After the load cell's calibration, it can be added to the test bench, completing its assembly. Since it was assembled with a new load cell, calibration is needed to understand the effect that any produced thrust translates into measured thrust by the load cell. Thus, a new relationship is studied: produced thrust versus measured thrust.

The calibration is performed by using the VTDC, introduced in subsection 6.5.7. Takken [11] found that the coil overheats when maintained at 16 A or above for extended periods. This limits the produced forced by the coil. Regarding the placement of the coil, it was inserted as far as possible to the centre of the rotating beam but allowing the

placement of the thruster at the edge. Consequently, the relationship between the coil induced force F_{coil} can be related to the F_{LSB200} by:

$$F_{coil} = F_{LSB200}\frac{d_{LSB200}}{d_{coil}} = F_{LSB200}\frac{175}{117} = (1.4957 \pm 0.0077)F_{LSB200}, \tag{7.2}$$

where d_{LSB200} and d_{coil} are the distances of the load cell and the coil, respectively, from the beam's rotating point. These were measured with a ruler several times on different occasions to ensure correct measurement. The accuracy of these measurements is defined as ± 0.5 mm since it is half the ruler's smallest measurement. This gives an absolute uncertainty of 0.008 which translates to 0.535%.

Considering the relation between load cell measured force and voltage, then the induced force F_{coil} can be calculated by:

$$F_{coil} = 34.5 * \Delta V_{LSB200} \pm \sqrt{4.84 + 0.0315 * \Delta V_{LSB200}^2}. \tag{7.3}$$

For each calibration run, the software increases the current of the coil from 0 A to 16 A in 1 A steps with a duration of 20 seconds each. In the end, the current goes back to zero. Compared to previous work, the step size has been increased (from 0.5 A to 1 A) as well as its duration reduced (from 30 s to 20 s steps) to reduce the overall test time and potential overheating of the coil.

A calibration run is only considered successful if the behaviour between force and current is linear and the no-load voltage at the beginning and the end of the test does not differ more than 5%. Returning to the previous no-load voltage indicates that the load cell most likely did not suffer any changes in the no-load voltage throughout the run. After each successful calibration run, it was noticed that the coil presented better results if enough time (around 5 minutes) was given to cool down until the next test. Moreover, usually, the first two or three runs of the day presented non-consistent readings.

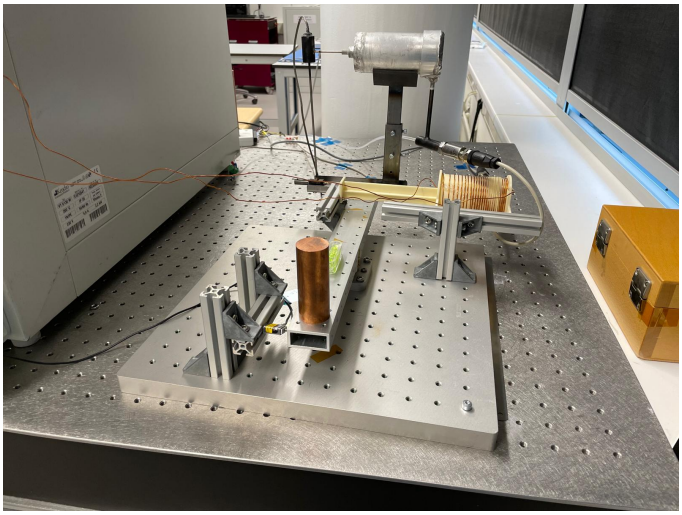

Figure 7.2: Test bench with the thruster connected to its instrumentation on.

Two calibration scenarios are tested: without (fig. 6.10) and with the thruster on the test bench (fig. 7.2). The former evaluates the effect of the test bench on the load cell measurement, while the latter evaluates the effect of the thruster on the thrust bench. For each scenario, ten consecutive successful runs were executed before the cold flow testing and after (so in total, 20 runs for each scenario).

When calibrating the test bench with the thruster, an appropriate counterweight positioned on the other side of the beam is fundamental. The thruster's weight creates an unbalance in the rod and the load cell, since it is a solid object, adjusts to this unbalance by fully extending. Thus, the load cell reaches its maximum voltage reading and does not capture any forces produced by the coil. In this case, solid copper bodies were used with a total weight of around 1 kg to balance out the thruster.

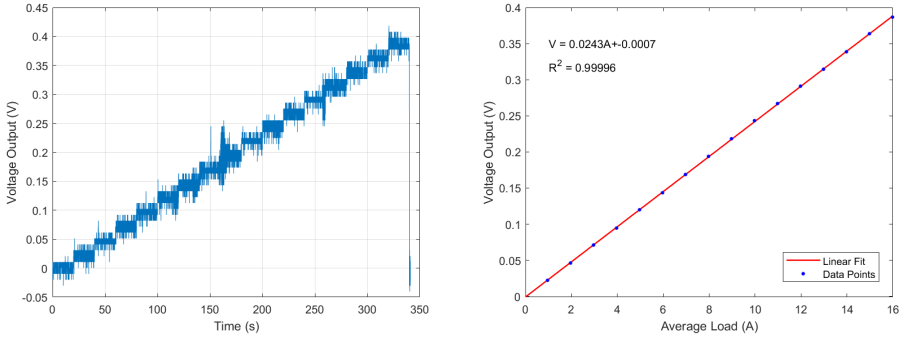

(a) Voltage output throughout the experiment

(b) Averaged voltage at each step

Figure 7.3: Example of successful calibration run without thruster on the test bench

In Fig. 7.3, an example of the data acquired in a successful calibration test without the thruster on the test bench is shown. In the first image (Fig. 7.4a), the increase in load is evident in the 20-second steps. After the time ends, the voltage returns near the previous no-load case as desired. Additionally, noise is always present. Periods where the noise increases are commonly related to movements in either the cleanroom or even in the hallway. Nevertheless, when averaged out, the effects of the noise are removed and a clear linear trend between the force and the voltage is found (Fig. 7.4b). From the relationship, the value of the coil-induced force can be determined with equation (7.2) and in this example is 0.8389 mN $A^{-}1$.

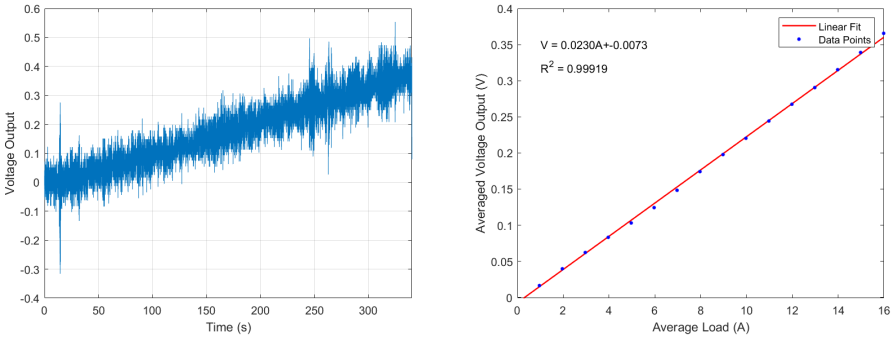

(a) Voltage output throughout the experiment

(b) Averaged voltage at each step

Figure 7.4: Example of a successful calibration run with the thruster on the test bench

In Fig. 7.4, the data for a successful calibration with the thruster connected to all the instrumentation on the test bench is illustrated. Compared to the previous case, there is a clear increase in noise. The mass increase in the system probably led to the amplification of existing noise. Despite the noise, when averaged out, the behaviour is once again linear.

Table 7.1: Averaged calibration results before the cold flow test

F_{coil}	Mean	95% C.I.
Thruster off (mN A $^{-1}$)	0.8253	[0.8197, 0.8310]
Thruster on (mN A $^{-1}$)	0.7926	[0.7856, 0.7997]

By using equation 7.3, the force theoretically produced by the coil in each test can be determined. In table 7.1, the mean as well as the 95% confidence interval of the 10 calibration tests for each scenario before the cold flow test are presented. In the first case (thruster off), the mean is close to the previously mentioned result of 0.826 mN A $^{-1}$ and, thus, no major effect is at play. After assembling the thruster and its connections into the thrust bench, theoretical F_{coil} is reduced by around 4%. The confidence intervals are undoubtedly small enough (around 2% width) to consider the calibration a success.

Despite the actual produced force by the coil staying the same, by adding the thruster, the theoretical force produced by the coil is reduced. Consequently, the addition of the thruster setup to the test bench affects the relationship between the measured and actual thrust by adding stiffness and/or friction. The stiffness ratio λ is:

$$\lambda = \frac{F_{coil,on}}{F_{coil,off}} = 1.0413 \pm 0.01, \tag{7.4}$$

where $F_{coil,on}$ and $F_{coil,off}$ are the theoretical F_{coil} with the thruster on and off the test bench, respectively.

To sum up, the experimental thrust F_{exp} is calculated by:

$$F_{exp} = F_{LSB200} \frac{d_{LSB200}}{d_t} \lambda = 22.417 \Delta V_{LSB200} \pm \sqrt{2.045 + 0.0541 \Delta V_{LSB200}^2}, \tag{7.5}$$

where d_t is the distance of the nozzle to the rotating point of the beam (187.5 mm).

After the cold flow testing, before disassembling the thruster and the test bench, new calibrations of the bench were made to ensure that throughout the experiments the stiffness ratio did not suffer any variations. The results are shown in table 7.2 and since the results are undeniably close it is assumed that the calibration did not suffer noteworthy alterations.

Table 7.2: Averaged calibration results after the cold flow test

F_{coil}	Mean	95% C.I.
Thruster off (mN A $^{-1}$)	0.8261	[0.8202, 0.8321]
Thruster on (mN A $^{-1}$)	0.7936	[0.7852, 0.8020]

7.2. LEAK TESTING

Despite the presence of a mass flow sensor in the test setup, not all of the flow contributes to the generation of measurable thrust. A portion of the measured mass flow tends to escape through potential leaks within the system. Therefore, it becomes essential to identify and rectify these leaks. Minimizing the leaks to the greatest extent possible is desirable. Subsequently, quantifying the leak rate becomes imperative to accurately determine the actual mass flow responsible for generating thrust. In this section, the adjustments made to the thruster to reduce leakage are mentioned and the final leak rate is quantified. The experimental procedures for leak testing were adapted from the work of Versteeg [41] with small alterations due to different thruster components.

7.2.1. METHODOLOGY AND SETUP

After assembling the thruster, the nozzle is closed with a threaded steel cap with Teflon tape to ensure leak tightness. Consequently, the thruster system is fully closed except for unwanted leaks.

For leak finding, a soapy fluid (Electrolube DDF) is available in the cleanroom. If there is a leak where applied, bubbles are visibly formed. It is useful to locate leaks but can not be used to quantify leak rates. Thus, mainly used in the exploratory testing phase to identify leaks to possibly repair them.

To quantify the mass flow leak rate, two different methods are used: the mass flow sensor method and the differential pressure method [45]. These have been taken from the work of Hutten [45]. The first method measures the leak rate directly with the mass flow sensor. When the feed system is opened and the thruster's pressure is kept constant, the mass flow sensor reading is equal to the leak rate due to mass conservation. On the other hand, the differential pressure method takes advantage of the ideal gas theory assuming constant temperature:

$$\dot{m}_{Leak} = \dot{p}_s \frac{V_s}{RT}, \tag{7.6}$$

where $\dot{m}_{Leak}$ is the leakage rate, $\dot{p}_s$ is the change in thruster system's pressure, V_s is the volume of the closed system, R is the specific gas constant and T is the gas temperature.

Both methods have their advantages and disadvantages. Unlike the second method, the main advantages of the mass flow sensor method are that the leak rate is measured directly and it does not depend on any volume estimates. However, the first method only allows leak rate measurement for one pressure value at a time while the differential method determines it for a range of values in one go. Additionally, each method depends on the accuracy of their sensors. For example, Hutten was unable to perform the mass flow sensor method due to the leak rate being lower than the accuracy of the sensor [45].

Since both methods could be performed with the same setup, it was decided to perform the two simultaneously in the same test run.

7.2.2. EXPLORATORY TESTING

In the exploratory testing, several leaks were found. First, every threaded connection between two pieces was a clear leakage point. Consequently, silver soldering was done in stainless steel and steel connections and Teflon tap was applied in the threads related to the RAC. Additionally, the thermowell connection was not leak-tight (Fig. 7.5b) and was closed by applying an available fire sealant paste. The RAC itself exhibited a leak between the inner cylinder and its cap (Fig. 7.5a). This was undeniably unexpected since it had been welded together. No fix was performed on this leak since the fire sealant did not work and was the only readily available option.

Regarding the mass flow sensor method, it was found that the leak mass flow rate could be detected by using the Brooks 5850S Smart Mass Flow. Therefore, it was also performed.

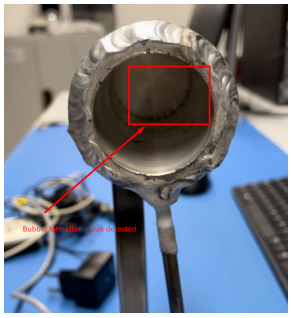

(a) Inner RAC leakage area - bubble formation

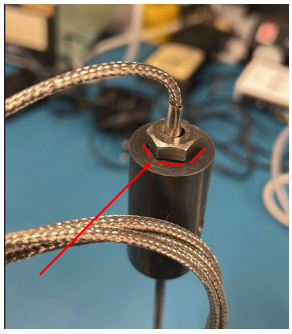

(b) Thermowell leakage area

Figure 7.5: Leaks detected during exploratory testing - red areas

7.2.3. RESULTS AND DISCUSSION

The transient results of the final leak test are shown in Fig. 7.6. As can be seen, five depressurization runs were performed at different starting and ending pressures. In ad-

dition, the mass flow leak rate was measured at six different pressures. The ambient pressure was measured with one of the pressure sensors and it had a constant value of 1.066 bar.

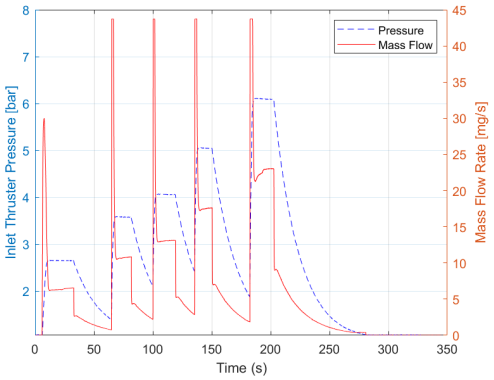

Figure 7.6: Leak testing pressure and mass flow results - p_a = 1.066 bar

Every time the selection valve is opened, the mass flow sensor registers a peak reading. This is expected since the high mass flow is the result of the huge pressure difference between the thruster's pressure and the feed system's pressure. After that initial period, the mass flow stabilizes as well as the inlet pressure. Whenever the valve is closed, the pressure starts dropping as expected. The mass flow reading also instantly drops since it is now reading the gas leaving the section between the valve and the mass flow meter. This is not the leak rate mass flow since that section is also losing pressure. Moreover, the mass flow leak rate increases with the increased system pressure which is expected. Consequently, from a qualitative point of view, the results make sense.

Table 7.3: Mass flow sensor method results

Interval	1	2	3	4	5	6
Mass Flow [mg/s]	0.00	6.46	10.71	13.07	17.48	23.00
Abs. Pressure [bar]	1.07	2.65	3.58	4.06	5.05	6.10

The results for the mass flow sensor method are shown in table 7.3. Six different pressure values were tested and their mass flow readings were measured. Next, the gathered data was fitted into a first-order and a second-order polynomial:

$$\dot{m}_{\text{Leak}} = 0.1257\Delta p^2 + 3.9322\Delta p - 0.006, \quad R^2 = 0.9998, \tag{7.7}$$

$$\dot{m}_{\text{Leak}} = 4.5623\Delta p - 0.4626, \quad R^2 = 0.9977, \tag{7.8}$$

where Δp is the difference between the system pressure and ambient pressure in bar. Although both fits exhibit a good relation with the data, the second-order fit has an un-

deniably closer leak rate to zero when the pressure difference is null which is expected. Thus, the second-order fit is chosen.

Regarding the differential pressure method, the volume needs to be determined. The thruster's volume is 16.84 mm^3 and was obtained from the CAD model and double-checked by hand calculations. However, a section of the feed system is also within the pressurized testing volume and that section had to be estimated since there was no rigorous information about the internal structure's dimensions. This volume is estimated to be 62.01 mm^3. Therefore, V_s is taken as 78.85 mm^3.

Five depressurization runs were done at different starting and ending pressures. In theory, they should overlap and this is verified in all except the first one. A possibility is that the leak increased with the first pressurization. Due to noise, the pressure data was filtered with a low-pass filter of ten readings (equal to one second at a 10 Hz frequency). Next, the pressure derivative was calculated with a finite difference method. Then the data was fitted to a linear relationship to obtain the mass flow leak rate function. Of all the runs, the one with the best fit is the last one which has the highest number of points since it started at the highest pressure and depressurized completely:

$$\dot{m}_{\text{Leak}} = 4.4211\Delta p - 0.4974, \quad R^2 = 0.9880. \tag{7.9}$$

The other 3 runs with similar behaviour also had a linear coefficient between 4.3 and 4.4 mg/s/bar. Comparing this regression to the mass flow sensor one, they are similar and the difference probably derives from the volume estimation process. To get the same linear relationship, the volume would have to be 81.37 mm^3 instead of the estimated 78.85 mm^3 which is not far off. The second-order fit is not similar to the previous method and the y-intercept is as far from zero as the first-order regression.

Due to its undeniably close fit to the data, the y-intercept being close to zero, and the no use of a volume estimation, the second-order fit obtained from the mass flow sensor method is used to estimate the mass flow leak rate. The main leakage source is regarded as the RAC inner cylinder weld.

The results obtained from the final leak testing indicate an estimated mass flow leak rate ranging from 7% to 8.5% when the chamber pressure is maintained at 3 and 6 bar, respectively, with a chocked nozzle with 0.5 diameter throat. While the observed mass flow leak rate appears relatively high compared to the findings and acceptable criteria of previous works, it does not warrant the cancellation of cold flow testing. This leakage can be factored into the theoretical predictions, ensuring that subsequent analyses account for its influence on system performance.

7.3. CONCLUSIONS AND RECOMMENDATIONS

In this section, the conclusions for both preliminary tests are presented. Moreover, recommendations for better results and practices are given. First, the thrust measurement calibration is treated, followed by the leak testing.

THRUST MEASUREMENT CALIBRATION

Regarding the load cell calibration, its calibration is a rather simple process and the results were irrefutably positive. The only recommendation is to build better vertical sup-

port for the load cell as it would easily suffer position changes (thus, changing the voltage offset) if the user was not careful enough. The datasheet shows a cylindrical support with an M3 thread that would achieve this purpose.

The test bench calibration was a harder process due to the coil's behaviour and the stability of the load cell. Nevertheless, despite the noise captured by the load cell, good linear trends were consistently captured, allowing for a successful calibration. Tapping down all wires and building a stable load cell support was fundamental to achieving consistent and repeatable results. Also, the return to the same zero-load voltage after the calibration runs is crucial to the calibration process. If it does not occur, it means that the system is not stable and the reason should be found and fixed.

Regarding recommendations, there are several. An alternative to the VTDC such as a pulley system with known weights attached would be useful for calibrations. This alternative would remove the uncertainties caused by the VTDC heating and misplacement. However, it would only be useful for tests outside the vacuum oven so another possibility that could also cover all scenarios would be best. Moreover, improvements to the current VTDC model could be made: replacing the mounting structure since the current shows melting signals from overheating and creating a mechanism/procedure to assist with the magnet. Lastly, changing the distances to the centre of the load cell, thruster and coil could allow for an approximation of the magnitude of the expected thrust and the coil force, increasing the calibration results extrapolation between the coil and thruster.

LEAK TESTING

The leak testing allowed us to identify the mass flow leak rate of the system by performing both methods described. Qualitatively, the results made are according to the expectations. Regarding the numerical results, the mass flow sensor method result was chosen due to its close fit to the data, null intercept and no volume estimate dependency. Nevertheless, the linear fit of the differential pressure method is close to the other method. Moreover, the method showed repeatability. If the first method was not possible, more depressurization runs would be needed. Consequently, despite the not small leak value, the leak testing was successful.

From the leak testing experience acquired from this work, some recommendations are given.

First, reducing the components' connection complexity is desirable. The choice of aluminium for the RAC in this work posed challenges in achieving leak-tight connections, particularly with steel components. Only Teflon tape proved effective in ensuring leak-proof connections and it is not a solution for laser tests due to its vulnerability at higher operating temperatures. Welding aluminium also presented difficulties and even resulted in the biggest leak. Moving forward, future laboratory models should prioritize materials that enable soldering or straightforward welding for seamless component connections, enhancing overall system integrity.

Additionally, incorporating an extra valve between the thruster and feed systems is recommended to facilitate more accurate volume estimation. However, this adjustment should only take precedence if the mass flow sensor's accuracy restricts that method's use.

These changes would lead to a leak tighter thruster as well as better estimates with

the differential pressure method.

8

NITROGEN TESTING

It is relevant to have experimental data regarding cold flow testing to compare to the hot flow scenario. Without it, it is not possible to attribute unexpected results solely to the propellant heating process as these differences might be caused by other factors such as defective components. By executing a cold flow test, the characteristics of the thruster without heating are determined and can be then compared to the hot flow test, allowing for more substantiated conclusions.

In this chapter, the cold flow testing with nitrogen performed is described. First, the experimental approach is described. Here the test goals, success criteria, controlled variables the measured variables and their range are stated. Next, the test data is treated. For example, the chamber pressure is estimated with the experimental data. Then, the test results are presented followed by their analysis and comparison to the expected performance. Finally, conclusions are drawn and recommendations are given. For the detailed test execution, refer to the appendix H.

8.1. EXPERIMENTAL APPROACH

For this test, the thruster is set up on the test bench and connected to the previously mentioned instrumentation (Fig. 8.1). The propulsion system will have fluid going through without any heating. The nitrogen feed system valve is opened manually at a predefined pressure, allowing flow to enter the thruster. This valve is not closed until all the measured parameters achieve constant values. This has been found to require approximately 30 seconds and the process is repeated five times for the same pressure to study repeatability.

Calibration of the test bench has been performed previously to calculate the produced thrust from the measured load. Also, leak testing has been done to adjust the measured mass flow to the one that escapes the nozzle. The mass flow sensor is switched from the 5805S to the 5851 due to the need for a higher range.

The test objective is to gather data and analyze the system performance without any propellant temperature increase. The performance is compared to ideal rocket theory

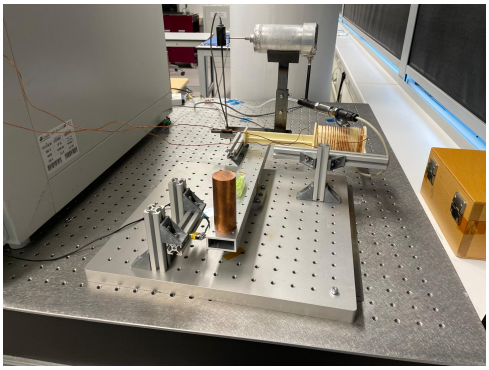

Figure 8.1: Test bench with the thruster connected to its instrumentation on.

and the developed model from Takken [11]. If a hot flow test were to be performed, then the data would be used for further comparison to the propellant temperature increase case. However, since the laser facility is not accessible, that is not possible in this thesis.

Table 8.1: Nitrogen testing measured parameters

Parameter	Description	Location
$\dot{m}$	Propellant mass flow	At the feed system's end
p_i	Inlet pressure	In the inlet connection piece
p_a	Ambient pressure	Cleanroom
T_c	Propellant temperature	Thermowell connection piece
F_{LSB200}	Measured Thrust	Load cell at the other side of the beam

The parameters to be measured and their respective measurement locations are listed in table 8.1. By collecting these, the experimental thrust can be determined as well as the theoretical predictions such as theoretical thrust and mass flow, allowing for comparison with reality. The ambient pressure p_a is measured by the pressure sensor before and is assumed to stay constant during testing. This is considered valid since the testing takes less than an hour, the ambient pressure reading in the cleanroom has stayed the same for all the exploratory testing, and the inlet pressure reading during testing after closing the valve reaches the same value. Regarding the chamber pressure, since unfortunately the pipe got clogged, measuring it is not possible. Thus, an estimate will be performed.

Table 8.2: Nitrogen testing experiment sets and expected values, p_a = 1.066 bar and T_c = 15°C

Test ID	NT-1	NT-2	NT-3	NT-4
p_i [bar]	3	4	5	6
Δp [bar]	0.35	0.42	0.49	0.55
p_c [bar]	2.65	3.58	4.51	5.45
$\dot{m}$ [mg/s]	121.8	164.6	207.3	250.6
F [mN]	45.0	68.2	91.3	114.7
I_{sp} [s]	37.7	42.2	44.9	46.7

The four sets of experiments that will be carried out with nitrogen are shown in table 8.2. Additionally, the expected values for chamber pressure, mass flow and thrust are presented. The pressure drop is estimated as described in section 8.3.1 and the chamber pressure is predicted to allow for nozzle choking. The mass flow is determined by the critical mass flow formula and subtracting the expected mass flow leakage as determined in the previous chapter. Thrust and specific impulse follow from these parameters.

For a schematic of the test setup, refer to Fig. 6.6 of Chapter 6. The only independent variable is the inlet pressure which can be adjusted in the feed system. The chamber temperature is only influenced externally by the ambient temperature and the mass flow sensor is in read-only mode.

The criteria to consider an experiment's data meaningful is described in table 8.3. It is mainly related to the precise measurement of the parameters at hand. These have been inspired by the work of Hutten [45]. The term "constant" means variations lower than 5% in the filtered measurements (due to noise, for example, with the load cell measurements).

Table 8.3: Acceptance criteria for nitrogen testing

ID	Description
AC-01	All parameters (except p_a) from the table 8.1 are measured over time through their respective sensors.
AC-02	The measured chamber temperature remains constant during operation.
AC-03	The measured inlet pressure remains constant during operation.
AC-03a	The averaged inlet pressure is within 5% of the target.
AC-04	The measured mass flow remains constant during operation.
AC-05	The measured thrust remains constant during operation.
AC-06	The exhaust is choked at the nozzle.

Before testing, predictions regarding the results are made to ensure that the outcomes during testing are logical and expected. Regarding the temperature, since no heating is performed, small variations are expected and might not even be effectively captured due to the thermocouple's low resolution. With the inlet pressure increased, it is expected that the measured mass flow and, consequently, the measured thrust increase throughout the testing.

Besides having five consecutive test runs at the same pressure, repeatability could be more extensively tested by performing, for example, a second run after dismantling and reassembling the whole experimental set-up. This was not performed due to time constraints and after the first run, the author tried to fix the clogged section, altering slightly the thruster. A small opening in the clogged part was managed by applying a rust remover solution but not enough to succeed (with a 5 bar system pressure, the reading of the chamber pressure only went from 1 to 1.3 bar).

8.2. TEST RESULTS

During testing, the gathered data appeared to act as expected and the overall experience went without any mishaps. It took around half an hour to perform the experiments after setting up the thruster and the instrumentation, which took around another half an hour, totalling an entire hour of work. The author was not bothered inside the cleanroom but there was some movement in the floor's corridor which is adjacent to the cleanroom. In Fig. 8.2, the plot results from the NT-3 experiment run are shown. All four experiments have the same plots qualitatively and, thus, the others are shown in the appendix I.

Regarding the mass flow plot (Fig. 8.2a), it exhibits a similar behaviour to the leak testing. An initial peak after opening the valve is observed due to a significant pressure difference which then attenuates into a constant value as the pressure difference reduces. After closing the valve, the depressurization occurs faster than the leak testing since the system is not closed. The inlet pressure shifts from ambient to set pressure based on the valve's status (Fig. 8.2b). The values stay undeniably constant. On the other hand, the temperature does not change with the propellant flow, staying around the ambient temperature (Fig. 8.2c). This has been previously explained as an expectation. The load cell output exhibits similar behaviour to the inlet pressure plot but with a higher noise (fig. 8.2d). Thus, a low-pass filter is used to smooth the graph and a constant load behaviour can be seen. After each thrust period, the no-load voltage returns to the same level, confirming that the load cell is adequately fixed and steady. Considering the acceptance criteria, only the choked nozzle (AC-02) can not be verified from the plots but will be verified next by comparing the ratio between the mass flow and the chamber pressure throughout the tests.

The experimental data reveals a commendable level of repeatability across all trials. Consistency in mass flows, pressure, and load cell readings was evident throughout the five runs for each experimental set. Such repeatability is crucial in experimentation, signifying the reliability and precision of our procedures. It instils confidence in the credibility of our findings and underscores the robustness of our methodology.

The measured values for each parameter are averaged out during the thrust periods. The interval being averaged depends on the parameter. For example, for the mass flow, only the last 10 seconds are averaged out since it is converging to a value and the initial seconds would affect the actual mass flow. Regarding the others, the interval values are adjusted to not contain the transition zones.

The only value of interest to average during the no-thrust periods is the load cell voltage output. This is used to assess how the non-zero voltage fluctuates throughout the experiment and to compute the difference to the subsequent thrust voltage zone, thereby determining the generated thrust. As mentioned, it was verified that the no-

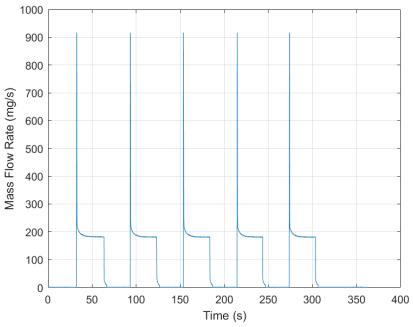

(a) Mass flow

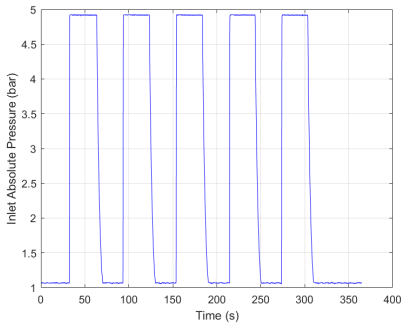

(b) Absolut Inlet Pressure

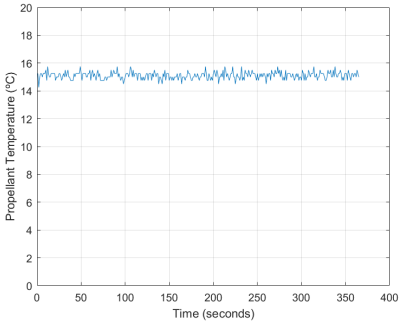

(c) Temperature

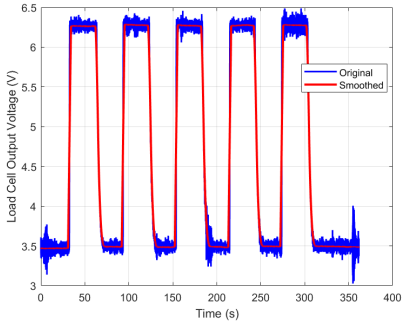

(d) Load Cell Output Voltage

Figure 8.2: NT-3 Results

8

load voltage remained fairly at the same level throughout the same experiment. The NT-1 no-thrust average voltage is 3.466 V while the NT-4 is 3.501 V which is roughly a 1% difference. In addition to it being a small difference, since the thrusts are calculated from the difference between the consecutive voltages of no-thrust and thrust periods, the effect of the change in no-load is even smaller.

Table 8.4: Nitrogen testing averaged results and standard deviation, p_a = 1.066 bar for all

ID	$\dot{m}$ [mg/s]	p_i [bar]	T_p [ºC]	F_{exp} [mN]
NT-1	104.6 ± 0.6	2.95 ± 0.05	14.99 ± 0.25	26.44 ± 1.62
NT-2	143.1 ± 0.8	3.93 ± 0.05	14.92 ± 0.25	44.04 ± 1.56
NT-3	181.3 ± 1.0	4.92 ± 0.05	15.11 ± 0.26	62.50 ± 1.64
NT-4	221.7 ± 1.1	5.97 ± 0.05	15.02 ± 0.25	82.34 ± 1.72

In table 8.4, the averaged results of each experiment and their standard deviations are presented. The uncertainty is calculated by considering the instrument's uncertainty and the data's statistical uncertainty. For example, the statistical uncertainty of the mass

flow is always 0.3 mg/s but the mass flow sensor has a 0.5% rate measuring uncertainty and, thus, the uncertainty is higher for higher mass flow values. For the temperature, only the statistical uncertainty is used since no information regarding its measurement uncertainty is given. Concerning the thrust, its uncertainty derives from the statistical component as well as all the error propagation from the previous chapter's thrust calibration segment.

The absolute inlet pressure is within the acceptance criteria but always lower than the goal. Its standard deviation is undeniably low. Regarding the mass flow sensor reading, this increases along the experiments which is expected due to the higher pressure and insignificant temperature change. Its standard deviation stays in the same range and, therefore, is probably induced by the sensor's accuracy. The experimental thrust F_{exp}, calculated with the relationships developed in Chapter 7, also increases as expected. Its standard deviation stays in the same order of magnitude and is the consequence of the already-mentioned noise. The temperature shows no considerable mean variation throughout the whole testing process and the standard deviation is around the instrument's resolution. Lastly, the ambient pressure does not suffer alterations.

8.3. DATA ELABORATION

In this section, from the experimental data, calculations required to interpret the acquired results are performed. First, the pressure drop is estimated considering the experimental inlet pressure and mass flow. Thus, a more accurate chamber pressure value can be obtained. Lastly, the experimental mass flow result is adjusted considering the mass flow leakage.

8.3.1. PRESSURE DROP ESTIMATION

Before calculating theoretical values, it is necessary to determine the chamber pressure. This parameter is fundamental in the calculation of any nozzle performance model. Due to its importance, the system was designed to measure it, however, as mentioned, the pipe which connected the chamber to the pressure sensor got clogged. Thus, the chamber pressure is estimated by calculating the nitrogen pressure drop after the inlet pressure measurement location.

Due to the complex inner geometry of the thruster, it is not possible to theoretically calculate the pressure drop. Similar situations require the use of CFD to accurately calculate it. Consequently, the pressure drop estimation takes into account only the sections in which the fluid flows through a straight pipe. Pressure losses due to, for example, area expansion and contraction and bends are, therefore, not considered, making the estimation a minimal pressure drop value.

There are four sections where the fluid flows in a straight pipe. The first is the straight connection between the inlet connection piece and the RAC, right after the inlet pressure measurement: 3.3 mm diameter and 7 cm length. The RAC ducts are the second part: 8 rectangular 1x0.5 mm ducts with 8 cm. The last two are the two stainless steel pipe sections: the one after the RAC and the one after the thermowell connection piece: 1 mm diameter and 25 cm length section. The segment inside the thermowell connection piece that connects the two stainless steel pipe parts is not considered due to its

relatively small length and high diameter, and due to its 90º bend, the fluid does not act exactly like inside a straight pipe.

For each test run, the pressure losses in the four sections are calculated according to the equations in the appendix E. The mass flow used is the adjusted mass flow (measured mass flow minus leak rate) and the density is obtained from the NIST Webbook considering the pressure and temperature.

Table 8.5: Pressure drop estimate for each test

Test ID	**NT-1**	**NT-2**	**NT-3**	**NT-4**
p_i [bar]	2.95	3.93	4.92	5.97
Δp_{est} [bar]	0.24	0.29	0.34	0.38
p_c [bar]	2.71	3.64	4.58	5.59

Table 8.5 shows the calculated pressure drop for each test and consequent chamber pressure estimation. The highest contributors to the pressure drop are the stainless steel pipe sections due to their small diameter, resulting in higher velocities. The pressure drop increases along the tests which is expected due to the higher mass flows and, consequent, flow velocity. In addition, the chamber pressure is higher than 2 bar which is the required pressure for nitrogen to achieve a sonic flow in the throat [5]. Consequently, the AC-06 criteria of a choked nozzle is satisfied as long as the actual pressure drop is significantly larger. Nevertheless, the AC-06 criteria can be checked by determining if the ratio between the mass flow passing the throat and the chamber pressure remains the same. This is checked in the next section.

8.3.2. MASS FLOW ADJUSTMENT

The mass flow going through the nozzle is a crucial parameter to determine the theoretical thrust according to IRT. However, the experimental mass flow data does not consider the leak rate and, therefore, that calculation needs to be performed before discussing the results.

Table 8.6: Experimental mass flow adjustment

ID	$\dot{m}_{exp}$ [mg/s]	$\dot{m}_{leak}$ [mg/s]	$\dot{m}_{adj}$ [mg/s]
NT-1	104.6	7.9	96.8
NT-2	143.1	12.3	130.9
NT-3	181.3	17.0	164.3
NT-4	221.7	22.3	199.4

In table 8.6, the calculation process of the mass flow that arrives at the nozzle is presented. The experimental mass flow is the one measured by the sensor, the leak rate mass flow is the mass flow that escapes the system which is calculated by the previously experimentally established relationship (Section 7.2), and the adjusted mass flow is the result of subtracting the leak rate to the experimental and is the one considered to arrive at the nozzle.

With the chamber pressure estimated and the adjusted mass flow, it is possible now to investigate and discuss the obtained results.

8.4. DISCUSSION

In this section, the experimental results shown previously are analysed. First, the system's pressure drop is estimated initially to determine the chamber pressure. With the chamber pressure estimation, the theoretical parameters are calculated according to the ideal rocket theory and compared to the experimental. Their difference is justified by findings in the literature. Lastly, the results are compared to Takken's model predictions.

8.4.1. DISCHARGE COEFFICIENT

Now with the chamber pressure estimated, theoretical values such as theoretical mass flow can be calculated. Consequently, one of the nozzle quality factors, the discharge coefficient C_D, can be calculated by comparison to the experimental. The discharge coefficient is a relevant part of the thruster as it limits the mass flow and if known allows for an improvement of the estimation tool.

Table 8.7: Theoretical and experimental mass flows

ID	$Re_{t,\text{exp}}$ [10^4]	$\dot{m}_{adj}$ [mg/s]	$\dot{m}_{th}$ [mg/s]	$C_{D,\ IRT}$	$C_{D,\text{Takken}}$
NT-1	1.64	96.8	124.7	0.776	0.9711
NT-2	2.22	130.9	167.2	0.783	0.9752
NT-3	2.78	164.3	210.8	0.780	0.9779
NT-4	3.38	199.4	257.2	0.775	0.9798

In table 8.7, the mass flows relevant to the result analysis, the experimental Reynolds number at the throat and the discharge coefficients are presented. The Reynolds number at the throat is calculated with the adjusted experimental mass flow and the nitrogen's viscosity at the local theoretical pressure and temperature. Two discharge coefficients are presented: $C_{D,\ IRT}$ is calculated by the ratio between the adjusted mass flow and the ideal rocket theory prediction and $C_{D,\text{Takken}}$ is the one obtained from Takken's tool (Chapter 2).

The discharge coefficient is correlated to the throat Reynolds number. At low Reynolds numbers ($Re_t < 10^5$), the flow in the rocket motor becomes highly laminar, creating a thick boundary layer in the nozzle throat and causing partial flow blockage [5]. As a result, this blockage leads to a reduction in the actual mass flow compared to the theoretical value. The experimental throat Reynolds numbers are within the low Reynolds range and, thus, the discharge coefficient is not expected to be unitary.

Before analysing the discharge coefficient, it is relevant to notice that the ratio between $\dot{m}_{adj}$ and p_c is roughly the same for the 4 experiments. This would not be the case if the flow was not choked at the nozzle. In fact, in the preliminary testing, a run with an inlet pressure of 2 bar (no choked nozzle) was conducted and the ratio was 15% lower than the ones in the documented experiments. Consequently, the AC-06 criteria (choked nozzle) is satisfied.

From the table 8.7 data, the nozzle's discharge coefficient remains in the 0.77-0.79 range throughout the experiments. From the literature, the discharge coefficients in the nozzle are typically in the 0.9-1.0 range [5]. However, these values are typically from nozzles with smooth converging sections and rounded nozzle throats which are known to have a better performance as they avoid flow detachment [47]. For example, the value predicted by Takken's tool [11] is between 0.97 and 0.98 and uses a relation developed by Johnson [48] and their nozzle is shown in Fig. 8.3.

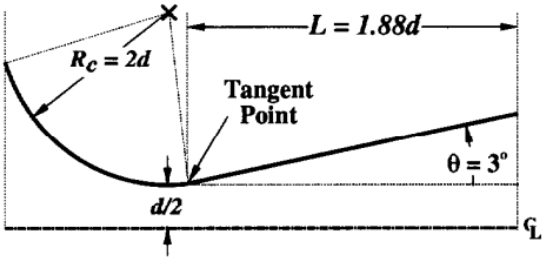

Figure 8.3: Schematic of critical nozzle geometry studied by Johnson [48]

This thruster's nozzle has been manufactured with a manual lathe by the author, leading to a straight-cut throat (no rounding of any kind) and a rough surface converging section with 70º half-angle, significantly higher than the typical 30-45º [47]. Consequently, the performance of the nozzle is expected to be more similar to what is known in the literature as an injector or orifice plate - which regularly presents values in the 0.8-0.9 range. The nozzle manufactured does not belong in the smooth and rounded converging nozzle class from which the relationship used by Takken derives. The difference between the experimental discharge coefficient and the one derived from Takken's tool is, thus, justified.

From the literature regarding orifice plates' discharge coefficient, interesting behaviours are found which are succinctly described below. For a more detailed discussion refer to Appendix J.

As the throat length-diameter ratio increases, the discharge coefficient becomes more invariant regarding chamber pressure with the lower pressure difference between the chamber and the pressure values approaching the choked nozzle behaviour [49] [50]. Also, the higher the contraction ratio from the chamber to the throat, the lower the discharge coefficient [49].

Also, for Reynolds numbers above 10^4, the discharge coefficient shows no dependency on it [50], which is the experimental situation of this thesis.

Zandbergen [5] presents a way to calculate the discharge coefficient for injectors and in this case yields a value of 0.82 which is not far off of 0.78-0.79 experimental value obtained. Moreover, the discharge coefficient is higher than the estimated since the estimated pressure drop is a minimum value, possibly being closer to the 0.82 result. Despite this method being for incompressible flow, for thick orifices (high length-diameter throat ratio) the incompressible flow discharge coefficient is similar to the compressible

case according to the data in the literature. Thus, this estimation method provided by Zandbergen appears suitable for a discharge coefficient prediction and is within a 5% range from the experimental result.

8.4.2. NOZZLE FLOW QUALITY

The other quality factor at play is the nozzle flow quality, ξ_n, which is related to the thrust coefficient C_F:

$$\xi_n = \frac{C_{F,\,exp}}{C_{F,\,th}}. \tag{8.1}$$

In this case, this correction factor can be interchanged with the specific impulse quality ξ_S since there is no combustion or heating ($\xi_c = 1$) [5]:

$$\xi_S = \frac{I_{sp,\,exp}}{I_{sp,\,th}} = \xi_n \xi_c = \xi_n. \tag{8.2}$$

Consequently, it can be calculated with the following relationship:

$$F_{exp} = \dot{m}_{adj} I_{sp,\,exp} g_0 = C_D \dot{m}_{th} \xi_s I_{sp,\,th} g_0 = C_D \xi_s F_{th}. \tag{8.3}$$

Table 8.8 shows the nozzle flow quality values for each test experiment. From the data, the nozzle flow quality increases with the chamber pressure from 0.74 to 0.90.

Table 8.8: Nozzle flow quality $\xi_{I_{sp}}$ for the different tests

ID	NT-1	NT-2	NT-3	NT-4
$\xi_{I_{sp}}$	0.73	0.81	0.86	0.90

In the literature, the nozzle flow quality is usually related to the divergent part of the nozzles where boundary layers form or the flow does not only have an axial velocity component [5]. However, in this case, the nozzle only has a converging section and, thus, the commonly used explanations can not be applied. Unfortunately, no relevant information about the nozzle flow quality in orifices and injectors was found.

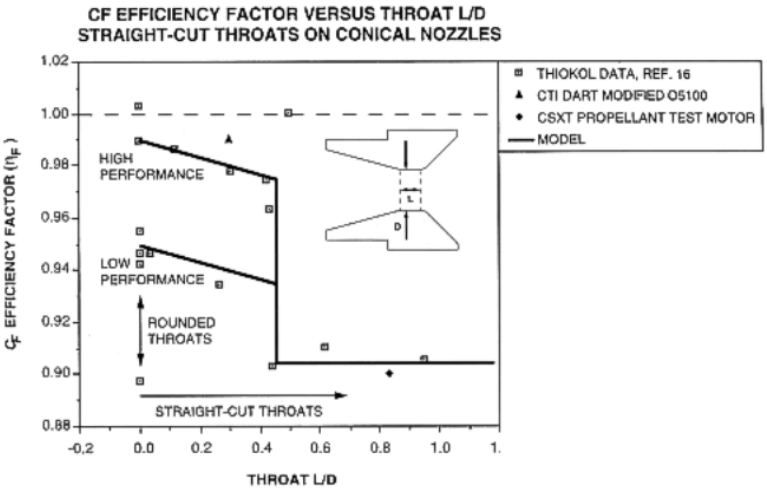

Figure 8.4: [47]

Nevertheless, Rogers [47] investigated the effect of the length-diameter ratio of straight-cut throats (Fig. 8.4). From the graph, L/D ratios above 0.4 have nozzle flow quality factors around 0.9 which is the maximum value obtained in this experiment.

A possible explanation for the increase in the nozzle flow quality might be related to the throat Reynolds number. Although it has been verified in the literature that it does not affect the discharge coefficient, it might affect the nozzle flow quality. The higher Reynolds number might result in a lower boundary layer formation after the flow reattaches in the nozzle throat which would result in higher velocities and, thus, higher specific impulse. However, this possibility needs to be taken cautiously as it is merely a hypothesis not based on the literature. In addition, the Reynolds number only doubles from the first to the fourth test which is not a significant change to cause such a difference in specific impulse quality.

Another possibility is related to the thrust bench calibration. The thrust bench was calibrated using the VTDC which is limited to around 12 mN and the measured thrust goes up to 82.3 mN. There could be the case that at higher force values the effect of the thruster on the bench and its wires changes and no longer restricts the rotation of the beam. Consequently, the produced thrust could be overestimated and, thus, the higher specific impulse qualities appear.

8.5. CONCLUSION AND RECOMMENDATIONS

In this chapter, we introduced the experimental procedure with clarity and conciseness, detailing the parameters to be measured, the independent variables and their planned testing, as well as the acceptance criteria for a successful test. The subsequent section presented the test results, including plots of the four datasets, which were commented on qualitatively. The data qualitatively corroborated the expected outcomes.

In the discussion of the results, the pressure drop was estimated, and the choked flow

in the nozzle was confirmed for the four inlet pressure values. However, the discharge coefficient was found to be lower than anticipated. The constant value for this coefficient throughout the experiments can be justified by experimental results for thick orifices in the literature. Moreover, the compressible discharge coefficient theory for thick orifices does not align with the experimental data, suggesting that for thick orifices, a discharge coefficient estimate considering incompressible flow might be appropriate.

Regarding the nozzle flow quality, it was noted that its value increases with pressure, but there is a lack of information on this topic in the literature, particularly for orifices. However, it appears that the throat length-to-diameter ratio plays a significant role, as indicated by the literature. A possible explanation for the variation in nozzle flow quality could be related to the Reynolds number and boundary layer formation or the fact that the thrust bench calibration does not cover the entire thrust range and, thus, overestimates the measured thrust.

Several recommendations can be made based on the findings of this experimental work:

- **Chamber Pressure Measurement:**
  - It is recommended to measure the pressure directly in the chamber to avoid the need for estimations. Thus, using, for example, stainless steel could avoid the clogging.
- **Nozzle Design Change**
  - The nozzle design could be changed to allow for a tube with a bigger inner diameter for the chamber pressure measurement. This would make clogging less likely.
- **Thrust Bench Calibration:**
  - Modify the thrust bench calibration method to ensure it covers the entire range of thrust measurements. This will provide more accurate and comprehensive data.
- **Nozzle Manufacturing:**
  - Manufacture the nozzle using a CNC machine or consider outsourcing the manufacturing process to avoid rough and high-angle converging sections. This would likely improve the precision and performance of the nozzles.

By implementing these recommendations, future experiments can achieve more accurate results and potentially uncover new insights into the behaviour of nozzles and orifices under various conditions. These steps will also help in addressing some of the inconsistencies and gaps identified in the current experimental setup and results.

9

CONCLUSION

In Section 2.6, the author formulated four distinct research questions derived from identified research gaps in the existing literature. These questions served as the guiding framework for the entirety of this thesis.

The first research question posed was:

Q1 Can the absorption of beam power be accurately modelled within a margin of 5%?

This question was addressed in the initial numerical chapter (Chapter 3). The chapter began with a theoretical exposition essential for comprehending the developed prediction models. Subsequently, three distinct methodologies were introduced. The author successfully developed algorithms that substantially reduced computational time compared to standard ray tracing computations, particularly for the three geometries in diffuse reflections and the cylindrical geometry in specular reflections. These optimized models achieved accuracies in estimating the absorbed power within 1% and operated approximately 20 times faster than the ray tracing method. Consequently, the research question was successfully answered under these specified conditions. Moreover, for the diffuse scenario, information regarding the spatial distribution of absorbed power is also an output, allowing for the development of the FEM model. This was not possible with COMSOL.

The second research question is:

Q2 How do the RAC and duct geometry change affect performance?

To answer this question, several steps were taken. First, in Chapter 3, the effect of geometry was studied regarding the beam power absorption: low aperture ratios, bigger length ratios and lower cone ratios generally led to higher absorption. Then, in Chapter 4, the tools developed to investigate the influence of the geometrical aspects relative to the other heat transfer mechanisms were presented. From them, optimization was also possible and it was the topic of Chapter 5. In this chapter, the influence of length, diameter, surface coating, and duct geometry were extensively studied. There is no straightforward answer to this research question since the impact of each variable varies a lot

case by case. For example, the influence of length and diameter in the equilibrium temperature depends on the surface coating ratio and the duct geometry depends on the propellant flow regime.

The third research question is regarding the possible efficiency values:

Q3 What overall RAC efficiency values can be achieved?

Needless to say, the possible values to be achieved depend on the constraints imposed by the mission requirements. However, by performing optimization in the case study in Chapter 5, some efficiency values are presented. Overall efficiency, in this scenario, ranged from 54% to 71% by simply changing the length from 5 to 10 cm. It was also noticed that it was mainly the absorption efficiency that limited the result and this could easily be improved by choosing a surface coating with a greater α/ε ratio such as black. This change would result in RAC efficiencies above 90% and, therefore, values above 90% are achievable.

The last research question is related to the experimental part of this thesis:

Q4 How does the experimental data relate to the prediction model?

Unfortunately, it was not possible to use the laser facility and, therefore, only cold flow testing of the manufactured was possible. Consequently, only the nozzle prediction tool developed by Takken was compared to the experimental data. The manufacturing process is documented in Chapter 6 and the preliminary testing in Chapter 7. Finally, the nitrogen cold flow testing results and discussion are the topics of Chapter 8.

The tests matched the expectations qualitatively with undeniable repeatability. Regarding numerical values, the prediction model was not successful in predicting the discharge coefficient and the nozzle flow quality factor. However, this discrepancy emerged from the difference in the manufactured nozzle and the nozzles used to determine the correction factors. In fact, relevant literature that justified the experimental discharge coefficient number and behaviour throughout the tests was presented as well as a predictive method for it. On the other hand, the behaviour of the nozzle flow quality could not be explained due to the lack of literature.

From the experience gained throughout this thesis, several recommendations for future work are given and are divided into numerical and experimental work. Concerning numerical development, the main recommendation is to further develop the FEM model by incorporating convective heat transfer and to create a user-friendly tool for it. Regarding experimental work, future laboratory models should have design/material changes that avoid clogging pipes and threaded connections. Moreover, an alternative to the performed thrust bench calibration method to cover higher thrust levels would be valuable to ensure that the relationship between generated and measured thrust is captured for the whole testing range.

To sum up, this thesis work aimed to answer the previously established research questions. The numerical work was able to successfully address the first three questions, demonstrating significant advancements in modelling beam power absorption, understanding the impact of RAC and duct geometry on performance, and identifying potential overall RAC efficiency values. However, the experimental work, despite considerable effort, was unable to fully meet expectations due to limitations in facility access

and manufacturing constraints. These restrictions prevented a comprehensive validation of the prediction models against experimental data. Moreover, at the end of each chapter, recommendations and future work possibilities are presented. These are based on the knowledge and experience gained from this thesis work.

BIBLIOGRAPHY

[1] McGill University. *Spacecraft propulsion*. 2007. URL: https://www.cs.mcgill.ca/~rwest/wikispeedia/wpcd/wp/s/Spacecraft_propulsion.htm (visited on 11/19/2022).

[2] Kim, Eun S., Emdee, Jeffery L., and Cohn, Richard K. "Liquid Propulsion: Historical Overview, Fundamentals, and Classifications of Liquid Rocket Engines". In: *Encyclopedia of Aerospace Engineering*. John Wiley Sons, Ltd, 2010. ISBN: 9780470686652.

[3] Shrivastava, S. K. "Orbital perturbations and stationkeeping of communication satellites". In: *Journal of Spacecraft and Rockets* 15.2 (1978), pp. 67–78.

[4] Gerrish Jr., H. P. *Solar Thermal Propulsion at MSFC*. Propulsion Systems Division Marshall Space Flight Center. Feb. 2016. URL: https://ntrs.nasa.gov/api/citations/20160003173/downloads/20160003173.pdf (visited on 11/2022).

[5] Zandbergen, B.T.C. *AE4-S01 Thermal Rocket Propulsion (version 2.08)*. Aug. 2020.

[6] National Aeronautics and Space Administration (NASA). *The Current State of Deep Space Propulsion: Challenges and Opportunities*. Tech. rep. NASA, 2018. URL: https://ntrs.nasa.gov/api/citations/20180005485/downloads/20180005485.pdf.

[7] NASA. *Dual-mode Propulsion System Enabling CubeSat Exploration of the Solar System*. Tech. rep. NASA, 2014. URL: https://www.nasa.gov/missions/small-satellite-missions/dual-mode-propulsion-system-enabling-cubesat-exploration-of-the-solar-system/.

[8] L., Fiona et al. "Design and characterisation of a bi-modal solar thermal propulsion and power system for small satellites". In: *Applied Thermal Engineering* 189 (2021), p. 116609. ISSN: 1359-4311. DOI: https://doi.org/10.1016/j.applthermaleng.2021.116609. URL: https://www.sciencedirect.com/science/article/pii/S135943112100065X.

[9] D., Emmanuel et al. "Design of a rapid transit to Mars mission using laser-thermal propulsion". In: *Acta Astronautica* 192 (2022), pp. 143–156. ISSN: 0094-5765. DOI: https://doi.org/10.1016/j.actaastro.2021.11.032. URL: https://www.sciencedirect.com/science/article/pii/S0094576521006305.

[10] Leenders, H. C. M. and Zandbergen, B. T. C. "Development of a solar thermal thruster system". In: *59th International Astronautical Congress: IAC 2008, 29 September-3 October 2008, Glasgow, Scotland*. 2008.

[11] Takken, A. *Development of a high temperature Solar Thermal Propulsion engine*. 2021. URL: https://repository.tudelft.nl/record/uuid:e6cc6c72-bcfb-4927-a0bf-d935a6ba32f8.

[12] Gomes, D. *Literature Study - Laser Propulsion System*. 2022. URL: https://github.com/djozao/Thesis.

[13] Das, K. *Design and Thermal Analysis of a Solar Thermal Thruster*. 2018. URL: https://repository.tudelft.nl/record/uuid:089a52d1-8b8f-486e-b17d-8bb73da9bb72.

[14] Takken, A. *Feasibility of Solar Thermal Propulsion Literature Study*. 2019.

[15] Shoji, J. and Larson, V. "Performance and heat transfer characteristics of the laser-heated rocket - A future space transportation system". In: *12th International Electric Propulsion Conference*. DOI: 10.2514/6.1976-1044. eprint: https://arc.aiaa.org/doi/pdf/10.2514/6.1976-1044. URL: https://arc.aiaa.org/doi/abs/10.2514/6.1976-1044.

[16] Sutton, G. P. and Biblarz, O. *Rocket propulsion elements*. John Wiley & Sons, 2016.

[17] Daabo, A. M., Mahmoud, S., and Al-Dadah, R. K. "The effect of receiver geometry on the optical performance of a small-scale solar cavity receiver for parabolic dish applications". In: *Energy* 114 (2016), pp. 513–525. ISSN: 0360-5442. DOI: https://doi.org/10.1016/j.energy.2016.08.025. URL: https://www.sciencedirect.com/science/article/pii/S0360544216311288.

[18] Asselineau, C. A., Zapata, J., and Pye, J. "Geometrical Shape Optimization of a Cavity Receiver Using Coupled Radiative and Hydrodynamic Modeling". In: *Energy Procedia* 69 (2015). International Conference on Concentrating Solar Power and Chemical Energy Systems, SolarPACES 2014, pp. 279–288. ISSN: 1876-6102. DOI: https://doi.org/10.1016/j.egypro.2015.03.032. URL: https://www.sciencedirect.com/science/article/pii/S1876610215003380.

[19] Prakash, M., Kedare, S.B., and Nayak, J.K. "Investigations on heat losses from a solar cavity receiver". In: *Solar Energy* 83.2 (2009), pp. 157–170. ISSN: 0038-092X. DOI: https://doi.org/10.1016/j.solener.2008.07.011. URL: https://www.sciencedirect.com/science/article/pii/S0038092X08001795.

[20] Uhlig, R. et al. "Strategies Enhancing Efficiency of Cavity Receivers". In: *Energy Procedia* 49 (2014). Proceedings of the SolarPACES 2013 International Conference, pp. 538–550. ISSN: 1876-6102. DOI: https://doi.org/10.1016/j.egypro.2014.03.058. URL: https://www.sciencedirect.com/science/article/pii/S1876610214005128.

[21] Larrouturou, F., Caliot, C., and Flamant, G. "Effect of directional dependency of wall reflectivity and incident concentrated solar flux on the efficiency of a cavity solar receiver". In: *Solar Energy* 109 (2014), pp. 153–164. ISSN: 0038-092X. DOI: https://doi.org/10.1016/j.solener.2014.08.028. URL: https://www.sciencedirect.com/science/article/pii/S0038092X14004058.

[22] van Boxtel, T. *AE4S20 Satellite Thermal Control Lecture Notes*. Unpublished. 2021.

[23] Preijde, J. J. *Design of a Solar Thermal Power-Propulsion System for a Small Satellite*. 2015.

[24] Rohsenow, W.M., Hartnett, J.P., and Cho, Y.I. *Handbook of Heat Transfer*. McGraw-Hill handbooks. McGraw-Hill Education, 1998. ISBN: 9780070535558.

[25] Eguchi, K. et al. “Fundamental Experiment of CW Laser Propulsion with Porous Carbon Heat Exchanger”. In: *2018 AIAA Aerospace Sciences Meeting*. 2018, p. 0176.

[26] M., Koichi. “Laser Propulsion Using a Porous Carbon Heat Exchanger”. In: *Journal of Propulsion and Power* 38.5 (2022), pp. 880–883.

[27] Shimizu, M. et al. “Solar thermal thruster made of single crystal molybdenum11Paper IAF-96-S.4.01, presented at the 47th International Astronautical Congress, Beijing, China, 7–11 October 1996.” In: *Acta Astronautica* 41.1 (1997), pp. 23–28. ISSN: 0094-5765. DOI: https://doi.org/10.1016/S0094-5765(97)00200-2. URL: https://www.sciencedirect.com/science/article/pii/S0094576597002002.

[28] Tucker, S. and Salvail, P. “Solar-thermal engine testing”. In: *AIP Conference Proceedings*. Vol. 608. 1. American Institute of Physics. 2002, pp. 486–493.

[29] Juds, S. *Photoelectric Sensors and Controls: Selection and Application, First Edition*. Mechanical Engineering. Taylor & Francis, 1988. ISBN: 9780824778866. URL: https://books.google.nl/books?id=BkdBo1n_oO4C.

[30] Gebhart, B. *Heat Transfer*. McGraw-Hill, 1961.

[31] COMSOL. *Ray Optics Module - User's Guide*. 2018.

[32] Nicodemus, F. E. et al. *Geometrical Considerations and Nomenclature for Reflectance*. NBS Monograph 160. National Bureau of Standards (U.S.), 1977. URL: https://nvlpubs.nist.gov/nistpubs/Legacy/MONO/nbsmonograph160.pdf.

[33] Griot, M. *Guassian Beam Optics*. 2009.

[34] European Space Agency. “Spacecraft thermal-control design data handbook – Volume 1”. In: European Space Agency, 1989.

[35] Chin, J. H., Panczak, T. D., and Fried, L. “Spacecraft thermal modelling”. In: *International Journal for Numerical Methods in Engineering* 35.4 (1992), pp. 641–653. DOI: https://doi.org/10.1002/nme.1620350403. eprint: https://onlinelibrary.wiley.com/doi/pdf/10.1002/nme.1620350403. URL: https://onlinelibrary.wiley.com/doi/abs/10.1002/nme.1620350403.

[36] Lienhard IV, J. H. and Lienhard V, J. H. *A Heat Transfer Textbook*. 5th. Version 5.10. Cambridge, MA: Phlogiston Press, 2020. URL: http://ahtt.mit.edu.

[37] Meseguer, J., Pérez-Grande, I., and Sanz-Andrés, A. *Spacecraft Thermal Control*. Spacecraft Thermal Control. Elsevier Science, 2012. ISBN: 9780857096081. URL: https://books.google.nl/books?id=_dpkAgAAQBAJ.

[38] Sutheesh, P. M. and Chollackal, A. “Thermal performance of multilayer insulation: A review”. In: *IOP Conference Series: Materials Science and Engineering* 396.1 (Aug. 2018), p. 012061. DOI: 10.1088/1757-899X/396/1/012061. URL: https://dx.doi.org/10.1088/1757-899X/396/1/012061.

[39] *SAFFIL M-FIL PRODUCT DATA SHEET*. SAFFIL. URL: http://www.lloyd-ris.co.uk/pdfs/datasheets/SAFFIL%20MFIL%20DATA%20Sheet.pdf.

[40] Ray, S., Loukou, A., and Trimis, D. “Evaluation of heat conduction through truncated conical shells”. In: *International Journal of Thermal Sciences* 57 (2012), pp. 183–191. ISSN: 1290-0729. DOI: https://doi.org/10.1016/j.ijthermalsci.2012.02.004. URL: https://www.sciencedirect.com/science/article/pii/S129007291200049X.

[41] Versteeg, H. *Novel fabrication method for a hot gas supersonic micro-thruster*. 2020. URL: https://repository.tudelft.nl/record/uuid:ac2482ad-0f8e-4569-8bd4-fd11bd6327bd.

[42] Brooks Instrument. *Profibus-DP Interface for use with Brooks® Smart Mass Flow Meters models 5860S, 5861S, 5863S, 5864S Mass Flow Controllers models 5850S, 5851S, 5853S*. 2008.

[43] Santos, S. *Arduino: K-Type Thermocouple with MAX6675 Amplifier*.

[44] Cramer, L. *The advancement of the TU Delft vaporising liquid micro-resistojet design*. 2024. URL: https://repository.tudelft.nl/record/uuid:6c21b8f6-c55a-44e6-86bf-69f99c1e0978.

[45] Hutten, R. *Vaporizing Liquid Micro-resistojet experimentation*. 2021. URL: https://repository.tudelft.nl/record/uuid:960550ce-eb34-4f3d-873a-1f2a6f4763f0.

[46] Bijster, R. *Design, Verification and Validation of a Micropropulsion Thrust Stand*. 2014. URL: https://repository.tudelft.nl/record/uuid:5c3f0eb3-511c-4443-90b2-46eed9a6b184.

[47] Rogers, C. E. “Departures from Ideal Performance for Conical Nozzles and Bell Nozzles, Straight-Cut Throats and Rounded Throats”. In: *High Power Rocketry Magazine* 35.7, 8 (Oct. 2004), pp. 24–54, 14–35. URL: https://rasaero.com/dloads/Departures%20from%20Ideal%20Performance.pdf.

[48] Johnson, A. N. et al. “Numerical characterization of the discharge coefficient in critical nozzles”. In: *NCSL Conference Proceedings, Albuquerque, NM*. 1998, pp. 407–422.

[49] Kayser, J. C. and Shambaugh, R. L. “Discharge coefficients for compressible flow through small-diameter orifices and convergent nozzles”. In: *Chemical Engineering Science* 46.7 (1991), pp. 1697–1711. ISSN: 0009-2509. DOI: https://doi.org/10.1016/0009-2509(91)87017-7. URL: https://www.sciencedirect.com/science/article/pii/0009250991870177.

[50] Deckker, B. E. L. and Chang, Y. F. “Paper 7: An Investigation of Steady Compressible Flow through Thick Orifices”. In: *Proceedings of the Institution of Mechanical Engineers, Conference Proceedings* 180.10 (1965), pp. 312–323. DOI: 10.1243/PIME_CONF_1965_180_307_02. eprint: https://doi.org/10.1243/PIME_CONF_1965_180_307_02. URL: https://doi.org/10.1243/PIME_CONF_1965_180_307_02.

A

RAY TRACING SIMULATIONS

In this chapter, the ray tracing simulations performed in this thesis to determine the total absorption in a cylindrical, conical and concylindrical cavity are presented. First, a guide to recreating the simulation environment in COMSOL is described. Afterwards, justification for the decisions regarding some of the parameters, for example, the number of rays is explained.

Most of the information used to develop this has been taken from the COMSOL Manual for the ray tracing model [1].

A.1. NUMERICAL SIMULATION SETUP

Below the modelling instructions to create the ray-tracing simulation model using COMSOL from scratch are presented.

To sum up, in the "Global Definitions" section, the user defines all the parameters that require changes during the parametric sweep as well as other variables which appear throughout the simulation model, thus, making it easier to change. It is relevant to note that the origin of the beam has been decided in such a way that it fits the aperture. This has been done to decrease the number of input variables since it is probably ideal for the design: a larger aperture would result in lower beam power absorption and higher power loss due to radiation. Next, the user creates the cavity geometry which can be a rectangle, a cone or a mixture of both according to the user input. Next, in "Geometrical Optics", the user creates the beam and defines the previously defined geometry as a wall with a specific absorption and reflection type. Also, ray termination criteria are added: the bounding box is defined in a way such that rays that have left the cavity at some stage are not considered anymore and the power threshold is defined in a way that the sum of the rays terminated by it cannot exceed 0.01 W of power. These termination criteria reduce slightly the computational time and deviate at most 0.01 W, which is 0.01% of the total beam power, from the result without it. The user is guided on how to set up the parametric sweep according to their interests. Moreover, the maximum length and the step size used in the simulations are declared and these will be justified below.

A

After the simulation is done, which might take several hours or even days depending on the number of simulations the user defines in the parametric sweep and its computational power, how to extract the data regarding the total power absorbed, minimum and maximum power density in a form of a table is explained.
Modelling Instructions

From the **File** menu, choose **New**.

NEW

In the **New** window, click **Model Wizard**.

MODELWIZARD

1. In the **Model Wizard** window, click **2D**.
2. In the **Select Physics** tree, select **Optics>Ray Optics>Geometrical Optics (gop)** and click **Add**.
3. Click **Study**.
4. In the **Select Study** tree, select **Preset Studies for Selected Physics Interfaces>Ray Tracing**.
5. Click **Done**.

GLOBALDEFINITIONS
Parameters I

1. Fill in the parameter table with the data structure in table A.1.

Table A.1: Parameter Table

Name	Expression	Value	Description
D	10 [cm]	0.1 m	Diameter
LD	10	10	Length-Diameter Ratio
L	LD*D	1 m	Length
a	AR*D	0.01 m	Aperture
AR	0.1	0.1	Aperture Ratio
CC	0.1	0.1	Cone/Cylinder Ratio
γ	atan((D/(2*CC*L)))	0.46365 rad	Cone Angle
emi	0.1	0.1	Emissivity
α	5	5	Laser Angle
origin	a/(2* tan($\alpha * \pi/180$))	0.05715 m	Laser Origin
N_rays	1000	1000	Number of Rays
P_0	100	100	Laser Power

GEOMETRY

1. In the **Model Builder** window, under **Component 1 (comp1)** click **Geometry 1**.
2. In the **Geometry** toolbar, click **Primitives>Polygon**.
3. In the **Polygon** dialog box, select **Type>Open curve** and fill in the **Coordinates** with the information in table A.2.

Table A.2: Polygon coordinates table

Point	**1**	**2**	**3**	**4**	**5**	**6**	**7**
x (m)	0	0	$L-\frac{D}{2\tan(\gamma)}$	L	$L-\frac{D}{2\tan(\gamma)}$	0	0
y (m)	$a/2$	$D/2$	$D/2$	0	$-D/2$	$-D/2$	$-a/2$

GEOMETRICAL OPTICS (GOP)

1. In the **Model Builder** window, under **Component 1 (comp1)** click **Geometrical Optics (gop)**.
2. In the **Settings** window for **Geometrical Optics**, locate the **Ray Release and Propagation** section and in the **Intensity Computation** box select **Compute power**.

Release from Grid I

1. In the **Physics** toolbar, click **Global** and choose **Release from Grid**.
2. In the **Settings** window for **Release from Grid**, locate the **Initial Coordinates** section.
3. In the $q_{x,0}$ text field, type "-origin", and in the $q_{y,0}$ type "0".
4. Locate the **Ray Direction Vector** section and from the list, choose **Conical**.
5. In the N_θ text field, type "N_rays". In the **Cone Axis** text field, type 1 and 0 for x and y, respectively. In the **Cone Angle** text field, write "alpha*pi/180". From the **Sampling from Distribution** list, choose **Deterministic**.
6. Locate the **Total Source Power** section. Choose **Uniform Distribution** from the **Intensity initialization** and in the P_{src} text field, type "P_0".

Wall I

1. In the **Physics** toolbar, click **Boundaries** and choose **Wall**.
2. In the **Settings** window for **Wall**, locate the **Boundary Selection** section and select **All Boundaries**.
3. Locate the **Wall Condition** section and from the list choose **Specular Reflection**, **Diffuse Reflection** or any other which fits your goal.
4. Locate the **Absorption Coefficient** section and in the **Absorption coefficients** text field type "emi".

A

5. In the **Physics** toolbar, click **Attributes** and choose **Deposited Ray Power**.

Ray Termination

1. In the **Physics** toolbar, click **Global** and choose **Ray Termination**.
2. In the **Termination Criteria** window, select from the list **Bounding box, user defined** and fill the boxes according to table A.3.

Table A.3: Ray termination bounding box criteria

Parameter	x_{min}	x_{max}	y_{min}	y_{max}
Value	$-1.01 \times$ origin	$L \times 1.01$	$-D \times 1.01$	$D \times 1.01$

3. In the **Additional Termination Criteria** part, select **Power** from the list and in the **Threshold Power** type in "0.01/N_rays".

STUDY
Parametric Sweep

1. In the **Study** toolbar, click **Parametric Sweep**.
2. In the **Settings** window for Parametric Sweep, locate the **Study Settings** section and click in the **Add** button.
3. In the table, enter the settings, for example, according to table A.4.

Table A.4: Parametric Sweep Settings

Name	Value	Unit
alpha	range(5, 10, 45)	
emi	range(0.1, 0.1, 1)	
AR	range(0.1, 0.1, 1)	
LD	range(0.5, 0.25, 2.5)	
CC	0 0.1 1	

Step 1: Ray Tracing

1. In the **Study** toolbar, click **Step 1: Ray Tracing**.
2. In the **Study settings** window, select **Specify maximum path** from the **Time-step specification** list and **m** from the **Length unit** list.
3. In the **Lengths** text box, write "range(0,60,60)".
4. In the **Study** toolbar, click **Compute**.

RESULTS

1. In the **Results** toolbar, right-click **Derived values** and select **Integration>Line Integration**
2. In the **Line integration** window, select the respective **Dataset** from your study and choose **Last** from the **Time Selection** list.
3. From the **Selection** list, select **All boundaries**.
4. Locate the **Expressions** table, click **Add Expression** and select **Model>Component 1 (comp1)>Geometrical Optics>Accumulated Variables> Boundary Heat Source** and from the options select **Boundary Heat Source**, **Minimum of accumulated variable** and **Maximum of accumulated variable**.
5. In the **Line integration** window, right-click **Evaluate** and select **New Table**.
6. In the **Table** window, click on **Export** to export the table in the preferred format.

A.2. SIMULATION NUMERICAL PARAMETERS

The results of the simulation depend on the numerical steps the user defines. The relevant aspects for this type of simulation are the number of rays, their maximum path length and the step size.

NUMBER OF RAYS

To define the minimum number of rays N_{rays} needed for the simulations, the maximum path length and its step size, a somewhat interactive method is required. It is important to underline that although accuracy in the result is desired, the computational time required is also an important factor to take into account. To determine these parameters, only a few cases were studied.

First, the minimum number of rays N_{rays} is determined for the specular case. For this, it is relevant to use a maximum path length which is not a limiting factor in the simulation result. The biggest path length a ray can realistically cover is the diagonal of the cylinder with the highest LD, in this case, 10, which makes the diagonal approximately 1.005 meters. Moreover, the lowest emissivity in the simulation range ($\varepsilon = 0.1$) produces the most sensitive result and, therefore, is chosen for these runs. After 100 reflections in a surface with $\varepsilon = 0.1$, a ray's power diminishes to 0.0026% of its initial power. Consequently, setting up the maximum length path to 100.5 meters is enough to isolate N_{rays}. Next, regarding the angle and the aperture ratio, only the extreme cases were considered: 5° and 45°, and 0.1 and 1, respectively. Thus, only 4 scenarios for each geometry are simulated and it was decided to test on both the rectangle and conical geometries.

The results for the study of the minimum N_{rays} in the rectangular cavity with specular reflection are presented in table A.5. The results of the conical cavity are similar in trend. At $N_{rays} = 1$, the results might appear bizarre at first glance but they are equal due to it being only one ray which has $\alpha = 0$ and thus reflects back out the cavity after one reflection. As N_{rays} increases, the accuracy of the result is expected to increase and, thus, the 100k N_{rays} will be used as the real value and the relative errors were calculated. Taking into account the relative errors and t_{sim}, the 1k value has been chosen as its maximum relative error is around 0.23% and the time difference compared to the low N_{rays}

Table A.5: Simulation results and time vs. Number of Rays of rectangular cavity with specular reflection

N_{rays}	1	10	100	1k	5k	10k	100k
$\alpha = 5, AR = 0.1$	10	96.375	78.824	78.289	78.462	78.503	78.475
$\alpha = 5, AR = 1$	10	20.440	19.774	19.691	19.687	19.687	19.687
$\alpha = 45, AR = 0.1$	10	97.775	91.684	92.546	92.675	92.739	92.734
$\alpha = 45, AR = 1$	10	59.766	58.555	58.869	58.866	58.861	58.862
t_{sim} (s)	6	6	6	8	16	27	300

simulations is not as significant, which is relevant because a considerably huge number of simulations are intended.

MAXIMUM PATH LENGTH

Now with N_{rays} determined, the maximum path length can be determined. The inputs are the same as in the previous study and the value chosen will be the lowest which does not change the value from the extreme path case. The scenario with the highest maximum path length required is $\alpha = 5$ and $AR = 0.1$ with 70 meters. Consequently, the maximum path length chosen is 70 meters for the whole simulation. It appears that an increase in path length is not as detrimental to t_{sim} as N_{rays}.

STEP SIZE

Regarding the step size for the simulations, several simulations with different values were used but it seems to have no influence in the simulation results. In fact, COMSOL automatically adjusts the step size throughout the simulation accordingly. However, the step size highly influences the simulation run time. For example, the previous 4 simulations combined take 1 minute with "range(0,0.1,70)" and 8 seconds with "range(0,70,70)". Therefore, one can and should, if interested only in the numerical results, only insert "range(0,70,70)" in the simulation path length text box. Having a smaller step size is only beneficial if the user is interested in the ray tracing plots. The difference in time might be caused by the process of storing the numerous plot images.

REFERENCES

[1] COMSOL. *Ray Optics Module - User's Guide*. 2018.

B

2D Specular Rectangular Algorithm

In this chapter, a developed algorithm to determine the percentage of beam power absorbed by a 2D specular rectangular cavity is described. Since for specular reflections, the beams remain in the same plane, it can also be used for the 3D cylindrical cavity as long as the beam is also axially symmetrical.

B.1. Algorithm

Consider a rectangular cavity with length L, diameter D, aperture size A and absorptivity ε, as well as a beam with a diverging half-angle α_0, origin o and total power P_0. Concerning the rectangular-shaped cavity, there is a smooth property which will allow us to develop the algorithm. Due to it being only composed of horizontal and vertical, the angle of incidence is preserved in such a way that it is always the initial angle α or its supplementary. This allows us to "unfold" the several segments and form a continuous line with the same slope as can be seen in Fig. B.1.

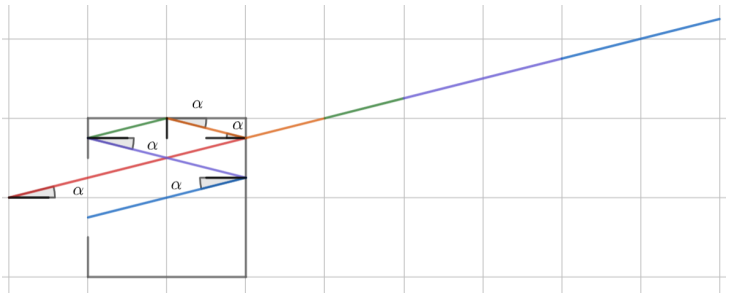

Figure B.1: Specular reflection of a ray with an arbitrary angle inside a rectangular cavity

Consequently, by knowing the horizontal and vertical distance that a ray travels until

it leaves the cavity, it is possible to calculate the angle of such a ray:

$$tan\alpha = \frac{d_y}{d_x}. \tag{B.1}$$

The roughest estimation one could make is to calculate the angle range where the rays only hit the bottom surface and leave through the aperture. This will be denominated as the first-order approximation. It is trivial that the angle of zero is part of such a range due to its null angle of incidence. The upper limit of this range ϕ is:

$$\beta = \arctan \frac{\frac{A}{2}}{2L+o}, \tag{B.2}$$

since it travels horizontally o to get to the aperture and $2L$ (travels the cavity back and forth), and vertically $A/2$ since any value higher hits the top surface. Consequently, the formula for this first-order approximation, for uniform power distribution, is:

$$P_{abs} = P_0\left(1 - \frac{\beta}{\alpha_0}(1-\varepsilon)\right). \tag{B.3}$$

For a Gaussian distribution, it is necessary to calculate the power that is inside that range. The approximation will be best in scenarios where the remaining angle ranges' power is highly absorbed such as high emissivity and/or high number of reflections or is small such as low α_0. It is important to note that β might be higher than α_0 and in that case β is replaced by α_0.

To improve this approximation, it is possible to calculate the range in which there are only two reflections. Considering the theory of specular reflection, this is the case where the ray either hits the bottom and then the upper lateral and exists or hits the upper lateral and then the bottom and leaves through the aperture. This translates to the following equation:

$$\tan\left(\psi_1, \psi_2\right) = \frac{D \mp A/2}{2L+o}, \tag{B.4}$$

since the ray travels vertically D (twice the upper half) and $2L+o$ similarly to the previous case. The $\mp A/2$ term is trivially needed to add to the vertical distance as it represents the two extremes of the aperture. The second-order approximation is, in uniform distribution:

$$P_{abs} = P_0\left(1 - \frac{\beta}{\alpha_0}(1-\varepsilon) - \frac{\psi_2 - \psi_1}{\alpha_0}(1-\varepsilon)^2\right). \tag{B.5}$$

Again, there is no guarantee that the result of this equation is entirely inside the $[0, \alpha_0]$ range; if ψ_1 is higher than α_0 then no angle range reflects only twice and the term is null; if ψ_1 is lower than α_0 but ψ_2 is higher then the latter is replaced by α_0; if both are inside the range there is no change to be made. Also, ψ_1 is always higher or equal to β since $D \geq A$ and, thus, no interference occurs.

By deriving the equations for the possible third reflections and so on, a pattern was identified. Each pair of angles can be determined by:

$$\tan\left(\phi_i, \phi_{i+1}\right) = \frac{aD \mp A/2}{2bL+o}, \tag{B.6}$$

where a and b are positive integers. The former represents how many times the ray reflects into the lateral areas, it can never travel non-integer values of D since it always travels $D/2$ twice (for example, going to the upper lateral and coming back down the middle). The latter is related to how many times the ray has reflected into the bottom or top sides, it is multiplied by 2 since it has to travel an even distance due to there only existing an aperture on one side.

The number of reflections of the range ϕ_i and ϕ_{i+1} is calculated by $a+2b-1$. The presence of the minus one in the equation is due to the fact that when exiting the cavity there is no reflection. Therefore, for example, the angle interval where $a=4$ and $b=2$ has 7 reflections and it represents the scenario where the ray hits the bottom surface twice and the lateral walls 4 times.

It is important to stress that, although the equations have solutions, it does not necessarily mean that that particular range plays a part in the reflections. The equations only tell us that, if there is such a type of reflection in this scenario, it would be within this range but it does not grant that such a type of reflection in fact exists. This is the result of the equation not taking into account the possible fact that the ray left the cavity before. For example, consider there are two intervals A and B and the second is inside the first, what happens then? The solution to this situation lies in the number of reflections. If the number of reflections of interval A is lower than B, then it means that the range B had already left the cavity before continuing its reflections; thus interval B is ignored and the interval A is considered as a whole with its number of reflections. If the number of reflections of interval A is higher than B's then the interval A B is considered to have the same number of reflections as A and the interval B remains untouched with its respective reflection number.

Now that there is a clear understanding of the physics and a global equation (B.6) that calculates the angle ranges, the algorithm can be developed.

This algorithm takes several inputs, including the geometrical properties of a cavity (length, diameter, and aperture) and properties of a light beam (angle of incidence and origin). Two important matrix variables are used: "Boundary" and "Reflection_Matrix." "Boundary" is initialized with the range $[0,\alpha_0]$ (where α_0 is the initial angle of incidence), and "Reflection_Matrix" is initially empty. The purpose of this algorithm is to calculate the ranges of angles and the number of reflections at each range as a beam reflects inside the cylindrical cavity. The algorithm works as follows:

1. Calculates β and subtract the range $[0,\beta]$ from "Boundary." Add this range to "Reflection_Matrix" with a reflection number of 1. This represents the first reflection of the beam.

2. The algorithm enters an outer loop that continues until "Boundary" is empty. This means that all possible ranges of angles have been accounted for in "Reflection_Matrix" with their respective reflection numbers.

3. Inside the outer loop, a is initialized to 1. The inner loop calculates the range of angles until a condition is met: it increments a until the calculated angle ϕ_i is greater than the initial angle of incidence α_0.

4. For each calculated range of angles, the algorithm checks if there is an intersection between this range and the ranges in "Boundary." If an intersection is found, it is removed from "Boundary" and added to "Reflection_Matrix" with the appropriate reflection number.

5. After the inner loop finishes, b is incremented, and the outer loop runs again. This process continues until "Boundary" is empty, ensuring that all possible ranges of angles and their reflections are accounted for.

In summary, this algorithm systematically calculates and records the ranges of angles and the number of reflections of a light beam as it reflects inside a cylindrical cavity, using the given geometrical and beam properties. It is a process of iteratively calculating and updating ranges until all possible reflections have been considered.

It is relevant to confirm that there are no situations where an angle interval with higher priority (fewer reflections) is overtaken by an interval with lower priority. Examining the inner loop, where b is constant and a is incremented, the intervals cannot intercept due to the restriction $D \geq A$ so there is no problem; additionally, even if they intercepted, since the algorithm considers the intervals in an ascending order of reflections, it would not be a problem. However, considering the outer loop, where b can have different values, is not as trivial as the previous case to ensure that the situation does not occur. In order to examine this, let us investigate if there exists an interception between two intervals with different a and b values but the same number of reflections; such implies that:

$$a + 2b = a' + 2b', \tag{B.7a}$$

$$b < b' \Leftrightarrow b' = b + k \implies a = a' + 2k \tag{B.7b}$$

where a and b are coefficients of one interval, a' and b' of the other and k a positive integer. The last implication derives from the combination of the two equations. If the lower boundary of the first interval is higher than the upper boundary of the second interval, then, the intervals do not intersect. In fact, this is the case:

$$\frac{aD - \frac{A}{2}}{2bL + o} > \frac{a'D + \frac{A}{2}}{2b'L + o} \Leftrightarrow$$

$$L\,[2kD(a + 2b) - A(2b + k)] + o(2kD - A) > 0. \tag{B.8}$$

The derivation was done considering the previous conditions. Consequently, there are two main terms: one involving L and the other o. The former is always positive since $D \geq A$ and the coefficient of the latter is also always positive. Consequently, for null and positive values of o, the condition is true. However, o can be negative as far as $-L$ to be physically coherent. Nevertheless, in the extreme case where $o = -L$, the equation is:

$$L[2kD(a + 2b - 1) - A(2b + k - 1)] > 0, \tag{B.9}$$

which is still true due to $D \geq A$. Thus, it is proven that when the algorithm reaches the region of the first interval again with a different b, this one has more reflections and thus lower priority.

Consequently, the way the algorithm searches for the intervals never produces situations where low-priority intervals are chosen instead of higher-priority ones when these share values.

C

View Angle Method

In this chapter, a theoretical approach to calculating the percentage of beam power absorbed by a cavity is described in detail. In this case, the approach was explored for the 2D rectangular and conical cases. Moreover, the difficulties encountered in this approach are mentioned as well as alternatives that might extend the prediction beyond its limitations.

Rectangular

Consider a rectangular cavity with length L, diameter D, aperture size A and emissivity ε, as well as a beam with a diverging half-angle α_0, origin o and total power P_0. Regarding reflection, for this algorithm, the surface is considered to reflect the ray equally in all directions (Lambertian reflection).

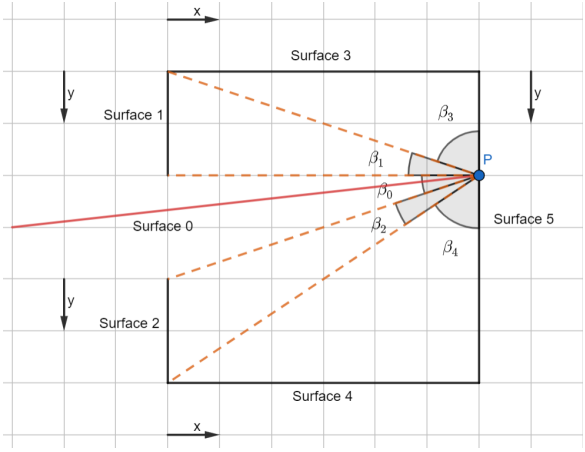

Figure C.1: Probability of diffuse reflection inside a rectangular cavity

Fig. C.1 illustrates the idea behind the whole algorithm. Consider a ray that hits surface 5 at point P. The probability that it bounces back to surface i is related to β_i, considering the distribution profile of a specular reflection. Therefore, as long as the point where the ray hits a surface is known, it is possible to calculate its fraction losses. It is relevant to note that probability and fraction are somewhat interchangeable terms in this context: probability is suited if only one ray is reflected (it is the case in ray-tracing software to decrease computational demand such as COMSOL) and fraction is suited if the ray is split into several others equally spaced after the reflection and, thus, fractions of the initial ray will go to all the other surfaces. For the sake of this algorithm, the latter case is considered.

To simplify the explanation, let us consider the scenario where the beam does not reach surface 3 in its first hit i.e. it only hits surface 5. Also, due to symmetry, it is only studied the positive half of the angle interval. The height h (0 at the middle of surface 5 and with a positive sign upwards) at which a ray with angle α hits surface 5 can be determined by:

$$h(\alpha) = (o + L)\tan(\alpha). \tag{C.1}$$

By knowing the height at which the ray intersects surface 5, it is possible to calculate the view angle to other surfaces. For instance, the view angle from the first hit at surface 5 to surface 3 V_{53} is:

$$V_{53}(\alpha) = \frac{1}{2}\left(1 + \frac{h(\alpha) - \frac{D}{2}}{L\sqrt{1 + \left(\frac{h(\alpha) - \frac{D}{2}}{L}\right)^2}}\right). \tag{C.2}$$

The rest of the view angles (V_{50}, V_{52}, V_{53},V_{54} follow similarly by geometry. Consequently, it is possible to determine the fraction of the beam that goes to each surface. For instance, the beam fraction that escapes after only one reflection f_{50} is determined by:

$$f_{50} = \frac{1}{\alpha_0}\int_0^{\alpha_0} V_{50}(\alpha)\,d\alpha, \tag{C.3}$$

where the integral divided by the angle determines the average view angle to surface 0.

However, this form of view angles formula only allows us to calculate up to two absorptions since it does not provide information about where the second reflection occurs which is crucial to identify the next view angles. Thus, a view angle formula which determines the distribution of the second reflection is required. For example, considering the view angle V_{53} again, what we want to know is the distribution of the fractions along surface 3 which means we want to know how the view angle changes in terms of dx (refer to the coordinate system in Fig. C.1). It is possible to write V_{53} in terms of α and x:

$$V_{53}(\alpha,x)=\frac{1}{2}\left(1+\frac{h(\alpha)-\frac{D}{2}}{(L-x)\sqrt{1+\left(\frac{h(\alpha)-\frac{D}{2}}{L-x}\right)^2}}\right). \tag{C.4}$$

and to find the distribution in terms of dx, one just needs to derive the previous equation:

$$P_{53}(\alpha,x)=\frac{\partial V_{53}(\alpha,x)}{\partial x}. \tag{C.5}$$

This method allows us to calculate the other view angle distributions P_{52}, P_{53},P_{54}. P_{50} is undeniably irrelevant since it does not reflect back into the cavity. Now, the beam fraction which hits surface 5 and goes to surface 1 f_{51}, for instance, can be calculated in two ways:

$$f_{51}=\frac{1}{\alpha_0}\int_0^{\alpha_0}V_{51}(\alpha)d\alpha=\frac{1}{\alpha_0}\int_0^{\alpha_0}\int_0^{\frac{D-A}{2}}P_{51}(\alpha,y)dyd\alpha. \tag{C.6}$$

How can we now calculate, for example, f_{515}, the fraction that hits surface 5, surface 1 and again to surface 5? We now have information about the distribution in terms of dy that reaches surface 1, so the only aspect missing is a view angle formula that determines the view angle to surface 5 for a point y in surface 1. Using geometry, it is trivial to reach the following $V_{15}(y)$:

$$V_{15}(y)=\frac{1}{2}\left(\sin\left(\arctan\left(\frac{y}{L}\right)\right)-\sin\left(\arctan\left(\frac{y-D}{L}\right)\right)\right), \tag{C.7}$$

and, thus,

$$f_{515}=\frac{1}{\alpha_0}\int_0^{\alpha_0}\int_0^{\frac{D-A}{2}}P_{51}(\alpha,y)V_{15}(y)dyd\alpha, \tag{C.8}$$

gives the desired beam fraction. The rest of $V_{ij}(x_i)$ can be determined geometrically as well.

However, the same problematic situation appears, $V_{15}(y)$ gives us information about the fraction that goes into surface 5 but nothing regarding the distribution of the rays. Nevertheless, the solution is exactly the same: write the view angle formula taking into account y_2 (here we use another y to distinguish between the y of surface 1) and derive it in order of y_2:

$$V_{15}(y,y_2)=\frac{1}{2}\left(\sin\left(\arctan\left(\frac{y}{L}\right)\right)-\sin\left(\arctan\left(\frac{y-y_2}{L}\right)\right)\right), \tag{C.9}$$

$$V'_{15}(y,y_2)=\frac{\partial V_{15}(y,y_2)}{\partial y_2} \tag{C.10}$$

Consequently, for example, f_{5150} (fraction of the beam which reflects onto, in sequence, surface 5, 1, 5 and leaves the cavity) can be calculated by:

$$f_{5150} = \frac{1}{\alpha_0}\int_0^{\alpha_0}\int_0^{\frac{D-A}{2}}\int_0^{D} P_{51}(\alpha, y)V'_{15}(y, y_2)V_{50}(y_2)dy_2dyd\alpha. \tag{C.11}$$

In general, the formula for the fraction of the beam that hits the surface z after reflecting into n surfaces $i, j, k, ..., x, y$ is:

$$f_{ijk...xyz} = \frac{1}{\alpha_0}\int_0^{\alpha_0}\int_0^{L_j}\int_0^{L_k}\cdots\int_0^{L_x}\int_0^{L_y} P_{ij}(\alpha, j)V'_{jk}(j, k)... \\ V'_{xy}(x, y)V_{yz}(y)dydx...dkdjd\alpha, \tag{C.12}$$

where L_j is the length of the surface j and so on.

So far, the scenario where α_0 is high enough to reach surface 3 has been ignored. Nevertheless, there are not many changes in the process in that scenario. One needs to deduce the view angle formulas of the form $P_{3j}(\alpha, y)$. Additionally, the boundary of the $d\alpha$ integral needs to be changed. The angle where the separation occurs α_s is:

$$\alpha_s = \arctan\left(\frac{\frac{D}{2}}{L+o}\right). \tag{C.13}$$

The boundary of the $d\alpha$ integral when the fraction starts with a reflection on surface 5 instead of being 0 and α_0 is 0 and α_s and the boundaries when the fraction reflects on surface 3 first are α_s and α_0.

From the general equation (C.12), it is clear that, to calculate a fraction which entails n reflections, $n-1$ integrals need to be calculated and all of the functions being integrated are indirectly related, making it impossible to separate them in order to simplify the integration process. Also, the functions are not trivial. Consequently, the calculation process for each fraction becomes highly computationally demanding as the number of reflections goes up. Moreover, the number of integrals increases exponentially: the second absorption has 4 single integrals to calculate, the third absorption has 14 double integrals and the fourth absorption has 416 triple integrals; and it gets worse if α_0 is high enough to also have an initial reflection on surface 3. Consequently, it is irrefutably wise to truncate the algorithm at some point and that point should be determined individually taking into account the computer used and the desired accuracy.

There are a few concepts that allow us to reduce the complexity of the calculation. First, it is important to acknowledge that calculating, at each stage, the beam fraction that leaves the cavity and, thus, is not absorbed entails fewer integrals than calculating each surface absorption. For example, to calculate the beam fraction which escapes until the fourth absorption only 1 single integral, 2 double integrals and 10 triple integrals. This is an irrefutable lower computational requirement compared to the previously mentioned 416 triple integrals. By knowing what amount leaves the cavity at each stage, it is possible to calculate the amount that has been absorbed so far (which sets a lower limit for the total absorption) as well as the maximum total absorption possible (the scenario where the remaining power is all absorbed). Another aspect that reduces the number of integrals needed is the fact that rays cannot go from surface 1 to surface 0 and surface 2 and equally from surface 2 to surface 0 and surface 1. For instance, the

number of triple integrals would be 16 instead of 10 in the previous case. In addition, not being able to escape the cavity directly after reflecting onto surfaces 1 and 2 requires that those fractions are once again reflected inside the cavity and another absorption event occurs. This allows the calculation of some of the beam fractions that suffer at least 5 reflections with a triple integral. To better illustrate, it is possible to calculate, for example, f_{5151} with a triple integral only and that fraction is guaranteed to be absorbed again and, thus, no need for quadruple integrals. With this information, the lower boundary can be slightly increased and, therefore, reduce the estimation range.

Due to the increased complexity of using quadruple integrals and so forth, the algorithm uses only up until the triple integral. As explained above, this allows us to calculate the estimation range fully considering 4 reflections and some of the fraction that reflects 5 times. The difference between the lower and upper limits is the remaining power of the rays still inside the cavity. After 4 reflections the remaining power is in the order of $(1-\varepsilon)^4$ which is undoubtedly only a concern in the low emissivity range. Therefore, the higher the emissivity the smaller the estimation interval and, for high emissivities, it is expected that the range is small enough to give a good estimate. However, for low emissivity values, the lower boundary is certainly far from the upper boundary to provide any good estimate. For example, with $\varepsilon = 0.1$, after 4 reflections, in the extreme scenario that no fraction escaped the cavity, the total power absorbed would be at 34.39% (which is the lower boundary) and the upper boundary would be 100%. Unless the cavity exhibits a geometry which allows for a huge amount of rays to exit after 4 reflections, which is already undesirable, the calculated range will not be small enough to provide any meaningful insight.

In an attempt to fix the issue at low emissivity values, the Gebhart factors are used. In fact, this might appear contradictory to the previous claim that the view factors can not be applied to calculate the total power absorption from the start but the difference lies in the distribution of the rays. In the beginning, the beam presents itself as a bundle of rays with defined directions, nothing similar to a diffuse scattering from the opening, which gives a proper and non-uniform distribution of the targeted areas. However, as the rays reflect several times, the distribution of the reflections in the surfaces starts to, at least, not look as concentrated as in the first reflection stage. Thus, it makes more sense to consider that the remaining beam ray distribution is closer to a uniform distribution (which is what the view factors consider). Nevertheless, there is no certainty that the distribution converges to a uniform distribution (it probably does not), even more only after 4 reflection steps. To sum up, this approach is not guaranteed to provide good estimates but there is a reasonable justification to consider it at this stage.

The view factors F_{ij} are easily determined due to the simple geometry. The Gebhart factors of surface i to surface j, B_{ij}, is calculated with:

$$B_{ij} = F_{ij}\varepsilon_j + \sum_{k=1}^{n} (1-\varepsilon_k) F_{ik} B_{kj}. \tag{C.14}$$

In this case, we are interested in calculating the Gebhart factors to surface 0, whose emissivity is unitary for calculation purposes. Due to symmetry, it is only required to solve the B_{10}, B_{30} and B_{50} system of equations since $B_{10} = B_{20}$ and $B_{30} = B_{40}$ due to symmetry. Next, the average $B_{(1,2,3,4,5)0}$ can be calculated:

$$B_{(1,2,3,4,5)0} = \frac{(D-A)B_{10} + 2B_{30}L + B_{50}D}{D + (D-A) + 2L}, \tag{C.15}$$

and, thus, quantifies the ratio between the beam power that will leave the cavity and the total beam power still present. Consequently, 1-$B_{(1,2,3,4,5)0}$ is the percentage of the remaining beam power which is absorbed. By multiplying the percentage with the remaining beam power and adding it to the lower boundary estimated previously, a new estimation of the total power absorbed is made.

To sum up, the full algorithm will be explained. First, the inputs are the geometrical characteristics of the rectangular cavity (length L, aperture A, diameter D) as well as its emissivity ε, and the beam's diverging half-angle α_0 and its origin o. All the forms of the needed view angle formulas V_{ij} and its derivatives P_{ij} and V'_{ij} are provided. Then, α_s is calculated and if $\alpha_s \leq \alpha_0$ surface 5 is the only surface where the beam reflects first, whereas if $\alpha_s > \alpha_0$, then also the beam has a first reflection on surface 3 and the possible trajectories increases and more integrals need to be calculated. Either way, the way these integrals are defined has already been explained thoroughly, only the number increases. The beam fractions that leave after one, two and three reflections are calculated. Additionally, the beam fractions that have their fourth reflection in surfaces 1 and 2 are calculated (since we know that they will reflect a fifth time inside the cavity). Then, $B_{(1,2,3,4,5)0}$ is calculated considering the cavity's geometry. Finally, the three outputs are calculated. The maximum possible fraction of beam power absorbed by the cavity is:

$$P_{abs\,\max} = \left(1 - (1-\varepsilon)f_1 - (1-\varepsilon)^2 f_2 - (1-\varepsilon)^3 f_3\right), \tag{C.16}$$

where f_i is the beam fraction which leaves after i reflections. The fraction of beam power which is guaranteed to be absorbed and, thus, the minimum:

$$P_{abs\,\min} = \left(\sum_{n=0}^{3} \varepsilon(1-\varepsilon)^n \left(1 - \sum_{i=0}^{n} f_i\right)\right) + (1-\varepsilon)^4 \varepsilon f_{1+2}, \tag{C.17}$$

where f_{1+2} is the beam fraction that has its fourth reflection in surfaces 1 or 2. Lastly, the Gebhart factor estimation is:

$$P_{abs\,\text{est}} = P_{abs\,\min} + \left(1 - B_{(1,2,3,4,5)0}\right)\left(P_{abs\,\max} - P_{abs\,\min}\right) \tag{C.18}$$

CONE

Consider a conical cavity with length L, diameter D, aperture size A and emissivity ε, as well as a beam with a diverging half-angle α_0, origin o and total power P_0. Again, for this algorithm, the surface presents Lambertian reflection.

Fig. C.2 illustrates the idea behind the algorithm as well as the numbering of the surfaces and the coordinate system used. It is clear that there are similarities between the conical and the rectangular case. In fact, the differences are the view angle formulas V used, the numbering of the surfaces and coordinate system, and the view factors. For example, the view angle from the first reflection to surface 1 is:

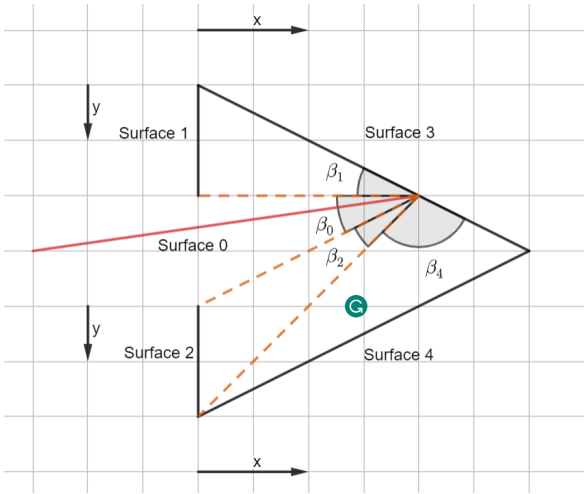

Figure C.2: Probability of diffuse reflection inside a conical cavity

$$V_{31}(\alpha) = \gamma - \arctan\left(\frac{\frac{A}{2} - h(\alpha)}{L - \frac{h(\alpha)}{\tan(\gamma)}}\right), \tag{C.19}$$

where γ is the cone half-angle:

$$\gamma = \arctan\left(\frac{D}{2L}\right), \tag{C.20}$$

and $h(\alpha)$ is the height at which the ray intersects surface 3, similar to the concept in the rectangular case:

$$h(\alpha) = \frac{(L+o)\tan(\alpha)}{1 + \frac{\tan(\alpha)}{\tan(\gamma)}}. \tag{C.21}$$

The beam fraction calculations follow the same principle as the rectangular case. In this case, there is no α_s as the beam always hits only surface 3 at the first reflection stage. Due to the reduced number of surfaces, the integrals to be evaluated when calculating the fractions that leave the cavity are fewer: 1 single integral for the fraction after the first reflection, 1 double integral for the one after the second reflection and 5 triple integrals for the one after the third reflection. Moreover, if someone would want to calculate the integrals regarding the fraction that leaves after its fifth reflection it would only need to evaluate 7 integrals instead of around 32 in the rectangular case. This makes the conical scenario more suitable for further estimation improvement without compromising the performance as much.

Regarding the Gebhart factor estimation, the only thing that changes is the view factor formula F_{ij} due to the different geometry. As the B_{ij} formula is identical, so not much change is needed.

To sum up, the algorithm essentially is the same with different view angle formulas and view factors due to different geometry. Moreover, the reduced number of surfaces is beneficial to reduce the computational effort required.

D

Beam Absorption Results

In this chapter, relevant plots of the results of the explored beam power absorption in a cavity in this thesis are presented. More precisely, the effect of each variable in the outcome as well as the effect of surface reflection properties for all geometries is explored.

D.1. Variable Effect

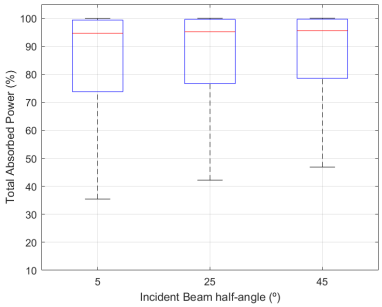

(a) Effect of incident beam angle

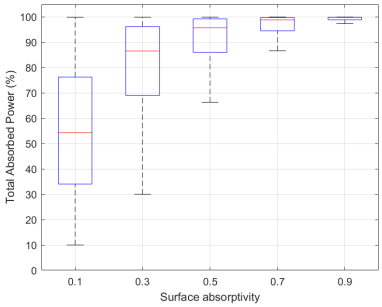

(b) Effect of surface absorptivity

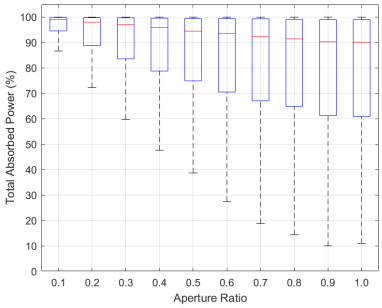

(c) Effect of aperture ratio

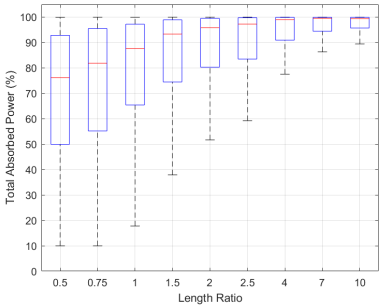

(d) Effect of length ratio

Figure D.1: Variable effect on total absorption percentage specular reflection of all geometries

D.2. SURFACE REFLECTIVITY

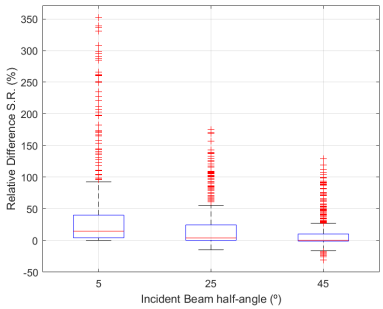

(a) Effect of incident beam angle

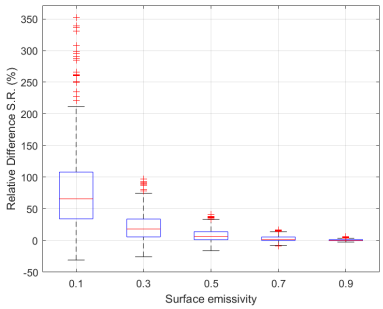

(b) Effect of surface emissivity

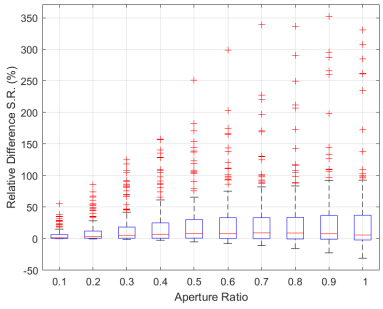

(c) Effect of aperture ratio

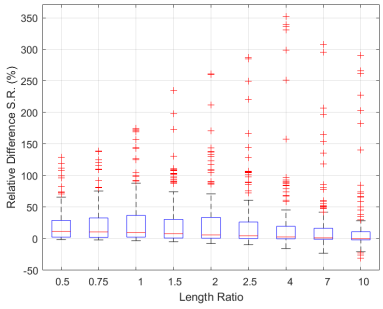

(d) Effect of length ratio

Figure D.2: Variable effect on relative power absorption difference between diffuse and specular surfaces in a cylindrical cavity

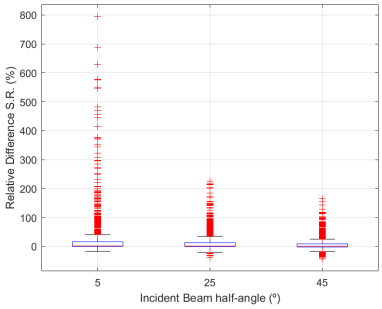

(a) Effect of incident beam angle

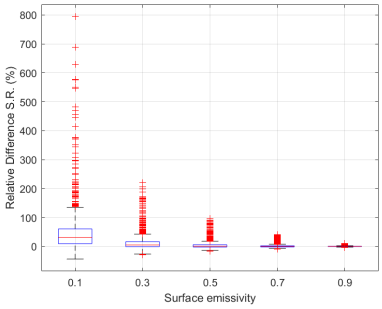

(b) Effect of surface emissivity

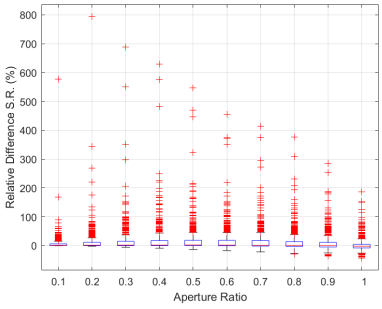

(c) Effect of aperture ratio

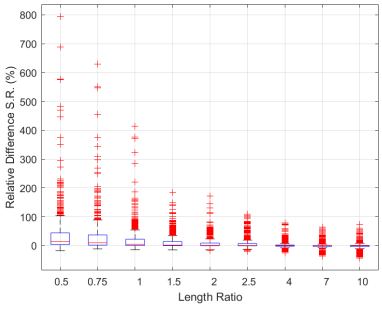

(d) Effect of length ratio

Figure D.3: Variable effect on relative power absorption difference between diffuse and specular surfaces in a concylindrical cavity

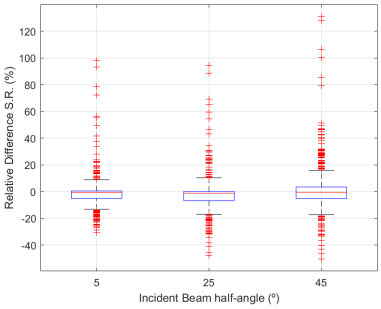

(a) Effect of incident beam angle

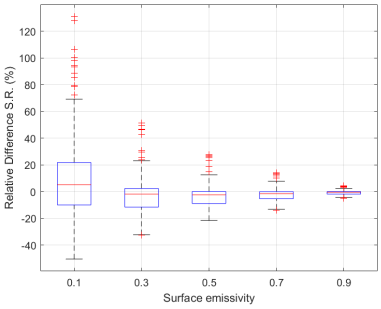

(b) Effect of surface emissivity

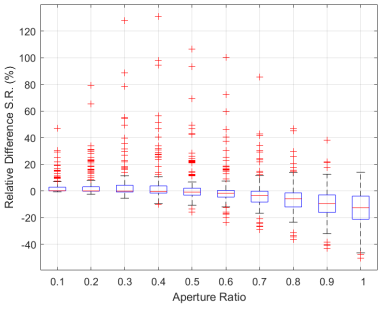

(c) Effect of aperture ratio

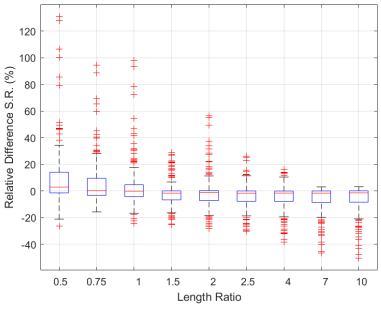

(d) Effect of length ratio

Figure D.4: Variable effect on relative power absorption difference between diffuse and specular surfaces in a conical cavity

E

CONVECTION - LITERATURE STUDY

In this chapter of the appendix, the convection section of the literature study [1] is presented as well as the pressure gradient calculations.

This chapter is a good starting point for the modelling of heat transfer in thermal thrusters where a fluid is heated to a high temperature through convection. However, it mainly focuses on open cavities related to indirect heating beam-powered thermal propulsion thrusters. The book from Lienhard "A Heat Transfer Textbook" [2] is a good source of information for heat transfer mechanisms and heat exchangers in general. Nevertheless, some specific scenarios are not presented there and, thus, require the search for information in the literature

First, the inner cavity convection losses are explored with mentions of relevant literature findings. Next, propellant convection, single-phase a two-phase flow, is explored. Then, formulas to predict the outer convection losses from the literature are present as well as their restrictions. Lastly, methods to calculate a propellant's pressure variation along pipes are presented.

E.1. CONVECTION

Convection is the heat transfer mechanism related to the transfer of heat between a bounding surface and a fluid in motion or across the flow plane within the interior of the fluid. When the fluid motion is caused by, for example, a pump or a fan, it is called forced convection, and, when the fluid motion is caused by density differences due to temperature differences, it is named natural convection [3].

Convection is governed by Newton's law of cooling:

$$Q_c = h_c A \Delta T, \tag{E.1}$$

where Q_c is the rate of heat transfer, h_c is the convective heat transfer coefficient, and ΔT is the temperature difference which depends on the situation [3]. The value of h can vary drastically depending on several factors such as geometry and temperature, and it can be calculated by:

$$h_c = \frac{Nu \cdot k}{L_s}, \tag{E.2}$$

where k is the fluid's thermal conductivity, L_s is the characteristic length which depends on geometry, and Nu is the Nusselt number [4]. There are several empirical relations to calculate Nu which depend highly on the scenario.

The RAC will experience natural convection in its inner cavity and outer wall. On the other hand, forced convection occurs inside the propellant tubes from the hot wall to the fluid.

E.1.1. INNER CAVITY CONVECTION

The heating of the cavity leads to convection heating of the fluid inside the cavity. In space, since there is a vacuum, this is no concern, however, on earth, this can only be avoided by using a vacuum chamber. This subject is a great concern in solar cavity receivers of parabolic dish-receiver systems and solar power tower [5] [6] and several formulas have been established with experimental and numerical data [7] [8]. However, most of the studies focus on downfacing angles as its the main situation in those scenarios and the formulas are not usually exact with margin errors of 50% [8]. The most relevant and simple conclusions from research are that the convection loss is highly dependent on the angle of the opening, the loss increases with the increase in the aperture and outer diameter ratio, and higher inner wall temperature [7].

A recent paper by Wang K. et al. performed a numerical study on the natural convective heat loss of an isothermal upward-facing cylindrical cavity [9]. In the paper, AR corresponds to the opening ratio, ϕ to the angle (-90° means upward and 0° means sideways opening), Q_c the convection heat loss and T_w to the inner temperature. Regarding the effect of the inner temperature, there is a linear relationship between T_w and Q_c and the slope diminishes with AR decrease (fig. E.1a Natural convection heat loss is maximum at around -30° and is minimum at -90° which is explained by the higher velocity of inflow and outflow of air into the aperture (fig. E.1b). Finally, concerning AR, it is clear that lower values lead to lower natural convection losses as the decrease in area obstructs the natural air flow (Fig. E.1c).

From the results, an empirical relation to estimating Q_c in an open cylindrical cavity has been established. The Nusselt Number is calculated by:

$$Nu_D = 7.26 \times 10^{-5} Gr^{0.3533} [4 + cos(\phi + 30)]^{5.8632} \left(\frac{A_{ap}}{A_{cav}}\right)^{1.0266}, \tag{E.3}$$

where A_{ap} is the aperture's area, A_{cav} is the heat transfer area (in this case, the cavity's inner wall), and Gr is the dimensionless Grashof number (ratio of the buoyancy to viscous forces acting on a fluid) and is calculated by:

$$Gr = \frac{g_0 \beta \rho^2 (T_w - T_\infty) D^3}{\mu^2}, \tag{E.4}$$

where g is the acceleration of gravity, β the fluid's thermal expansion coefficient, T_∞ the air's surrounding temperature, and D is the cylinder's diameter. Then the total heat loss by convection Q_c is:

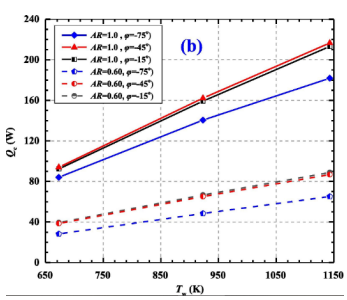

(a) T_w for different AR and ϕ values.

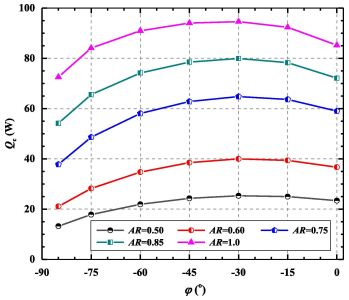

(b) ϕ under different AR at Tw = 673 K

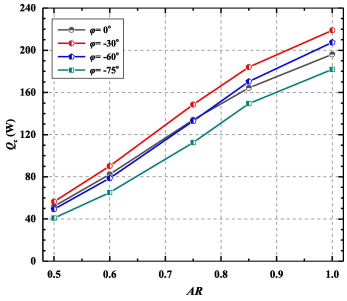

(c) AR under different ϕ at T_w = 1143 K

Figure E.1: Variations of Q_c for a cylindrical cavity in different conditions [9].

$$Q_c = h_c A_{cav}(T_w - T_\infty) = \frac{Nu_D k}{D} A_{cav}(T_w - T_\infty). \tag{E.5}$$

It is relevant to mention that these equations are valid for $-85° \leq \phi \leq 0°$, $0.50 \leq AR \leq 1.0$, and $7.82 \times 10^5 \leq Gr \leq 1.94 \times 10^6$. About 98.1% and 76.2% data points fluctuate within ±20% and ±10%, respectively, which indicates that the prediction accuracy of the correlation is fairly satisfactory [9].

Regarding conical-shaped cavities, there appears to not be much research available especially in upward-facing angles with no wind conditions. However, Jilte R. et. al [10] performed natural convection loss simulations with sideways as well as downward angles with several types of geometry, including cylindrical and conical shapes, in two distinct cases. In the first one, the heat transfer area was the same for all geometries, and, in the second one, the aspect ratio was equal (in this paper, defined as the ratio of the cavity's length and its aperture diameter). From the results displayed in figures E.2a and E.2b, it is clear that the conical-shaped cavity is always the shape with the lowest convection loss. Thus, with the assumption that this relative trend remains in upward-facing angles, the cone has lower convection heat losses than the cylinder. It is relevant to mention that, in this paper, the aperture ratio is unitary and an alternative value could possibly result in a different relation between the two geometries. From the data, a possibly fair estimate for the conical scenario seems to be calculating the convection loss with Wang K. et al. method [9] for a cylinder with an equal heat transfer area.

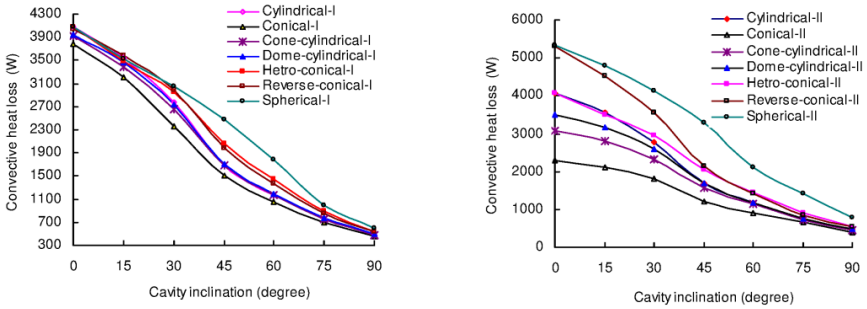

(a) Case I - Equal heat transfer area

(b) Case II - Equal aspect ratio

Figure E.2: Convection heat loss for different geometries [10].

Takken A. [11] and Leenders H. [12] used a correlation method developed for open cavity receivers by Paitoonsurikarn S. et al. [13]. Despite being valid for conical and cylindrical shapes, it is only valid for side-ways orientation. Nevertheless, from Wang K. et al. [9], more specifically fig. E.1b, the side-ways condition tends to result in a slightly higher convection loss and, thus, the method might determine a maximum loss value.

E

E.1.2. SINGLE-PHASE PROPELLANT CONVECTION

The heat transfer from the wall to the fluid is the main principle of the RAC and, thus, it is undeniably important concerning its performance. The wall's temperature T_w can be considered somewhat uniform throughout the propellant flow due to its high thermal conductivity [2]. Thus, from [2], the convective heat transferred Q_c as well as the final temperature, follow this relation:

$$Q_c = \bar{h}A\frac{(T_{p,\,f} - T_{p,\,i})}{\ln\left(\frac{T_{p,\,f}-T_w}{T_{p,\,i}-T_w}\right)} = \dot{m}c_p(T_{p,\,f} - T_{p,\,i}), \tag{E.6}$$

where $\bar{h}$ is the mean convective heat transfer, A is the surface area, T_p is the propellant's temperature, $\dot{m}$ is the mass flow, c_p is the propellant's specific heat capacity, and the subscripts i and f refer to initial and final conditions, respectively. The logarithmic mean temperature difference is present due to the decrease in the difference between the temperatures of the propellant and wall along the duct. A rearrangement of equation (E.6) leads to:

$$\frac{T_{p,\,f} - T_{p,\,i}}{T_w - T_{p,\,i}} = 1 - exp\left(-\frac{\bar{h}PL}{\dot{m}c_p}\right), \tag{E.7}$$

where A was substituted by the multiplication of the tube's length L and its cross section's perimeter P to illustrate better their influence.

It is clear that $\bar{h}$ highly influences the convective heat transfer and, from equation (E.2), it is dependent on the Nusselt number. However, before going directly to its formula, the Nusselt number depends on several variables which will be examined first.

Reynolds Number

The Nusselt number depends on the propellant's flow type: laminar, transitional or turbulent. That flow's characteristic is determined by the dimensionless Reynolds number Re which is the ratio between inertial forces to viscous forces, and it is given by the following equation:

$$Re_D = \frac{\rho u D}{\mu} = \frac{4\dot{m}}{P\mu}, \tag{E.8}$$

where ρ is the density, u is the velocity, D is the diameter, μ is the dynamic viscosity and P is the perimeter.

Laminar flows are described by Reynolds numbers below 2300 whilst turbulent flow from Reynolds numbers of 10000 [2]. Turbulent flow has higher convection heat transfer than laminar flow and, thus, achieving that regime might be beneficial and can be done by increasing mass flow or diminishing the duct's perimeter. However, the propellant's velocity can not be too high as it can experience what is called water-hammer. Zandbergen [4] presents a formula to calculate its upper limit:

$$u_{max} = 175\left(\frac{1}{\rho}\right)^{0.43}. \tag{E.9}$$

Thermal entrance length and Prandtl Number

Another Nusselt number dependency is if the flow regime is fully developed. The flow can be hydro-dynamically developed (the velocity profile is constant along the duct) and thermally developed (the temperature profile is constant along the duct) [2]. It is important to notice that the flow can not be thermally developed without hydro-dynamical development.

The thermal entrance length is the section at the start of the pipe where the flow is not thermally developed and, therefore, the temperature profile is not constant, causing variations in the Nusselt number. For laminar flow, the thermal entrance length x_{e_t} formula at a uniform wall temperature is [2]:

$$\frac{x_{e_t}}{D} = 0.034 Re_D Pr, \tag{E.10}$$

where Pr is the dimensionless Prandtl number which is the ratio between momentum diffusivity and thermal diffusivity [3]:

$$Pr = \frac{\mu c_p}{k}. \tag{E.11}$$

Regarding turbulent flow, there is no gratifying general equation for the thermal entrance length but it is generally accepted that it does not depend on the Reynolds number for enough large Prandtl numbers. Bergman T. et al. [14] provide a fair estimate:

$$\frac{x_{e_t}}{D} = 10. \tag{E.12}$$

Generally, the convective heat transfer is higher at the entrance region and the equations for the Nusselt number are averages throughout the whole pipe which take into account said region [14]. In an isothermal pipe, when the fluid is fully developed the Nusselt number is equal to:

$$Nu_D = 3.657. \tag{E.13}$$

Consequently, the formula for Nu_D is expected to converge to this value (from higher values) as the thermal entrance section becomes relatively smaller than the duct's length. In 1956, Sellars, Tribus, and Klein solved the problem of the constant wall temperature proposed by Graetz and discovered there is a useful dimensionless number to take into account the effect of the thermal entrance section - the Graetz number Gz - which is calculated by [2]:

$$Gz = \frac{Re_D Pr D}{L}, \tag{E.14}$$

where D is the duct's diameter and L is the length.

Hydraulic Diameter

The previous equations were all based on circular ducts and the Nusselt number is affected by the ducts' geometry. Nevertheless, all the previous thought process is still valid but the equations need to be adjusted. The hydraulic diameter D_h can be used to approximate the heat transfer coefficients in non-circular pipes [2]:

$$D_h = \frac{4A}{P}. \tag{E.15}$$

The results from this substitution in all the previous relevant formulas are usually within ±20% and often within ±10% and the worse results are generally present in sharp angle geometry such as acute triangles [2]. This accuracy can be improved by applying specific geometry equations that can be seen in [3].

Channel Layout

From previous work [11] [12] [15], the choice has been mainly between two different channel layouts: linear tubing or spiral tubing. In fact, this property influences as well the Nusselt number [4]. For its conical cavity, Leenders H. used linear tubing [12] while Takken A. chose spiral for its cylindrical cavity [11].

For the same cavity's length, spiral tubing has the advantage over linear tubing since it can increase its contact length. This increase in length can be varied as the spiralling angle can be changed. Furthermore, Rohsenhow W. et al. mention that spiral flow has a higher heat transfer due to a secondary flow induced by the presence of centrifugal forces. Consequently, spiral tubing is widely used in industry [3].

Surface Roughness

When the surface of a pipe is rough enough, it can disturb the thin layers of fluid near the surface that affect how heat and momentum transfer between the fluid and the pipe wall. As the fluid flow's Reynolds number increases, the thin layer closest to the surface becomes even thinner. At a certain point, the roughness of the pipe wall becomes more important than this thin layer, and the friction between the fluid and the wall is mainly determined by the size of the roughness compared to the pipe diameter [2]. This is described by the roughness Reynolds number equation:

$$Re_\epsilon = \frac{\rho \epsilon u^*}{\mu}, \tag{E.16}$$

where u^* is the friction velocity and ϵ is the material's roughness. The roughness Reynolds number tells us whether the roughness on the surface of the pipe will affect the friction and heat transfer between the fluid and the pipe. If it is less than 5, the pipe is considered to be hydraulically smooth; if it is greater than 70, the pipe is considered to be fully rough; and if it is between 5 and 70, the pipe is in a transitional state [2]. There are established relationships in scientific literature to predict the heat transfer [16] and friction properties [17] for fully rough pipes.

When the surface of a pipe is rough, it can increase the amount of heat transferred between the fluid and the pipe wall. However, it also increases friction, which results in higher pressure losses [2].

Nusselt Number equations

As all the vital characteristics influence the Nusselt number in the relevant scenario, it is possible to present the equations that calculate it. Several fluid properties like viscosity and density depend on the fluid's temperature and, therefore, they should be taken at meaningful temperatures. The most appropriate temperature is the mean temperature between the fluid's initial and final temperature, however, the final temperature is not initially known. Consequently, a strategy can be to take the properties at the mean temperature between the propellant's initial temperature and the wall's temperature and calculate its final temperature. Another possibility is to use only the initial temperature as a reference. After getting the first final temperature value, performing at least one iteration is recommended through the same formulas again with the properties at the fluid's mean temperature since now there is an initial estimate for the final temperature's value. Through several iterations of this method, the final temperature value should converge.

Concerning laminar flow in linear ducts, for an isothermal wall, the Nusselt number is calculated by [2]:

$$Nu_D = \frac{3.657}{\tanh\left(2.264Gz^{-\frac{1}{3}} + 1.7Gz^{-\frac{2}{3}}\right)} + 0.0499Gz\tanh\left(Gz^{-1}\right) \tag{E.17}$$

As the length increases, the Graetz number tends to zero and the Nusselt number tends to 3.657 as expected previously.

In regards to turbulent flow in linear ducts, the Gnielinski equation is the most widely used [18] and is valid for a wide range of values. In fact, this range is not consensual as different sources state different ranges. A recent source by Lienhard J. et. al [2] mentions

the range to be $2300 \leq Re_D \leq 5 \times 10^6$ and $0.6 \leq Pr \leq 10^5$. However, the original Gnielinski equation does not take into account the thermal entrance region which can be crucial at small duct lengths. Taler D. et. al [19] modified the equation usefully by multiplying the original with a term that tends to one as the length increases:

$$Nu_D = \frac{\left(\frac{f_{DB}}{8}\right)(Re_D - 1000)Pr}{1 + 12.7\sqrt{\left(\frac{f}{8}\right)}(Pr^{\frac{2}{3}} - 1)}\left(1 + \left(\frac{D}{L}\right)^{\frac{2}{3}}\right). \tag{E.18}$$

where f_{DB} is the dimensionless Darcy-Weisbach friction factor whose calculation is explained further in section E.2.

Regarding flow in spiral tubes, Ferreira [20] gathered for his thesis a collection of useful formulas for the Nusselt number. Later, Takken [11] also uses the same equations. It is relevant to understand that each formula is applicable within its defined conditions.

E.1.3. TWO-PHASE PROPELLANT CONVECTION

Under certain conditions, the liquid may reach its saturation point and undergo flow boiling, resulting in a two-phase mixture of liquid and vapour. In this scenario, heat transfer occurs through both convective heat transfer and nucleate boiling and the heat flux is primarily used for evaporation [21]. The extra interaction between two different fluid phases usually leads to a higher convection heat transfer [2]. In fig. E.3, it is possible to visualize the different flow patterns in a two-phase boiling flow.

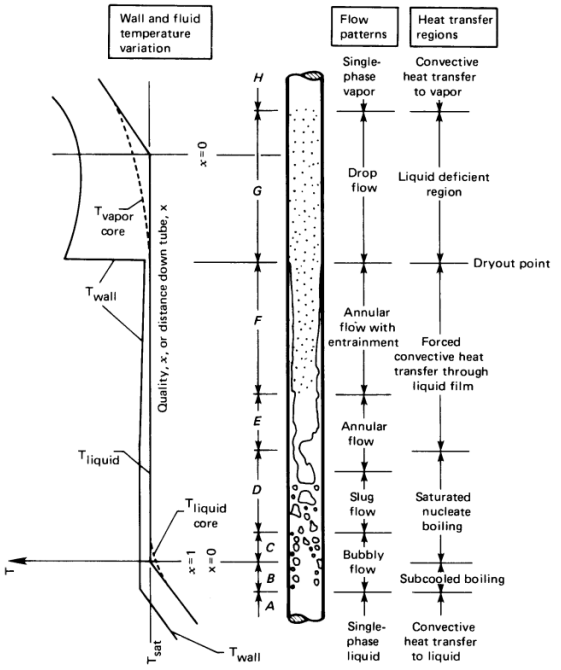

Figure E.3: The development of a two-phase flow in a vertical tube with a uniform wall heat flux (not to scale) [2]

Several equations have been developed to predict heat transfer in this case. However, in the literature, the majority studies the constant wall heat flux scenario. For example, Lienhard J. et al. [2] calculate the heat transfer for the nucleate boiling dominant and the convective boiling dominant cases and choose the biggest; the equations depend on the dimensionless boiling number which depends on the wall's heat flux.

The boiling curve of water at 1 atm can be seen in fig. E.4. Boiling curves allow us to determine in which type of heat transfer regime the flow is considered the temperature difference between the fluid and the wall.

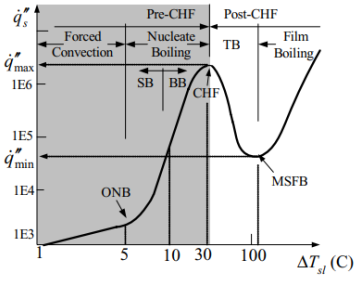

BB	Bulk Boiling
CHF	Critical Heat Flux
MSFB	Min. Stable Film Boiling
ONB	Onset of Nucleat Boiling
SB	Subcooled Boiling
TB	Transition Boiling

Figure E.4: The boiling curve of water at 1 atm and various heat transfer regimes [21]

Additionally, the heat transfer regime determines the set of equations to estimate the heat transfer process [21]. For instance, regarding film boiling, which is certainly the case when the propellant is hydrogen, Massoud M. [22] suggests the Dougal-Rohsenow correlation:

$$h = 0.023 \frac{k}{D} \left(Re \frac{\rho_g}{\rho} \right)^{0.8} Pr^{0.4}. \tag{E.19}$$

Concerning spiral ducts, there seems to be a lack of trustworthy correlations in the literature. Consequently, the linear case is used.

E.1.4. OUTER WALL CONVECTION

With the RAC's outer wall having a higher temperature than the surrounding medium, natural convection also occurs which induces energy losses. The geometry, as usual, also influences the amount of heat lost by convection of the outer wall [3]. Unfortunately, no information was found regarding outer convection loss in open cavities, only closed surfaces. Nevertheless, these closed surface formulas can give an irrefutably useful approximation which is better as the aperture ratio is smaller.

Rohsenow W. et al. [3] give formulas for several geometries including short vertical and horizontal cylinders and horizontal cones. In fact, Leenders H. [12] also used these equations. However, it requires the calculation of several quantities and the use of tabulated values which depend on the limited available length-to-diameter ratio. Therefore, it is a complex process.

However, simpler relations exist which do not require tabulated values in literature. Oosthuizen P. experimentally investigated free convective heat transfer from horizontal cones [23]:

$$Nu_D = 0.7 + 0.35 Ra_D^{0.125} + 0.51 Ra_D^{0.25}, \tag{E.20}$$

where Ra_D is the Rayleigh number:

$$Ra_D = Gr_D Pr. \tag{E.21}$$

The same author also published an article for the free convective heat transfer from vertical cones [24], where the following equation is obtained:

$$Nu_l = 0.65 \left(Gr_l^{0.25} + \frac{1.44}{\tan\left(\frac{\phi}{2}\right)} \right), \tag{E.22}$$

where Gr is the Grashof number and ϕ is the cone's included angle. In this case, Nu_l and Gr_l are based on the cone's slant height. These equations are simpler than the previous ones as they entail fewer equations and no dependency on tabled values.

Regarding the cylinder, Churchill S. and Chu H. [25] present the following equation in the horizontal case:

$$Nu_D = \sqrt{0.6 + 0.387 \left(\frac{Ra_D}{\left(1 + \left(\frac{0.559}{Pr}\right)^{\frac{9}{16}}\right)^{\frac{16}{9}}} \right)^{\frac{1}{6}}}. \tag{E.23}$$

For the vertical case, Day J. et al. [26] performed numerical simulations and achieve formulas for cylinders with a length-to-diameter ratio from 0.1 to 10. For example, the formula applicable when the ratio is between 2 and 10 is:

$$Nu_L = -0.06211 + 0.54414 Ra_L^{\frac{1}{4}} + 0.6123 \frac{L}{D}. \tag{E.24}$$

The formula for 0.1 to 2 is of a similar structure, only the coefficients change.

The resulting Nusselt number is an average for the whole outer surface and, thus, in equation (E.1), A corresponds to the outer surface area minus the aperture area to approximate the cavity's scenario.

E.2. PRESSURE GRADIENT

Pressure gradients refer to the change in pressure that occurs in a fluid as it flows through a pipe. The pressure gradient is caused by various factors, such as fluid viscosity, pipe geometry, flow rate, and external forces like gravity [2]. Since the nozzle is designed for a certain chamber pressure [4], it is ideal to know the pressure drop between the propellant tank to the chamber in order to understand at what pressure the propellant needs to be stored or vice-versa. There are different types of pressure gradients which will be discussed further and their sum is equal to the total gradient.

Single-phase flow friction pressure gradient

The pressure loss due to friction in a single-phase flow is easily calculated by the Darcy-Weisbach equation [2]:

$$\Delta p_{sp} = f_{DB} \frac{L}{D} \frac{1}{2} \rho u^2, \tag{E.25}$$

where sp stands for single-phase, L and D are the tube's length and diameter, respectively, ρ and u is the propellant's density and velocity, and f_{DB} is the dimensionless Darcy-Weisbach friction factor. For laminar and turbulent flow in linear smooth pipes, the friction factor is calculated, respectively, by [2]:

$$f_{DB} = \frac{64}{Re_D}, \tag{E.26a}$$

$$f_{DB} = \frac{1}{(1.82 \log Re_D - 1.64)^2}. \tag{E.26b}$$

On the other hand, for rough pipes, it is advised to consult a Moody diagram to extract values. Regarding spiral ducts, their friction factor is higher than linear and Guo L.

et al. [27] recommend the following relationships for, respectively, laminar and turbulent flow:

$$f_{DB} = \frac{1}{1-\left(1-\left(\frac{11.6}{Re_D\left(\frac{D}{D_c}\right)^{0.5}}\right)^{0.45}\right)^{\frac{1}{0.45}}}\frac{64}{Re_D}, \tag{E.27a}$$

$$f_{DB} = 0.304 Re_D^{-0.25} + 0.029\left(\frac{D}{D_c}\right)^{0.5}, \tag{E.27b}$$

where D_c is the diameter of the spiral.

Two-phase flow friction pressure gradient

The friction loss in two-phase flow is similar to the single-phase scenario. In fact, it is the same formula multiplied by a coefficient named the two-phase multiplier ϕ:

$$\Delta p_{tp} = \phi \Delta p_{sp} = \phi f_{DB}\frac{L}{D}\frac{1}{2}\rho u^2. \tag{E.28}$$

Several correlations for ϕ have been proposed with some being more complex than others, usually emerging from experimental test data. Massoud M. [22] mentions several equations such as the Reddy as well as the Friedel correlation. For horizontal and slightly inclined straight tubes, the Lockhart-Martinelli correlation [28] is commonly used in industry. Concerning helically coiled pipes, Guo L. et al. [27] proposed a correlation based on their own experimental data, however, prediction values can still diverge by about 40%. Gravity influences the pressure drop: horizontal tubes have the lowest value while the 45° downwards inclined coil has a 70% increase and the 45° upwards is in between these two values [27].

Experimental data concerning two-phase boiling flow in microgravity conditions is scarce as well as reliable correlations [29]. Consequently, it is better to consider the correlations obtained in earth-gravity conditions.

Acceleration pressure gradient

The acceleration pressure gradient Δp_{ac} results from a change of density and cross-section [30]:

$$dp_{ac} = \frac{\dot{m}}{A}du = Gd\left(\frac{G}{\rho}\right), \tag{E.29}$$

where G is the flow rate. Depending on the scenario, the equation can be simplified. For example, in a single-phase flow with a constant cross-section area:

$$\Delta p_{ac,1-2} = G^2\left(\frac{1}{\rho_2} - \frac{1}{\rho_1}\right). \tag{E.30}$$

In two-phase flow, the previous equation applies if a full transition from liquid to gas occurs: ρ_2 being the gas density and ρ_1 being the liquid density. In the general scenario for variable cross-section, the following formula applies:

$$dp_{ac} = \frac{1}{A} d\left(A\left(\frac{G_g^2}{\alpha_v \rho_g} \right) + \left(\frac{G_l^2}{(1-\alpha_v)\rho_l} \right) \right), \tag{E.31}$$

where α_v is the void fraction which is the gaseous volume fraction.

Gravitational pressure gradient

As the fluid moves downwards a pipe, the pressure at any given point will be influenced by the height of the fluid column above that point. The pressure at the bottom of the pipe will be greater than the pressure at the top of the pipe due to the weight of the fluid in the column and is calculated by [22]:

$$\Delta p_{grav} = \rho g_0 \sin\gamma, \tag{E.32}$$

where γ is the inclination of the pipe (positive if flowing downwards and negative otherwise). Thus, the pressure gradient due to gravity will cause the pressure to decrease as the fluid flows upward against gravity, and increase as the fluid flows downward with gravity [2].

REFERENCES

[1] Gomes, D. *Literature Study - Laser Propulsion System*. 2022. URL: https://github.com/djozao/Thesis.

[2] Lienhard IV, J. H. and Lienhard V, J. H. *A Heat Transfer Textbook*. 5th. Version 5.10. Cambridge, MA: Phlogiston Press, 2020. URL: http://ahtt.mit.edu.

[3] Rohsenow, W.M., Hartnett, J.P., and Cho, Y.I. *Handbook of Heat Transfer*. McGraw-Hill handbooks. McGraw-Hill Education, 1998. ISBN: 9780070535558.

[4] Zandbergen, B.T.C. *AE4-S01 Thermal Rocket Propulsion (version 2.08)*. Aug. 2020.

[5] Prakash, M., Kedare, S.B., and Nayak, J.K. "Investigations on heat losses from a solar cavity receiver". In: *Solar Energy* 83.2 (2009), pp. 157–170. ISSN: 0038-092X. DOI: https://doi.org/10.1016/j.solener.2008.07.011. URL: https://www.sciencedirect.com/science/article/pii/S0038092X08001795.

[6] Uhlig, R. et al. "Strategies Enhancing Efficiency of Cavity Receivers". In: *Energy Procedia* 49 (2014). Proceedings of the SolarPACES 2013 International Conference, pp. 538–550. ISSN: 1876-6102. DOI: https://doi.org/10.1016/j.egypro.2014.03.058. URL: https://www.sciencedirect.com/science/article/pii/S1876610214005128.

[7] Prakash, M., Kedare, S.B., and Nayak, J.K. "Numerical study of natural convection loss from open cavities". In: *International Journal of Thermal Sciences* 51 (2012), pp. 23–30. ISSN: 1290-0729. DOI: https://doi.org/10.1016/j.ijthermalsci.2011.08.012. URL: https://www.sciencedirect.com/science/article/pii/S129007291100250X.

[8] Paitoonsurikarn, S. et al. "Numerical Investigation of Natural Convection Loss From Cavity Receivers in Solar Dish Applications". In: *Journal of Solar Energy Engineering* 133.2 (Mar. 2011). 021004. ISSN: 0199-6231. DOI: 10.1115/1.4003582. eprint: https://asmedigitalcollection.asme.org/solarenergyengineering/article-pdf/133/2/021004/5714926/021004_1.pdf. URL: https://doi.org/10.1115/1.4003582.

[9] Wang, Ke et al. "A numerical study on the natural convective heat loss of an isothermal upward-facing cylindrical cavity". In: *Applied Thermal Engineering* 213 (2022), p. 118763. ISSN: 1359-4311. DOI: https://doi.org/10.1016/j.applthermaleng.2022.118763. URL: https://www.sciencedirect.com/science/article/pii/S1359431122007050.

[10] Jilte, Ravindra, Kedare, S.B., and Nayak, J.K. "Natural Convection and Radiation Heat Loss from Open Cavities of Different Shapes and Sizes Used with Dish Concentrator". In: *Mechanical Engineering Research* 3 (Jan. 2013). DOI: 10.5539/mer.v3n1p25.

[11] Takken, A. *Development of a high temperature Solar Thermal Propulsion engine*. 2021. URL: https://repository.tudelft.nl/record/uuid:e6cc6c72-bcfb-4927-a0bf-d935a6ba32f8.

[12] Leenders, H. C. M. and Zandbergen, B. T. C. "Development of a solar thermal thruster system". In: *59th International Astronautical Congress: IAC 2008, 29 September-3 October 2008, Glasgow, Scotland*. 2008.

[13] Paitoonsurikarn, Sawat and Lovegrove, Keith. "On the Study of Convection Loss from Open Cavity Receivers in Solar Paraboloidal Dish Applications". In: *Proceedings of 41st Conference of the Australia and New Zealand Solar Energy Society (ANZSES)* (Jan. 2004).

[14] Bergman, T.L. et al. *Fundamentals of Heat and Mass Transfer*. Wiley, 2011. ISBN: 9780470501979. URL: https://books.google.nl/books?id=vvyIoXEywMoC.

[15] Preijde, J. J. *Design of a Solar Thermal Power-Propulsion System for a Small Satellite*. 2015.

[16] Kakac, S, Shah, R K, and Aung, W. "Handbook of single-phase convective heat transfer". In: (Jan. 1987). URL: https://www.osti.gov/biblio/6291382.

[17] Haaland, S.E. *Simple and Explicit Formulas for the Friction Factor in Turbulent Pipe Flow, Including Natural Gas Pipelines*. Univ., Norwegian Inst. of Technol., Division of Aero- and Gas Dynamics, 1981. URL: https://books.google.nl/books?id=veHGPgAACAAJ.

[18] Gnielinski, V. "New equations for heat and mass transfer in the turbulent flow in pipes and channels". In: *NASA STI/Recon Technical Report A* 41.1 (Jan. 1975), pp. 8–16.

[19] Taler, Dawid and Taler, Jan. "Simple heat transfer correlations for turbulent tube flow". In: *E3S Web Conf.* 13 (2017), p. 02008. DOI: 10.1051/e3sconf/20171302008. URL: https://doi.org/10.1051/e3sconf/20171302008.

[20] Ferreira, R. A. *Development and testing of a water resistojet*. 2008.

[21] Kolev, Nikolay. "Multiphase Flow Dynamics 3". In: Jan. 2011, pp. 35–66. ISBN: 978-3-642-21371-7. DOI: 10.1007/978-3-642-21372-4_2.

[22] Massoud, M. *Engineering Thermofluids: Thermodynamics, Fluid Mechanics, and Heat Transfer*. Springer Berlin Heidelberg, 2005. ISBN: 9783540272809. URL: https://books.google.nl/books?id=9KIp%5C_fmC9A0C.

[23] Oosthuizen, P. "Free Convective Heat Transfer From Horizontal Cones". In: *ASME* (1973).

[24] Oosthuizen, P. H. and Donaldson, E. "Free Convective Heat Transfer from Vertical Cones". In: *Journal of Heat Transfer* 94.3 (Aug. 1972), pp. 330–331. ISSN: 0022-1481. DOI: 10.1115/1.3449945. eprint: https://asmedigitalcollection.asme.org/heattransfer/article-pdf/94/3/330/5728271/330_1.pdf. URL: https://doi.org/10.1115/1.3449945.

[25] Churchill, Stuart W. and Chu, Humbert H.S. "Correlating equations for laminar and turbulent free convection from a horizontal cylinder". In: *International Journal of Heat and Mass Transfer* 18.9 (1975), pp. 1049–1053. ISSN: 0017-9310. DOI: https://doi.org/10.1016/0017-9310(75)90222-7. URL: https://www.sciencedirect.com/science/article/pii/0017931075902227.

E

[26] Day, Jerod, Traum, Matthew, and Boetcher, Sandra. “Laminar Natural Convection From Isothermal Vertical Cylinders: A Revisit to a Classical Subject”. In: vol. 135. Mar. 2011. DOI: 10.1115/AJTEC2011-44552.

[27] Guo, Liejin, Feng, Ziping, and Chen, Xuejun. “An experimental investigation of the frictional pressure drop of steam–water two-phase flow in helical coils”. In: *International Journal of Heat and Mass Transfer* 44.14 (2001), pp. 2601–2610. ISSN: 0017-9310. DOI: https://doi.org/10.1016/S0017-9310(00)00312-4. URL: https://www.sciencedirect.com/science/article/pii/S0017931000003124.

[28] Chisholm, D. “A theoretical basis for the Lockhart-Martinelli correlation for two-phase flow”. In: *International Journal of Heat and Mass Transfer* 10.12 (1967), pp. 1767–1778. ISSN: 0017-9310. DOI: https://doi.org/10.1016/0017-9310(67)90047-6. URL: https://www.sciencedirect.com/science/article/pii/0017931067900476.

[29] Narcy, Marine and Colin, Catherine. “Two-phase pipe flow in microgravity with and without phase change: recent progress and future prospects”. In: *Interfacial Phenomena and Heat Transfer* 3.1 (2015).

[30] Roetzel, Wilfried, Luo, Xing, and Chen, Dezhen. “Chapter 2 - Basic thermal design theory for heat exchangers”. In: *Design and Operation of Heat Exchangers and their Networks*. Ed. by Roetzel, Wilfried, Luo, Xing, and Chen, Dezhen. Academic Press, 2020, pp. 13–69. ISBN: 978-0-12-817894-2. DOI: https://doi.org/10.1016/B978-0-12-817894-2.00002-9. URL: https://www.sciencedirect.com/science/article/pii/B9780128178942000029.

F

Locations

In this appendix, the locations relevant to the experimental part of this thesis are described in detail. These are:

- IWS and EWW,
- 3mE Welding Facility and DEMO,
- Meetshop,
- Cleanroom,
- Laser Facility.

IWS and EWW

The IWS and EWW are manufacturing workshops located at 3mE. In them, students can use the available equipment to manufacture their workpieces. In addition, the staff members are available to help as well as provide design tips to facilitate the manufacturing process.

Available machines include lathing and milling machines as well as laser cutting. Before being authorised to use the lathing and milling machines, students need to undergo mandatory training sessions, typically lasting 4 to 5 hours each. The author participated in these workshops and recommends these sessions for anyone interested as they give an insight into what is feasible to build easily as well as giving access to manufacturing machines and, thus, lowering manufacturing costs.

The EWW is focused primarily on requests from the 3mE staff but thesis students can also work there if space is available. It has smaller equipment available which allows for the manufacturing of tinier details.

The author used the IWS and EWW facilities to manufacture all the thruster pieces, except for two stainless steel pipes which were ordered online due to their smaller inner diameter size. Moreover, the thruster supports were also manufactured there.

Welding facility and DEMO

The welding facility is located at the 3mE building, close to the IWS. Equipment for welding, brazing and soldering is available to use if the necessary authorization is given. A colleague of the author had attended a welding workshop in that facility which allowed them to use it.

The DEMO has locations spread around campus. The one visited was the one in the aircraft hall in the AE faculty. There are several machines available but they are not to be used by students. Thus, it is necessary to ask the staff to perform the required task which might entail a cost or not.

The Welding facility at 3mE was used to weld together the RAC aluminium pieces. Moreover, some connections between stainless steel and steel pieces were soldered by Professor Jurriaan van Slingerland with silver free of charge. The rest of the silver soldering was performed by a DEMO staff member, free of charge as well.

Meetshop

The MeetShop is located in the 3mE building next to the IWS and allows students to borrow measurement equipment. The responsible person is Mr. Jacques Brenkman.

An online catalogue is available where the vacant equipment is shown. Nevertheless, inquiring personally or via email to the responsible for the needed instrumentation is recommended as the catalogue might not be up to date and an appointment is required beforehand in any case. Also, the responsible can provide some suggestions about the experimental setup. In addition to borrowing the equipment, the responsible provides adequate LabVIEW programs for the borrowed equipment.

The author borrowed two pressure sensors, a signal amplifier for the load cell and their respective data acquisition device (DAQ). Labview code for the pressure sensors was also provided.

Cleanroom

The cleanroom is located on the space engineering department floor at AE. It contains, amongst other things, a vacuum oven, a computer and a nitrogen feed system. Mehmet Sevket Uludag is the responsible contact person. To have access, a request needs to be made to the responsible and afterwards attend a workshop where an overview of the cleanroom and its safety precautions are given.

All of the experiments were conducted in the cleanroom. The author used plenty of the available resources including the test bench, load cell, nitrogen feed system and the computer.

Laser Facility

A laser was needed to perform the tests which required heating the RAC. After enquiring with the relevant staff, only one available laser fulfilled the requirements of continuous high-power output. That laser is a Philips VCSEL laser module that is located in the aircraft hall in the AE and used by the Department of Aerospace Structures and Materials (DASM). The responsible contact persons are Mr. Roy Awater and Prof. Julie Teuwen.

To have access to the laser, the author had to attend a laser safety workshop given by Mr. Andrei Anisimov. However, despite the efforts to execute the laser tests by carefully

developing a test plan after an in-person meeting with the involved parties, the responsible staff was quite unresponsive to the proposed plan. Moreover, PhD students were using the laser facility often and the responsible staff had shown their unease with the presence of a pressurized nitrogen tank in the laser facility. The combination of all these factors ultimately led to the regrettable decision to abandon the laser testing segment.

G

DATA SHEETS

In this chapter of the Appendix, the data sheets of the pressure sensors and the load cell used in this thesis' experimental tests are presented.

G.1. PRESSURE SENSOR

PU5404

Pressure transmitter

PU-010-SEG14-B-DVG/US/ /W

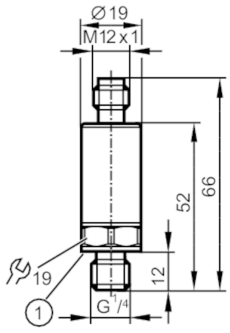

1 Sealing

Product characteristics				
Number of inputs and outputs	Number of analogue outputs: 1			
Measuring range	0...10 bar	0...145 psi	0...1000 kPa	0...1 MPa
Process connection	threaded connection G 1/4 external thread (DIN EN ISO 1179-2)			
Application				
Application	for industrial applications			
Media	liquids and gases			
Medium temperature [°C]	-40...90			
Min. bursting pressure	300 bar	4350 psi	30 MPa	
Pressure rating	25 bar	360 psi	2.5 MPa	
Note on pressure rating	static			
Vacuum resistance [mbar]	-1000			
Type of pressure	relative pressure			
Electrical data				
Operating voltage [V]	16...36 DC			
Current consumption [mA]	< 12			
Min. insulation resistance [MΩ]	100; (500 V DC)			
Protection class	III			
Reverse polarity protection	yes			
Power-on delay time [s]	< 0.1			
Inputs / outputs				
Number of inputs and outputs	Number of analogue outputs: 1			
Outputs				
Total number of outputs	1			
Output signal	analogue signal			
Number of analogue outputs	1			
Analogue voltage output [V]	0...10			

PU5404

Pressure transmitter

PU-010-SEG14-B-DVG/US/ /W

Min. load resistance	[Ω]	2000			
Short-circuit proof		yes			
Overload protection		yes			
Measuring/setting range					
Measuring range		0...10 bar	0...145 psi	0...1000 kPa	0...1 MPa
Accuracy / deviations					
Repeatability	[% of the span]	< ± 0,05; (with temperature fluctuations < 10 K)			
Characteristics deviation	[% of the span]	< ± 0,5; (incl. drift when overtightened, zero point and span error, non-linearity, hysteresis)			
Linearity deviation	[% of the span]	< ± 0,1 (BFSL) / < ± 0,2 (LS)			
Hysteresis deviation	[% of the span]	< ± 0,2			
Long-term stability	[% of the span]	< ± 0,1; (per 6 months)			
Temperature coefficient zero point and span	[% of the span / 10 K]	< ± 0,1 (-25...90 °C) / < ± 0,2 (-40...-25 °C)			
Response times					
Step response time analogue output	[ms]	1			
Operating conditions					
Ambient temperature	[°C]	-40...90			
Storage temperature	[°C]	-40...100			
Protection		IP 67; IP 69K			
Tests / approvals					
EMC		DIN EN 61000-6-2			
		DIN EN 61000-6-3			
Shock resistance		DIN EN 60068-2-27	50 g (11 ms)		
Vibration resistance		DIN EN 60068-2-6	20 g (10...2000 Hz)		
MTTF	[years]	762			
UL approval		UL Approval no.	J031		
Pressure Equipment Directive		Sound engineering practice; can be used for group 2 fluids; group 1 fluids on request			
Mechanical data					
Weight	[g]	59			
Materials		stainless steel (630/1.4542/17-4 PH); stainless steel (316L/1.4404); PEI			
Materials (wetted parts)		stainless steel (630/1.4542/17-4 PH)			
Min. pressure cycles		60 million; (at 1.2 times nominal pressure)			
Tightening torque	[Nm]	25...35; (recommended tightening torque; depends on lubrication, seal and pressure rating)			
Process connection		threaded connection G 1/4 external thread (DIN EN ISO 1179-2)			
Process connection sealing		FKM (DIN EN ISO 1179-2)			
Restrictor element integrated		no (can be retrofitted)			
Remarks					
Remarks		BFSL = Best Fit Straight Line			
		LS = limit value setting			

PU5404

Pressure transmitter

PU-010-SEG14-B-DVG/US/ /W

Pack quantity	1 pcs.

Electrical connection

Connector: 1 x M12; coding: A

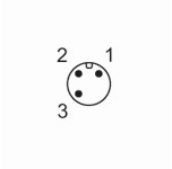

Connection

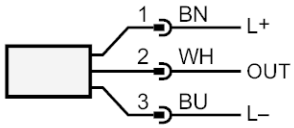

OUT	analogue output
	colours to DIN EN 60947-5-2
	Core colours :
BN =	brown
BU =	blue
WH =	white

G.2. FUTEK LSB200

FUTEK
ADVANCED SENSOR TECHNOLOGY, INC.

MODEL LSB200

Low Capacity Miniature S-Beam Jr. Load Cell

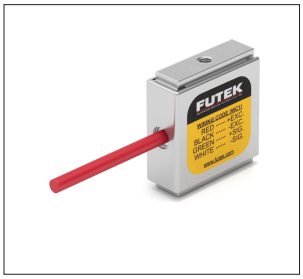

FEATURES

- Up to 10 times the overload protection
- Overload is available in Tension and Compression
- Light weight
- Notable nonlinearity
- Miniature size
- Ultra Low Capacity and High Sensitivity
- Vibration and shock resistance
- High flex silicone cable

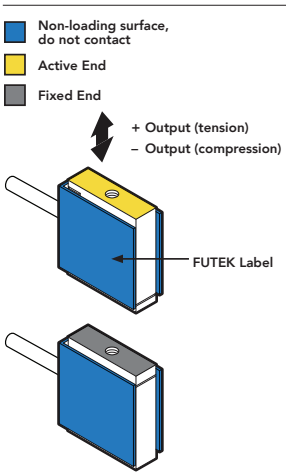

SPECIFICATIONS	
PERFORMANCE	
Nonlinearity	±0.1% of RO
Hysteresis	±0.1% of RO
Nonrepeatability	±0.05% of RO
ELECTRICAL	
Rated Output (RO)	See chart on third page
Excitation (VDC or VAC)	10 max
Bridge Resistance	1000 Ohm nom.
Insulation Resistance	≥500 MOhm @ 50 VDC
Connection	#29 AWG, 4 conductor, spiral shielded silicone cable, 5 ft [1.5 m] long
Wiring Code	WC1
MECHANICAL	
Weight (approximate)	0.7 oz [19.3 g] (10–250 g)
Safe Overload	1000% of RO
Material	Aluminum (10–250 g)
IP Rating	IP40
Vibration Resistance	20-2000 Hz, 0.01g²/Hz per MIL-STD-810E
Shock Resistance	500 g per IEC60068-2-27
TEMPERATURE	
Operating Temperature	-60 to 200°F [-50 to 93°C]
Compensated Temperature	60 to 160°F [15 to 72°C]
Temperature Shift Zero	±0.01% of RO/°F [0.018% of RO/°C]
Temperature Shift Span	±0.02% of Load/°F [0.036% of Load/°C]
CALIBRATION	
Calibration Test Excitation	5 VDC
Calibration (standard)	5-pt Tension
Calibration (available)	5-pt Tension and Compression
Shunt Calibration Value	301 kOhm (10–20 g) 150 kOhm (50–250 g)
CONFORMITY	
RoHS	EU 2015/863
CE	EN55011; EN61326-1

Sensor Solution Source
Load · Torque · Pressure · Multi-Axis · Calibration · Instruments · Software

www.futek.com

CE RoHS ANSI Z540-1 ISO 17025 ISO 9001 ISO 13485 U.S. Manufacturer

DIMENSIONS inches [mm]

TOLERANCE:
.X ± 0.1" [2.5 mm]
.XX ± 0.01" [0.25 mm]
.XXX ± 0.005" [0.127 mm]

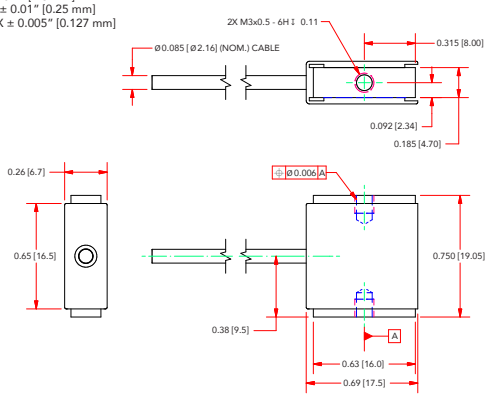

WIRING CODE (WC1)

RED	+ EXCITATION
BLACK	– EXCITATION
GREEN	+ SIGNAL
WHITE	– SIGNAL
SHIELD	FLOATING

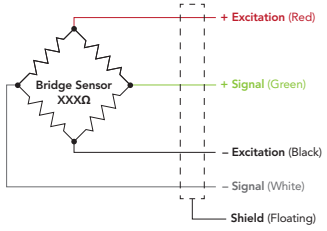

CAPACITIES

ITEM #	g	N	RO (nom)	Deflection	Natural Frequency (Hz)
FSH03867	10 g	0.1	0.5 mV/V	0.004 in [0.10 mm]	140
FSH03868	20 g	0.2	1 mV/V	0.008 in [0.20 mm]	140
FSH03869	50 g	0.5	2 mV/V	0.010 in [0.25 mm]	200
FSH03870	100 g	1.0		0.008 in [0.20 mm]	300
FSH03871	250 g	2.5		0.007 in [0.18 mm]	530

MOUNTING

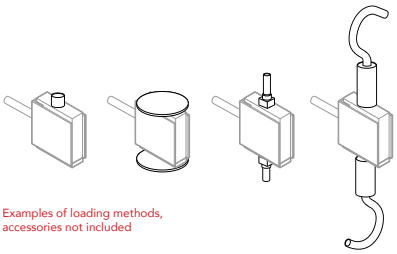

Examples of loading methods, accessories not included

Drawing Number: FI1455-B

10 Thomas, Irvine, CA 92618 USA
futek@futek.com
www.futek.com

CE RoHS ANSI Z540-1 ISO 17025 ISO 9001 ISO 13485 U.S. Manufacturer

H

TEST PROCEDURES

The purpose of detailing experimental procedures is to provide a comprehensive understanding of the methodologies used to obtain empirical data. This ensures reproducibility and allows other researchers to reproduce the work, enhancing the reliability and credibility of the research.

This section presents the test procedures for the leak testing and the cold gas flow testing. It is assumed that the user has assembled the propulsion system according to the experiment to be performed such as, for example, inserting the pressure sensors. The work of Versteeg has inspired these [1] as well as Cramer [2] and adapted where necessary to the developed experimental setup. The main adaptation is regarding the instrumentation used as their procedures refer to heaters, which are not a part of the experimental setup of this thesis.

H.1. LEAK TEST PROCEDURE

H.1.1. BACKGROUND AND INSTRUMENTATION OVERVIEW

The original author of this procedure is Versteeg in 2020 [1]. This corresponds to a second version adapted by the author of this thesis in 2024.

For the experiment, the user requires a thruster system with a nozzle closing mechanism, at least one pressure sensor measuring the thruster's pressure, a mass flow reader and a nitrogen feed system. Needless to say, the sensors need to be connected to devices capable of gathering their data via their respective data transfer mechanisms. The procedure has been produced considering the nitrogen feed system available in the Cleanroom of the TU Delft's Aerospace Faculty (Fig. H.1). A Labview program named "Leak Test" is used and it stores the information on the pressure and the mass flow readings.

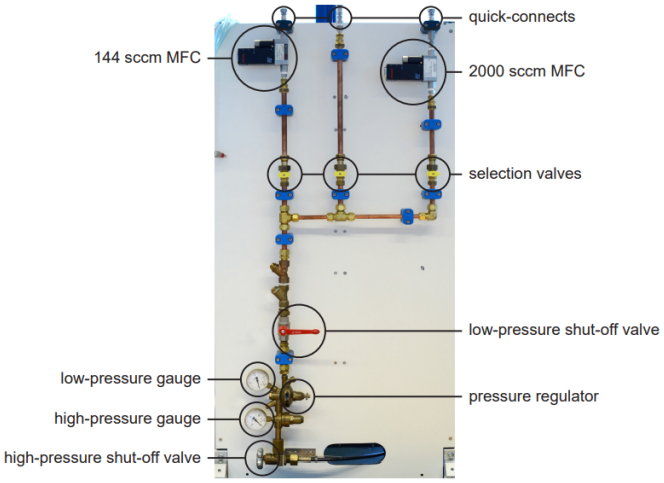

Figure H.1: Nitrogen Feed System and its components [3].

H.1.2. PREPARATION

1. Connect the pressure sensors to the corresponding DAQ device and this one to the user's laptop through the USB port.
2. Ensure that all the valves of the feed system are properly closed.
3. Connect the tubing from the feed system to the system's propellant inlet.
4. Seal the nozzle with its respective cap to close the thruster system.
5. Open the main valve on top of the nitrogen-pressurized cylinder, located behind the feed system board.
6. Open the high-pressure shut-off valve at the bottom of the feed system board.
7. The high-pressure gauge indicates the pressure inside the cylinder. If this is close to zero, the cylinder should be replaced according to the instructions on the board.
8. Adjust slowly the pressure regulator upward to the desired value for the feed-system pressure by carefully rotating it clockwise. The pressure in the feed system (relative to atmospheric) can be read-off on the low-pressure gauge.
9. Open the low-pressure shut-off valve (long red handle) by aligning it with the direction of the tubing.

H.1.3. EXPERIMENT EXECUTION

1. Open the LabView program - **"Leak Test"** - developed for this experiment.
2. Specify the test name and folder to save data in, then run the program.

3. Open the selection valve (small yellow knob) of the tubing connected to the system again by aligning it with the tubing.

4. Wait until the thrust chamber pressure and the mass flow reading remain constant over time and close the selection valve.

5. Record pressure over time for the desired period. For very low leakage flows this can take multiple hours or days, while for relatively severe leaks it may only take minutes or seconds.

6. When sufficient time has passed, stop the LabView program, making sure that the data has been saved.

7. Repeat the experiment execution with the various initial inlet pressure desired.

H.1.4. SHUTDOWN

1. Close the main valve on top of the nitrogen cylinder.

2. Close the high-pressure shut-off valve.

3. Turn the pressure regulator fully counterclockwise, so that it will start at zero outlet pressure for subsequent tests, and gas in the high-pressure line between the cylinder and the regulator is not wasted.

4. Remove the nozzle cap.

5. Close the low-pressure shut-off and selection valves.

6. Uncouple the propellant quick-connect to the propulsion system.

7. Disconnect the pressure sensor and unplug the used DAQs.

H.2. TEST BENCH CALIBRATION TEST PROCEDURE

H.2.1. BACKGROUND AND INSTRUMENTATION OVERVIEW

A previous procedure for the calibration of the TB-50m was not found. Thus, the author considering the same structure as the other test procedures created his own (Version 1 - 2024).

For the experiment, the user requires the Variable-Turn Density Coil (VTDC) with its corresponding power supply (SM-7020D), the thrust bench TB-50m and an assembled load cell with its signal amplifier, and the whole thruster setup (including attached instrumentation and feed system tubing) to be used in the following experiments.

A Labview program ("Calibration - LSB200") has been created and it controls the current supplied to the VTDC and measures the load cell voltage output. When the user starts the Labview program, the supplied current starts at 0 A and increases by 1 A every 20 seconds until it reaches 16 A, going back to 0 A after. For a successful calibration of the load cell voltage at the end when reset to 0 A should return to the same level as before the testing, otherwise the setup is somehow faulty.

H.2.2. PREPARATION

1. Turn on the SM-7020D power supply (60 minutes warm-up time).
2. Turn on the cleanroom's desktop.
3. Assemble the load cell and the VTDC to the thrust bench.
4. Measure the distances of both of them to the rotating beam.
5. If it is a calibration with the thruster on, attach the thruster to the test bench and insert a counterweight with equal mass in the opposite arm. Tap down all the cables that might influence the movement of the test bench.
6. Open the Labview program and ensure that the measured voltage is steady, if not detect the problem and fix it.

H.2.3. EXPERIMENT EXECUTION

1. Specify the test name and folder to save data in.
2. Run the LabView program.
3. After the LabView program resets to 0 A, stop it, making sure that the data has been saved.
4. Wait enough time for the VTDC to cool down (for this specific experiment set-up, the duration is around 10 minutes).
5. Repeat the experiment execution the necessary number of times.
6. After the calibration without the thruster on the test bench, add it to the test setup.
7. Repeat the experiment execution with the thruster on the test bench the same number of times.

H.2.4. SHUTDOWN

1. Turn off the SM-7020D and the desktop.
2. Only dismantle the thruster of the test bench, the load cell and the VTDC if no flow testing will be performed after. Reassembling could change the determined relationships.

H.3. COLD GAS FLOW TEST PROCEDURE

H.3.1. BACKGROUND AND INSTRUMENTATION OVERVIEW

The original author of this procedure is Versteeg in 2020 [1]. This corresponds to a second version adapted by the author of this thesis in 2024.

For the experiment, the user requires a thruster system, at least one pressure sensor measuring the thruster's pressure, a temperature sensor to measure the propellant temperature, a mass flow reader, a nitrogen feed system and a calibrated test bench with

a load cell incorporated. Needless to say, the sensors need to be connected to devices capable of gathering their data via their respective data transfer mechanisms. The procedure has been produced considering the nitrogen feed system available in the Cleanroom of the TU Delft's Aerospace Faculty (Fig. H.1). A Labview program that reads and stores the information on the pressure, temperature, mass flow readings and measured thrust is required.

H.3.2. PREPARATION

1. Turn on and/or plug in the components requiring warm-up or start-up time:
   (a) Plug in the power brick for the Brooks 5851S mass flow sensor (45 min).
   (b) Turn on the user's laptop and open the developed Labview program which reads all the necessary sensors.
2. While waiting for the previous components to initialize, install the thruster on the thrust bench and stably position the whole propulsion system.
3. Connect the instrumentation accordingly to their DAQs and the laptop. Test if all the sensors are working and providing expected values.
4. Couple the propellant feed system tubing to the system's propellant inlet.
5. Open the feed system:
   (a) Open the main valve on top of the cylinder located behind the feed system board.
   (b) Open the high-pressure shut-off valve at the bottom of the feed system board.
   (c) The high-pressure gauge indicates the pressure inside the cylinder. If this is below the desired test pressure, abort the test and the cylinder should be replaced according to the instructions on the board.
   (d) Adjust slowly the pressure regulator upward to the desired value for the feed-system pressure by carefully rotating it clockwise. The pressure in the feed system (relative to the atmospheric) can be read-off on the low-pressure gauge.
   (e) Open the low-pressure shut-off valve (long red handle) by aligning it with the direction of the tubing.

H.3.3. EXPERIMENT EXECUTION

1. Tune the RAC inlet pressure:
   (a) Run the Labview program.
   (b) Repeat the following until the desired value of the RAC inlet pressure is within accuracy:
      i. Open the selection valve connected to the system.
      ii. Close the selection valve.

iii. If the recorded pressure is too low, slightly open the pressure regulator (counterclockwise); Otherwise, close it slightly (clockwise).

(c) Stop the Labview program.

2. Run the Labview program.
3. Open the respective selection valve.
4. Close the selection valve after the intended test time has passed.
5. Repeat this whole process for the different RAC inlet pressure values.

H.3.4. SHUTDOWN

1. Close the main valve on top of the nitrogen cylinder.
2. Close the high-pressure shut-off valve.
3. Turn the pressure regulator fully counterclockwise, so that it will start at zero outlet pressure for subsequent tests, and gas in the high-pressure line between the cylinder and the regulator is not wasted.
4. Bleed off the excess nitrogen in the low-pressure zone until ambient.
5. Close the low-pressure shut-off and selection valves.
6. Close Labview.
7. Uncouple the propellant quick-connect to the propulsion system.
8. Unplug the power brick for the Brooks 5851S mass flow sensor.
9. Disconnect the instrumentation and unplug the used DAQs.

REFERENCES

[1] Versteeg, H. *Novel fabrication method for a hot gas supersonic micro-thruster*. 2020. URL: https://repository.tudelft.nl/record/uuid:ac2482ad-0f8e-4569-8bd4-fd11bd6327bd.

[2] Cramer, L. *The advancement of the TU Delft vaporising liquid micro-resistojet design*. 2024. URL: https://repository.tudelft.nl/record/uuid:6c21b8f6-c55a-44e6-86bf-69f99c1e0978.

[3] Hutten, R. *Vaporizing Liquid Micro-resistojet experimentation*. 2021. URL: https://repository.tudelft.nl/record/uuid:960550ce-eb34-4f3d-873a-1f2a6f4763f0.

I

NITROGEN TEST PLOTS

In this chapter of the appendix, the data plots of the gathered data are presented for the four different cold flow gas test runs performed in this thesis. For each run, the mass flow, the absolute inlet pressure, the temperature and the load cell voltage output are shown.

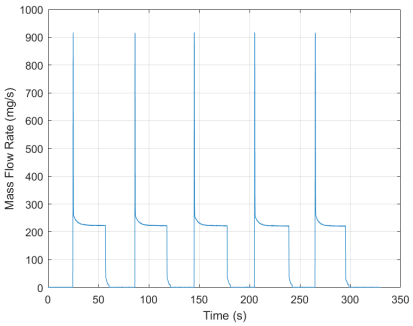

(a) Mass flow

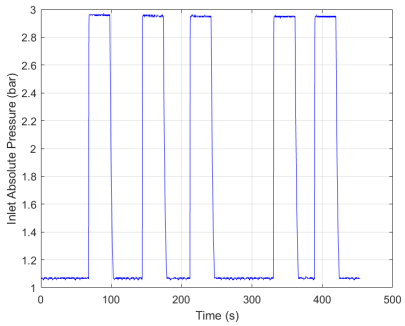

(b) Absolut Inlet Pressure

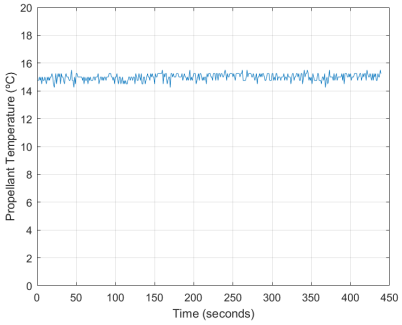

(c) Temperature

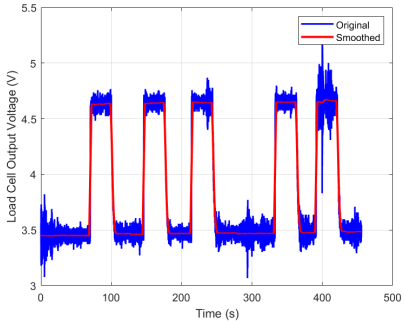

(d) Load Cell Output Voltage

Figure I.1: NT-1 Results

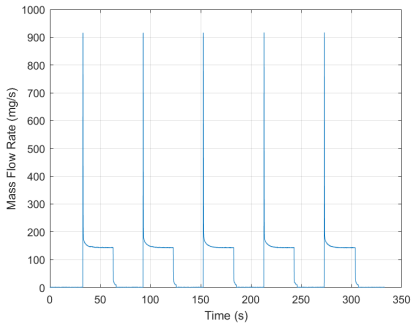

(a) Mass flow

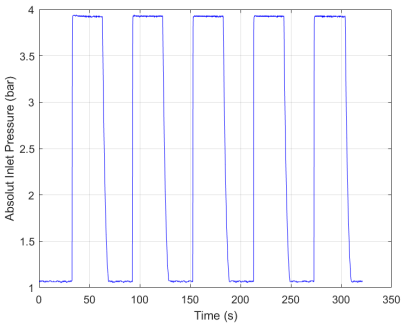

(b) Absolut Inlet Pressure

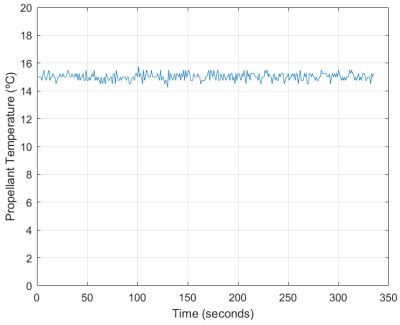

(c) Temperature

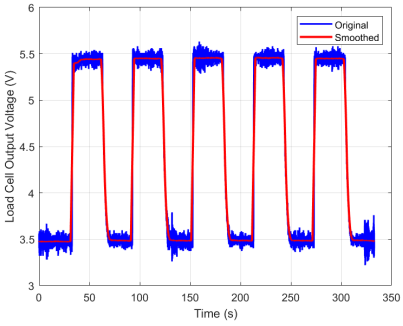

(d) Load Cell Output Voltage

Figure I.2: NT-2 Results

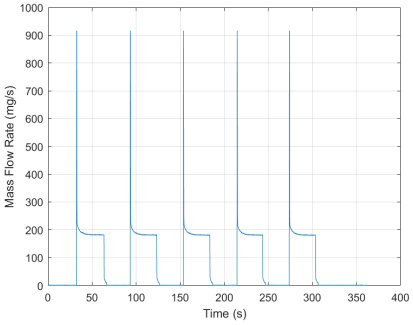

(a) Mass flow

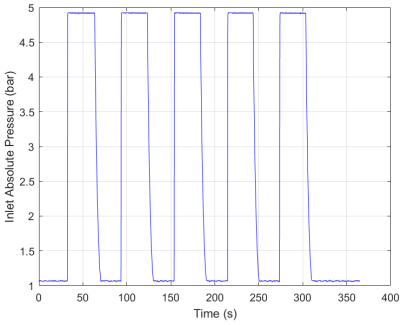

(b) Absolut Inlet Pressure

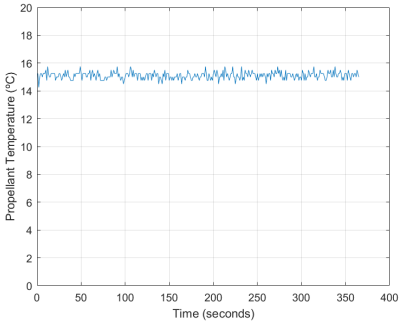

(c) Temperature

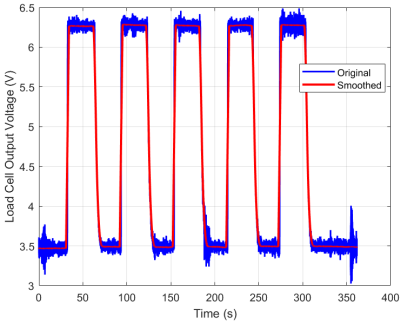

(d) Load Cell Output Voltage

Figure I.3: NT-3 Results

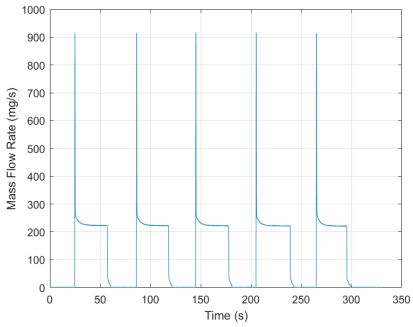

(a) Mass flow

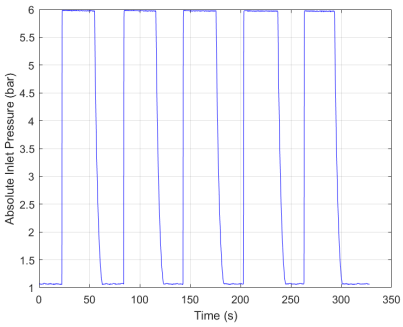

(b) Absolut Inlet Pressure

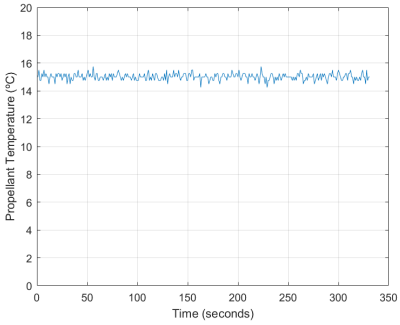

(c) Temperature

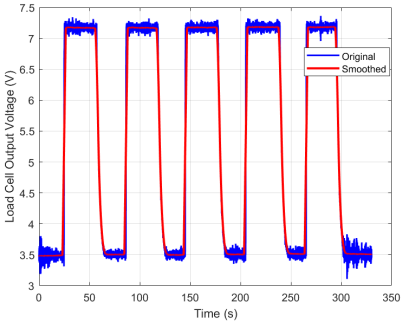

(d) Load Cell Output Voltage

Figure I.4: NT-4 Results

J

Discharge Coefficient for Orifice Plates

Kayser and Shambaugh studied experimentally the discharge coefficients for compressible flow through small-diameter orifices and convergent nozzles [1]. In their paper, P_1, P_3 and P_{crit} refer to the chamber, ambient and critical pressure, respectively, and the square-edged nozzles are referred to with the S symbol. Their pressure data only covers the first two experimental tests (NT-1 and NT-2).

The first remark made is about the effect of the ratio between the throat length and its diameter on the discharge coefficient (Fig. J.1a). As the length-to-diameter ratio increases, the discharge coefficient line starts to flatten, becoming almost independent of the pressure chamber increase. This change results from the complex interaction between the contracted flow and the nozzle throat's interior, an interaction that does not occur at low ratios [1]. In the case of the manufactured nozzle, the length-to-diameter ratio is approximately 4, which is twice as big as the maximum provided example. Thus, our nozzle's discharge coefficient should also remain within a small range as chamber pressure increases, which corroborates with the experimental data (table 8.7).

Fig. J.1b shows the discharge coefficient for straight orifices at different diameters and temperatures. The discharge coefficient remains constant. This is a result of the previous result as their length-to-diameter ratios are above 1.92. Moreover, the temperature has no apparent effect on the discharge coefficient. However, when examining the diameter, it is clear that smaller diameters lead to lower discharge coefficients. The S3 and S1 orifices have diameters of 1.656 mm and 1.125 mm, respectively, and their discharge coefficients are around 0.86 and 0.80. Their orifices have a chamber diameter of 22.23 mm which is relatively close to the manufactured 25 mm, so comparing the diameters of their models and the tested nozzle is not completely unfounded. If the discharge coefficient reduction with the diameter trend remained, the manufactured nozzle's discharge coefficient would be below 0.80. A linear fit to the data (R^2 = 0.979) suggests a value of 0.73 which needs to be considered cautiously since it is an extrapolation from three data points. However, the nozzle is not a perfect orifice, despite the converging

section being rough and quite angular, it is expected that its discharge coefficient would be slightly better than its orifice counterpart.

To sum up, the experimental discharge coefficient value and its invariance regarding chamber pressure are logically substantiated by this paper's data for the first two pressures tested.

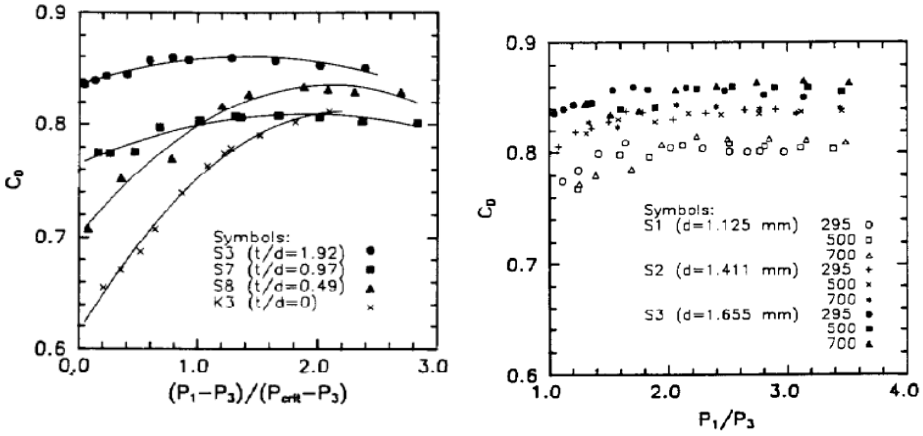

(a) Effect of length-to-diameter ratio at constant diameter upon C_D for air flow through straight orifices at 295 K. The curves are polynomial fits of the data. [1]

(b) Air discharge data for three 3.18 mm thick straight orifices at 295, 500 and 700 K [1]

Figure J.1: Straight nozzle experimental data from Kayser and Shambaugh [1].

Other findings in the literature support the idea of a constant discharge coefficient for orifices. Deckker and Chang [2] performed a similar experimental set-up to study compressible flow through orifices. They investigated the effect of the Reynolds number on the discharge coefficient by keeping the pressure ratio constant and increasing the stagnation temperature. At nominal Reynolds numbers above 10^4, the discharge coefficient showed no dependency on it, which is the experimental situation of this thesis. Next, the discharge coefficient is concluded to be a function of both the length-to-diameter ratio and the pressure ratio. Fig. J.2 shows the discharge coefficient for several pressure ratios for the two extreme length-to-diameter cases. The mass flow number in the axis is a dimensionless mass flow metric that has the chamber pressure in the denominator and, thus, at critical conditions, it remains constant. The increase in the length-to-diameter ratio leads to a flattening of the pressure ratio effect in the discharge coefficient, corroborating with Kayser and Shambaugh's work. Also, unlike the previous paper, the pressure ratios investigated include the values between 0.2 and 0.4 which are the experimental values for this test and, therefore, validate the constant experimental discharge coefficient. Lastly, the discharge coefficient values fall in the 0.8 and 0.9 range and no investigation on the diameter effect was performed.

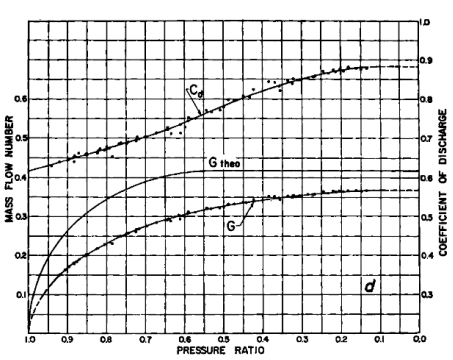

(a) Sharp-edge (L/D = 0.05)

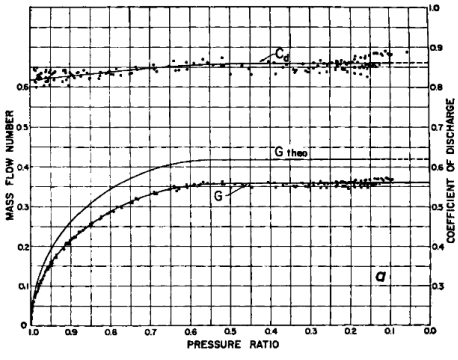

(b) L/D = 2

Figure J.2: Effect of pressure ratio and length-diameter ratio on mass flow number and discharge coefficient [2].

Zandbergen [3] presents a way to calculate the discharge coefficient for injectors and in this case yields a value of 0.82 which is not far off of 0.78-0.79 experimental value obtained. However, despite the closeness, this value is for incompressible flow which is not the case.

Theories have been developed to estimate the compressible discharge coefficient from the incompressible value and the discharge coefficient should theoretically increase with the pressure ratio in the orifice.

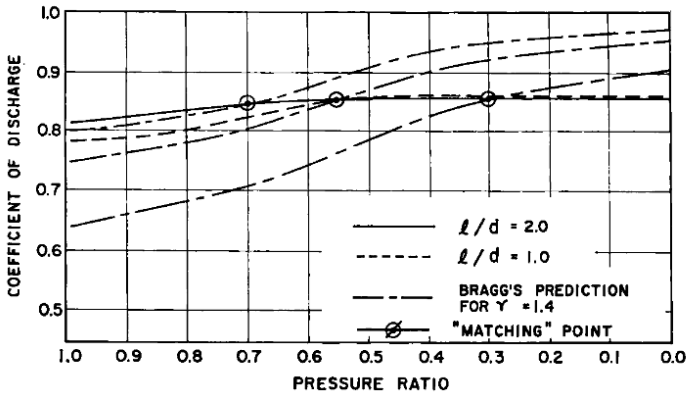

Figure J.3: Comparison of predicted and experimental values of discharge coefficients for L/D ratios equal to 1.0 and 2.0 [2]

Deckker and Chang investigated the relationship between their experimental results and one of the developed theories, in this case, by Bragg [4]. They concluded that for thick orifices the theory does not match the experimental results. Fig. J.3 shows the

Comparison of predicted and experimental values of discharge coefficients for L/D ratios equal to 1 and 2. Bragg expects a significant increase in the discharge coefficient as the pressure ratio decreases. But for thick orifices, the variation is not as meaningful, stagnating after the critical pressure.

By examining all the plots, it is evident that the incompressible flow estimate for thick orifices (high L/D) does not fall far from the compressible flow scenario. This difference seems to decrease even further with the increase in the length-diameter ratio. Consequently, for a length-diameter ratio of 4.0, the estimation method provided by Zandbergen is suitable for a discharge coefficient prediction and is within a 5% range from the experimental result.

REFERENCES

[1] Kayser, J. C. and Shambaugh, R. L. "Discharge coefficients for compressible flow through small-diameter orifices and convergent nozzles". In: *Chemical Engineering Science* 46.7 (1991), pp. 1697–1711. ISSN: 0009-2509. DOI: https://doi.org/10.1016/0009-2509(91)87017-7. URL: https://www.sciencedirect.com/science/article/pii/0009250991870177.

[2] Deckker, B. E. L. and Chang, Y. F. "Paper 7: An Investigation of Steady Compressible Flow through Thick Orifices". In: *Proceedings of the Institution of Mechanical Engineers, Conference Proceedings* 180.10 (1965), pp. 312–323. DOI: 10.1243/PIME_CONF_1965_180_307_02. eprint: https://doi.org/10.1243/PIME_CONF_1965_180_307_02. URL: https://doi.org/10.1243/PIME_CONF_1965_180_307_02.

[3] Zandbergen, B.T.C. *AE4-S01 Thermal Rocket Propulsion (version 2.08)*. Aug. 2020.

[4] Bragg, S. L. "Effect of Compressibility on the Discharge Coefficient of Orifices and Convergent Nozzles". In: *Journal of Mechanical Engineering Science* 2.1 (1960), pp. 35–44. DOI: 10.1243/JMES_JOUR_1960_002_007_02. eprint: https://doi.org/10.1243/JMES_JOUR_1960_002_007_02. URL: https://doi.org/10.1243/JMES_JOUR_1960_002_007_02.